

ABSTRACT

Title of dissertation: NANOCONFINED POLYELECTROLYTE
BRUSHES: THERMODYNAMICS,
ELECTROSTATICS AND TRANSPORT

Guang Chen

Dissertation directed by: Dr. Siddhartha Das
Department of Mechanical Engineering

Polyelectrolyte (PE) grafting on the solid-liquid interface of a nano-channel renders tremendous functionalities to the nano-channel. These grafted PE molecules attain "brush"-like configuration for large grafting density (σ), which makes the nano-channel (often denoted as *soft nano-channel*) capable of applications such as ion manipulation, ion sensing, current rectification, nano-fluidic diode action, and flow regulation.

The present thesis focuses on the theoretical modeling of the thermodynamics, electrostatics and transport of such nano-confined PE brush systems. The thesis starts by developing new scaling laws a) to determine the phase space for the grafting density (σ) and the polymer size or number of monomers (N_p) of the grafted PE molecules that ensure that the PE chains can simultaneously adopt a "brush"-like configuration and do not exceed the nano-channel half height, and b) to identify the regime where the elastic and the excluded volume effects of the chains can be decoupled from the electrostatic effects. The subsequent part of the thesis is divided

into two broad parts. In the first part, the thermodynamics, electrostatics, and the transport of PE-brush-grafted nano-channels in the *decoupled regime* is probed. In the second part, however, the analysis is carried out to elucidate the physical picture of the PE-brush-grafted nano-channels in the *coupled regime*.

For the analysis in the *decoupled regime*, firstly the electrostatics of such PE-brush-grafted nanochannels has been probed. These PE brushes are considered to exhibit pH-dependent charge density. The salient feature of the modeling is to account for the explicit hydrogen ion concentration in the corresponding electrostatics of the electric double layer (EDL) induced at the PE-brush-electrolyte interface. Results indicate profound influences of the hydrogen ion concentration, ionization constant of the PE brushes, salt concentration, and degree of confinement introduced by the nano-channel height in the overall electrostatics of the PE brushes. Secondly, continuum-based modeling is conducted to study the transport in such pH-responsive PE-brush-grafted nano-channels by quantifying the corresponding electric-field-driven electroosmotic (EOS) transport and the ionic current in the decoupled regime. Results reveal highly dominant ionic current and tremendously suppressed electroosmotic transport –both these findings are massively significant in designing of highly efficient and programmable soft nano-channels for sensing ions and analytes.

The last part of the thesis is focused in studying the nano-confined PE brushes in the *coupled regime*, i.e., where the elastic and the excluded volume effects interplay with the electrostatic effects to determine the overall brush behavior. Firstly, mean field theory models are developed to probe the electrostatics and configuration of PE brushes grafting the nano-channel inner walls. Results indicate highly non-intuitive

swelling-shrinking behavior of end-charged brush, while for backbone-charged brush, one can always witness swelling behavior due to the electrostatic effect. Detailed free energy analysis is subsequently invoked in order to explain these non-trivial results for the end-charged brushes. Secondly, ionic current and EOS transport in these end/backbone-charged-PE-brush-grafted nano-channels, with the brushes being described in the *coupled regime*, has been probed. Results indicate a most remarkable *enhancement* in the strength of the EOS transport. It completely reverses the standard understanding that the EOS transport is invariably suppressed in PE-brush-grafted nano-channels owing to the additional drag introduced by the brushes. Finally, we further quantify how the salt concentration and pH values of electrolyte effects the ionic and EOS transport in nano-channels grafted with end/backbone-charged brushes.

We anticipate that the findings of the present thesis will provide completely new perspectives in understanding several unknown facets of PE-grafted nano-channels. These facets will be pivotal in not only designing soft nano-channels with novel functionalities that can potentially be applied in several disciplines ranging from nanotechnology to biomedical and biochemical engineering, but will also provide important clues to decipher the behavior of a myriad of biological and chemical systems (e.g., PE-grafted nanoparticles, sheathed bacteria, phage viruses, etc.) that bear certain geometric and physical resemblances to the PE-grafted nano-channel system.

NANOCONFINED POLYELECTROLYTE BRUSHES:
THERMODYNAMICS, ELECTROSTATICS, AND TRANSPORT

by

Guang Chen

Dissertation submitted to the Faculty of the Graduate School of the
University of Maryland, College Park in partial fulfillment
of the requirements for the degree of
Doctor of Philosophy
2016

Advisory Committee:

Professor Siddhartha Das, Chair/Advisor
Professor Srinivasa R. Raghavan, Dean's Representative
Professor Jungho Kim
Professor Peter Chung
Professor Ryan D. Sochol

© Copyright by
Guang Chen
2016

Acknowledgments

First of all, I would like to deliver my great appreciation to my advisor, Dr. Siddhartha Das, for his guidance and inspiration that led me to arrive at this stage of my doctoral training so fast. Being the first Ph.D. student in the group is hard. Dr. Das was so eager to check the talent of his student, while I was under huge pressure to keep making progress to prove myself. But I always feel it was my fortune to be my advisor's first Ph.D. student, since he had the greatest expectation of me and devoted the maximum effort to help me succeed. I benefited a lot during that time and we have been very productive since then. I can't thank him enough for encouraging me and providing me opportunities to present my work in conferences, and for his immense trust, advice and support! I shall also like to express my deepest thanks to my thesis committee members (Prof. Raghavan, Prof. Kim, Prof. Chung, and Prof. Sochol) for their invaluable suggestions for improving my thesis.

Secondly I am indebted to my parents, who have built up a sweet family for three of us with their wisdom and love. They provided me with the best education environment and taught me to have an earnest attitude towards everything in my life. They always trust me and encourage me to pursue my dreams, which eventually helped me to take the decision for applying for a Ph.D. program.

Finally, I shall like to sincerely thank my lab-mates (Shayandev, Joseph, Parth, Hao, Haoyuan and Jahin) and friends (Jie, Shuyue, An, Martin, etc.) for always being around to support. I owe my gratitude to all the people who have made this thesis proposal possible and because of whom my graduate experience has been one that I will cherish forever.

Table of Contents

List of Tables	vi
List of Figures	vii
1 Introduction	1
1.1 Polymer and polyelectrolyte brushes: Fundamental ideas	1
1.2 Polymer and polyelectrolyte brushes: Applications	5
1.3 Theoretical modelling of polymer and polyelectrolyte brushes	6
1.3.1 State-of-the-art methods	6
1.3.2 Open questions and main agenda of the thesis	7
1.4 Organization of the thesis	10
2 Nanoconfined Polyelectrolyte brushes: Scaling laws	13
2.1 Introduction	14
2.2 Scaling Laws for a polyelectrolyte-grafted nanochannel	16
2.3 Applications of the scaling laws	22
2.4 Conclusions	24
3 Electrostatics of nanoconfined pH and pOH responsive polyelectrolyte brushes in the decoupled regime	25
3.1 Introduction	26
3.2 Theory	28
3.3 Results	37
3.3.1 Electrostatic potential and hydrogen ion concentration profiles for uniform distribution of PCS within the PE brush layer	38
3.3.2 Electrostatic potential and hydrogen ion concentration profiles for non-uniform distribution of PCS within the PE brush layer	41
3.4 Discussions	46
3.5 Conclusions	47

4	Ionic Current in pH and pOH responsive polyelectrolyte brush grafted nanochannels in the decoupled regime	49
4.1	Introduction	50
4.2	Results	51
4.3	Conclusions	55
5	Electroosmotic transport in pH responsive polyelectrolyte brush grafted nanochannels in the decoupled regime	56
5.1	Introduction	57
5.2	Theory	59
5.2.1	Electroosmotic transport in the polyelectrolyte-grafted nanochannel with pH-dependent charge density	59
5.2.2	Electroosmotic transport in the polyelectrolyte-grafted nanochannel with pH-independent charge density	62
5.3	Results	63
5.4	Discussion	66
5.4.1	Significance of the present study in different soft-nanochannel-based applications	66
5.4.2	Scaling calculations for flow induced deformation of PE brushes	68
5.5	Conclusions	72
6	Configuration and electrostatics of end-charged nanoconfined polyelectrolyte brushes in the coupled regime: Salt concentration and pH dictated anomalous shrinking-swelling of the brushes	73
6.1	Introduction	75
6.2	Theory	79
6.2.1	Governing Equations for pH-independent PE Brushes	79
6.2.2	Equilibrium conditions and non-dimensionalization for pH-independent PE Brushes	82
6.2.3	Governing Equations and Equilibrium for pH-responsive PE Brushes	86
6.3	Results and Discussions	90
6.3.1	Current understanding on the salt-dependent height variation of PE brushes	90
6.3.2	Configuration and electrostatics for weakly-end-charged, pH-non-responsive PE brushes	91
6.3.3	Configuration and electrostatics for end-charged, pH-responsive PE brushes	96
6.4	Conclusions	102
6.5	Appendix: Derivation of eq.(6.12)	103
7	Ionic current in nanochannels grafted with end-charged, pH-responsive polyelectrolyte brushes described in the coupled regime	105
7.1	Introduction	106
7.2	Calculation of the Ionic Current	107

7.3	Results	108
7.4	Conclusions	112
8	Massive enhancement of electroosmotic transport in nanochannels grafted with end-charged polyelectrolyte brushes	114
8.1	Introduction	115
8.2	Calculation of the EOS Transport	117
8.3	Results	120
8.3.1	Variation of the brush height	120
8.3.2	EDL electrostatic potential and the ion number density distribution	121
8.3.3	Electroosmotic velocity field	124
8.3.4	pH-responsive electrostatics and EOS velocity fields	130
8.3.5	Phase space for the volume flow rate ratio in nanochannels grafted with end-charged PE brushes	135
8.4	Discussions	138
8.4.1	Impact of the choice of the monomer profile	138
8.5	Conclusions	139
9	Electrokinetics in nanochannels grafted with backbone-charged polyelectrolyte brushes	141
9.1	Introduction	142
9.2	Theory	143
9.2.1	Derivation of the Governing Equations for the Equilibrium Brush Height	143
9.2.2	Non-dimensionalization and analytical solutions for the Equilibrium Brush Height	147
9.2.3	Numerical Solutions for the Equilibrium Brush Height	149
9.2.4	Calculation of the EOS transport	150
9.3	Results	150
9.3.1	Free Energy Variation and Equilibrium Brush Height: Results from Analytical Solution	150
9.3.2	Equilibrium Brush Height: Results from Numerical Solution	153
9.3.3	Electrostatics and electroosmotic transport: Numerical results	154
9.4	Conclusions	159
10	Summary, impact of the present thesis, and scope of future research	160
10.1	Key contributions: Summary and Impact	160
10.2	Scope of future research	163
	Bibliography	166

List of Tables

5.1	Order of magnitude for θ for nano-confined stiff polymer brushes using eq.(5.15). We consider $\kappa \sim 10^{-28} \text{ J.m}$ and $\eta = 10^{-3} \text{ Pa.s}$	70
5.2	Order of magnitude for θ for nano-confined semi-flexible polymer brushes using eq.(5.15). We consider $\kappa \sim 10^{-28} \text{ J.m}$ and $\eta = 10^{-3} \text{ Pa.s}$	71
9.1	Summary of the findings for EOS transport for nanochannels with BBC and end-charged brushes. Here u_B , u_{NB} , $u_{B,EC}$, $u_{B,BBC}$, $u_{B,LC}$, and $u_{B,SC}$ respectively denote EOS velocity in nanochannels grafted with brushes, no-brushes, end-charged brushes, backbone-charged brushes, brushes in presence of large salt concentration, and brushes in presence of small salt concentration.	158

List of Figures

1.1	Schematic of polymer brushes grafted at the solid-liquid interface (left) and the backbone of another polymer (right). This figure has been reproduced from Das et al. [5]	3
1.2	Schematic showing (a) interfaces, (b) nanochannels, and (c) spherical particles grafted with negatively charged PE brushes. The charges on the PE brushes are screened by the electrolyte ions forming the Electric Double Layer or the EDL. This figure has been reproduced from Das et al. [5]	4
2.1	Variation of σ^* , σ_h , and σ_c with N_p for (a) grafted PAA chains and (b) grafted λ -DNA chains. The hashed zones in both the plots represent the $\sigma - N_p$ phase space that simultaneously ensure $d < h$ and that the grafted PEs form brush-like configurations. Also these hashed zones are divided into zone I (where $\sigma > \sigma_c$, and hence $\Delta F_{PEB,elec} < \Delta F_{PEB,ent}$) and zone II (where $\sigma < \sigma_c$, and hence $\Delta F_{PEB,elec} > \Delta F_{PEB,ent}$). In these simulations, we use $a_k = 1.5 \text{ nm}$ and $t = 0.4 \text{ nm}$ for PAA chains, whereas $a_k = 100 \text{ nm}$ and $t = 2.5 \text{ nm}$ for DNA chains. Also σ_h is computed for the both the cases considering $h = 100 \text{ nm}$. This figure is taken from Chen and Das [8].	23
3.1	Schematic of the nanochannel grafted with (a) negatively charged PE layer and (b) positively charged PE layer.	30
3.2	Variation of the dimensionless hydrogen ion number density (top panel) and the dimensionless electrostatic potential profile (bottom panel) for the case of uniform distribution of PCS. For all the figures we maintain the four parameters (i.e., $\bar{n}_{H^+, \infty}$, $\bar{\gamma}$, $\bar{\lambda}$, and \bar{K}'_a) as equal to unity and $\bar{d} = 0.3$ except for (a) $\bar{n}_{H^+, \infty} = 0.1, 1, 10$ (b) $\bar{\gamma} = 0.1, 1, 10$ (c) $\bar{\lambda} = 0.2, 1, 10$ (d) $\bar{d} = 0.1, 0.3, 0.5$ and (e) $\bar{K}'_a = 0.1, 1, 10$. In all the figures, the value of the parameter (which is being varied) is indicated. This figure is taken from Chen and Das [56].	38

3.3	Profiles of the cubically varying PCS distribution for various dimensionless PE layer thickness \bar{d} . In the inset we schematically differentiate between (a) the case of uniform PCS distribution and (b) the case of cubic PCS distribution. This figure is taken from Chen and Das [5].	42
3.4	Variation of the dimensionless hydrogen ion number density (top panel) and the dimensionless electrostatic potential profile (bottom panel) for the case of uniform distribution of PCS. For all the figures we maintain the four parameters (i.e., $\bar{n}_{H^+, \infty}$, $\bar{\gamma}$, $\bar{\lambda}$, and \bar{K}'_a) as equal to unity, $\bar{d} = 0.3$, and $\beta = 150$ except for (a) $\beta = 100, 150, 400$, (b) $\bar{n}_{H^+, \infty} = 0.1, 1, 10$, (c) $\bar{\gamma} = 0.1, 1, 10$, (d) $\bar{\lambda} = 0.2, 1, 10$, (e) $\bar{d} = 0.1, 0.3, 0.5$, and (f) $\bar{K}'_a = 0.1, 1, 10$. In all the figures, the value of the parameter (which is being varied) is indicated. This figure is taken from Chen and Das [56].	44
4.1	Schematic of the nanochannel grafted with (a) negatively charged PE layer and (b) positively charged PE layer. The schematic also shows the direction of the applied electric field that triggers the nanochannel ionic current. The figure is taken from Chen and Das [8].	51
4.2	(a) Variation of the ionic current with pH_∞ for different values of pK_a for a negatively charged PE layer. Here we consider the electrolyte salt as $NaCl$ and the acid as HCl . The relevant unsigned mobility values are $\mu_+ = \mu_{Na^+} = 5 \times 10^{-8} m^2/Vs$, $\mu_- = \mu_{Cl^-} = 7.9 \times 10^{-8} m^2/Vs$, $\mu_{H^+} = 36 \times 10^{-8} m^2/Vs$, and $\mu_{OH^-} = 20 \times 10^{-8} m^2/Vs$. (b) Variation of the dimensionless number density of H^+ ion ($\bar{n}_{H^+, \infty}$) and the dimensionless electrostatic potential ($\bar{\psi}$) (shown in the inset) with \bar{y} for different values of pH_∞ for $pK_a = 4$. (c) Variation of the dimensionless number density of H^+ ion ($\bar{n}_{H^+, \infty}$) and the dimensionless electrostatic potential ($\bar{\psi}$) (shown in the inset) with \bar{y} for different values of pK_a for $pH_\infty = 4$. (d) Variation of the dimensionless ionic currents with pH_∞ due to different ions [$\bar{i}_+ = \frac{i_+}{eE\mu_+n_\infty h}$, $\bar{i}_- = \frac{i_-}{eE\mu_+n_\infty h}$, $\bar{i}_{H^+} = \frac{i_{H^+}}{eE\mu_+n_\infty h}$, $\bar{i}_{OH^-} = \frac{i_{OH^-}}{eE\mu_+n_\infty h}$] for $pK_a = 6$. For all the plots, we use $c_\infty = 10^{-4} M$ (i.e., $n_\infty = c_\infty \times N_A \times 10^3 = 6.023 \times 10^{22} 1/m^3$), $\gamma_a = 10^{-4} M$, $\bar{d} = 0.3$, $h = 100 nm$, $k_B T = 4.14 \times 10^{-21} J$, $e = 1.6 \times 10^{-19} C$, $\epsilon_0 = 8.8 \times 10^{-12} F/m$, and $\epsilon_r = 79.8$.	52
4.3	Variation of the ionic current with pH_∞ for a negatively charged PE layer for $pK_a = 4$ and for different values of \bar{d} , γ_a , and c_∞ . Other parameters, including the unsigned mobility values of the different ions, are identical to that used in Fig. 4.2.	54
5.1	Schematic of the electroosmotic flow profile in a PE-grafted nanochannel. The PE ions are shown in green.	59

5.2	Variation of (a) dimensionless hydrogen ion number density, (b) dimensionless electrostatic potential, and (c) dimensionless electroosmotic velocity profile for various bulk pH or pH_∞ values, namely $pH_\infty = 4, 5, 6$. Other parameters used to generate the figures are $c_\infty = 10^{-4} M$, $\bar{d} = 0.3$, $\gamma_a = 10^{-4} M$, $pKa = 4$, $h = 100 \text{ nm}$, $\alpha = 1$, $u_r = 1$, $N_p a_k^3 \sigma / d = 1$, $k_B T = 4.14 \times 10^{-21} \text{ J}$ and $e = 1.6 \times 10^{19} C$	64
5.3	Variation of (a) dimensionless hydrogen ion number density, (b) dimensionless electrostatic potential, and (c) dimensionless electroosmotic velocity profile for different pK_a values, namely $pKa = 4, 5, 6$ for $pH = 4$. Other parameters used to generate the figures are identical to Figure 5.2	64
5.4	Variation of (a) dimensionless hydrogen ion number density, (b) dimensionless electrostatic potential, and (c) dimensionless electroosmotic velocity profile for different sets of parameter space. Other parameters used to generate the figures are $pH = 4$, $pKa = 4$, $h = 100 \text{ nm}$, $\alpha = 1$, $u_r = 1$, $N_p a_k^3 \sigma / d = 1$, $k_B T = 4.14 \times 10^{-21} \text{ J}$ and $e = 1.6 \times 10^{19} C$	65
5.5	Variation of the ratio i_{eos}/i_{ion} for the cases with pH-dependent and pH-independent PE charge density. All the parameters are identical to that used in Fig. 5.2 and 5.3	69
5.6	Schematic of the flow induced deformation of the PE brush. The deformation is quantified by the angle θ . The flow is parallel to the grafting surface.	69
6.1	Schematic of the nanochannel grafted with end-charged PE layer.	78
6.2	(a) Variation of the brush height d_0 (brush height without the electrostatic effects) and d (brush height with electrostatic effects) with electrolyte ion concentration (c_∞) for different values of PE brush end charge density (σ_{ch}) for nanoconfined weakly end-charged, pH-non-responsive PE brushes. Results are shown corresponding to two different (constant) values of d_0 ; for one value, $d_0 < h/2$ (for this case $\ell = 80 \text{ nm}$, where ℓ is the distance of separation between grafted PEs) while for the other value, $d_0 > h/2$ (for this case $\ell = 22 \text{ nm}$). (b) Transverse variation of the dimensionless electrostatic potential [$\bar{\psi} = e\psi/(k_B T)$] for different combinations of c_∞ and σ values for $d_0 < h/2$ and $\ell = 80 \text{ nm}$ (plots that show change in sign of the slope for \bar{y} values such that $-1 < \bar{y} < -0.5$) as well as for $d_0 > h/2$ and $\ell = 22 \text{ nm}$ (plots that show change in sign of the slope for \bar{y} values such that $-0.5 < \bar{y} < 0$). Although we provide the variation of $\bar{\psi}$ for these chosen combinations of c_∞ , σ and d_0 , we have checked and ensured that $ \bar{\psi} < 1$ for the entire parameter space studied in (a). (c) Variation of $\delta\bar{F}/\delta\bar{d}$ and its different components with \bar{d} . Parameters for (c) are $c_\infty = 10^{-4} M$, $\sigma_{ch} = 8 \times 10^{-4} C/m^2$, $d_0 < h/2$ and $\ell = 80 \text{ nm}$. The point where $\delta\bar{F}/\delta\bar{d}$ crosses the \bar{d} axis from negative to positive value denotes the equilibrium \bar{d} . Other parameters used in (a)-(c) are $h = 100 \text{ nm}$, $N_p = 2000$, $a_k = 1 \text{ nm}$, and $\chi = 0.4$	89

6.3	Dimensionless PE brush height (\bar{d}) dependent variation of the electrostatic energy \bar{F}_{elec} for different values of c_∞ and σ_{ch} . Parameters are identical to those used for Fig. 6.2(c).	93
6.4	Variation of the brush height d_0 (brush height without the electrostatic effects) and d (brush height with electrostatic effects) with (a) ℓ or the distance of separation between adjacent grafted PE brushes (for this case, $h = 100 \text{ nm}$, $N_p = 2000$, $a_k = 1 \text{ nm}$ and $\chi = 0.4$), (b) h or nanochannel half height (for this case $\ell = 50 \text{ nm}$, $N_p = 2000$, $a_k = 1 \text{ nm}$ and $\chi = 0.4$), and (c) N_p or PE size (here $h = 100 \text{ nm}$, $\ell = 50 \text{ nm}$, $a_k = 1 \text{ nm}$ and $\chi = 0.4$). For each of (a)-(c), variation of d is shown for different values of PE brush end charge density (σ_{ch}) and electrolyte concentration (c_∞). The figure is for nanoconfined, weakly end-charged, pH-non-responsive PE brushes.	95
6.5	<i>Case for $d_0 < h/2$ for nanoconfined, end-charged, pH-responsive PE brushes:</i> (a) Variation of the brush height with salt concentration and pH. (b) Transverse variation of the dimensionless electrostatic potential ($\bar{\psi}$) for different combinations of salt concentration and pH. Parameters used for these plots are $N_p = 2000$, $\ell = 80 \text{ nm}$, $\sigma_{ch} = -0.0008C/m^2$, $d_0 = 34 \text{ nm}$, $pK_a = 4$, $h = 100 \text{ nm}$, $\chi = 0.4$, $a_k = 1 \text{ nm}$, $k_B = 1.38 \times 10^{-23} \text{ J/K}$, $T = 300 \text{ K}$, $e = 1.6 \times 10^{-19} \text{ C}$, $\epsilon_0 = 8.8 \times 10^{-12} \text{ F/m}$, $\epsilon_r = 79.8$	99
6.6	Variation of $\bar{F}_{elec} = \bar{F}_{B,elec} + \bar{F}_{EDL}$ with \bar{d} for different salt concentrations (expressed in M).The result is shown for $pH = 6$. All other parameters are identical to that used in Fig. 6.5.	100
6.7	<i>Case for $d_0 > h/2$ for nanoconfined, end-charged, pH-responsive PE brushes:</i> (a) Variation of the brush height with salt concentration and pH. (b) Transverse variation of the dimensionless electrostatic potential ($\bar{\psi}$) for different combinations of salt concentration and pH. Parameters used for these plots are $\ell = 22 \text{ nm}$ and $d_0 = 82 \text{ nm}$. All other parameters are identical to that used in Fig. 6.5.	100
7.1	Salt-concentration and pH induced variation of the ionic current [in $A/(Vm)$ or S/m] per unit nanochannel cross sectional area per unit applied axial electric field in nanochannels grafted with end-charged and pH-responsive PE brush for the case where $d_0 < h/2$. Parameters used for these plots are $N_p = 2000$, $\ell = 80 \text{ nm}$, $\sigma_{ch} = -0.0008C/m^2$, $d_0 = 29 \text{ nm}$, $pK_a = 4$, $h = 100 \text{ nm}$, $\chi = 0.4$, $a_k = 1 \text{ nm}$, $k_B = 1.38 \times 10^{-23} \text{ J/K}$, $T = 300 \text{ K}$, $e = 1.6 \times 10^{-19} \text{ C}$, $\epsilon_0 = 8.8 \times 10^{-12} \text{ F/m}$, $\epsilon_r = 79.8$	109
7.2	Salt-concentration and pH induced variation of the ionic current [in $A/(Vm)$ or S/m] per unit nanochannel cross sectional area per unit applied axial electric field in nanochannels grafted with end-charged and pH-responsive PE brush for the case where $d_0 > h/2$. Parameters used for these plots are $\ell = 15 \text{ nm}$ and $d_0 = 88.2 \text{ nm}$. All other parameters are identical to that used in Fig. 7.1.	110

7.3	Difference in the ionic current (per unit width of the nanochannel per unit applied electric field) between the taller (case studied in Fig. 7.2) and the shorter (case studied in Fig. 7.1) brushes. This difference in ionic current has units of $A/(Vm)$ or S/m	111
8.1	Schematic depicting the electroosmotic transport in (a) nanochannels free of PE brushes and (b) nanochannels grafted with end-charged PE brushes. The schematic categorically represents the enhancement of the strength of the EOS transport in nanochannels grafted with end-charged PE brushes.	118
8.2	Variation of the magnitude of the dimensionless transverse EDL electrostatic potential $ \bar{\psi} $ (top panel), transverse counterion number density n_+ (middle panel), and transverse coion number density n_- (bottom panel) as functions of the bulk salt concentrations for pH=7. Results are shown for a) nanochannels grafted with short-loose brushes ($N_p = 2000$, $\ell = 80$ nm, $d_0 = 34$ nm), b) nanochannels grafted with short-loose, but slightly taller brushes ($N_p = 2800$, $\ell = 80$ nm, $d_0 = 49$ nm), c) nanochannels grafted with short-dense brushes $N_p = 846$, $\ell = 22$ nm, $d_0 = 34$ nm, d) nanochannels grafted with tall-dense brushes $N_p = 2000$, $\ell = 22$ nm, $d_0 = 82$ nm, and (e) nanochannels grafted with no brush. Other parameters for all the figures are identical to that in Fig. 6.5.	122
8.3	Variation of the transverse electroosmotic velocities as functions of the bulk salt concentrations for pH=7. Results are shown for a) nanochannels grafted with short-loose brushes ($N_p = 2000$, $\ell = 80$ nm, $d_0 = 34$ nm), b) nanochannels grafted with short-loose, but slightly taller brushes ($N_p = 2800$, $\ell = 80$ nm, $d_0 = 49$ nm), c) nanochannels grafted with short-dense brushes ($N_p = 846$, $\ell = 22$ nm, $d_0 = 34$ nm), d) nanochannels grafted with tall-dense brushes ($N_p = 2000$, $\ell = 22$ nm, $d_0 = 82$ nm), and (e) nanochannels grafted with no brush. We represent the loose brushes as light green [see (a) and (b)] and dense brushes as pink [see (c) and (d)]. Other parameters are identical to those in Fig. 8.2.	125
8.4	Variation of the dimensionless per unit volume forces (\bar{f}) in the transverse direction as functions of the bulk salt concentrations for pH=7. Here $\bar{f} > 0$ represents the dimensionless per unit volume EOS body force, while $\bar{f} < 0$ represents the retarding PE-brush-layer-induced per unit volume drag force. Results are shown for a) nanochannels grafted with short-loose brushes ($N_p = 2000$, $\ell = 80$ nm, $d_0 = 34$ nm), b) nanochannels grafted with short-loose, but slightly taller brushes ($N_p = 2800$, $\ell = 80$ nm, $d_0 = 49$ nm), c) nanochannels grafted with short-dense brushes ($N_p = 846$, $\ell = 22$ nm, $d_0 = 34$ nm), d) nanochannels grafted with tall-dense brushes ($N_p = 2000$, $\ell = 22$ nm, $d_0 = 82$ nm), and (e) nanochannels grafted with no brush. Other parameters are identical to those in Fig. 8.2.	128

8.5	Transverse variation of $ \bar{\psi} $ (magnitude of dimensionless electrostatic potential), \bar{u} (dimensionless EOS velocity), \bar{f} ($\bar{f} > 0$ represents the dimensionless per unit volume EOS body force, while $\bar{f} < 0$ represents the retarding PE-brush-layer-induced per unit volume drag force), n_+ (counterion number density), n_- (coion number density), and n_{H^+} (number density of hydrogen ions). Results are shown for nanochannels grafted with short-loose brushes ($N_p = 2000$, $\ell = 80 \text{ nm}$, $d_0 = 34 \text{ nm}$) for (a) pH=3, (b) pH=4, and (c) pH=5. Other parameters are identical to those in Fig. 8.2.	131
8.6	Transverse variation of $ \bar{\psi} $ (magnitude of dimensionless electrostatic potential), \bar{u} (dimensionless EOS velocity), \bar{f} ($\bar{f} > 0$ represents the dimensionless per unit volume EOS body force, while $\bar{f} < 0$ represents the retarding PE-brush-layer-induced per unit volume drag force), n_+ (counterion number density), n_- (coion number density), and n_{H^+} (number density of hydrogen ions). Results are shown for nanochannels grafted with short-loose, but slightly taller brushes ($N_p = 2800$, $\ell = 80 \text{ nm}$, $d_0 = 49 \text{ nm}$) for (a) pH=3, (b) pH=4, and (c) pH=5. Other parameters are identical to those in Fig. 8.2.	132
8.7	Transverse variation of $ \bar{\psi} $ (magnitude of dimensionless electrostatic potential), \bar{u} (dimensionless EOS velocity), \bar{f} ($\bar{f} > 0$ represents the dimensionless per unit volume EOS body force, while $\bar{f} < 0$ represents the retarding PE-brush-layer-induced per unit volume drag force), n_+ (counterion number density), n_- (coion number density), and n_{H^+} (number density of hydrogen ions). Results are shown for nanochannels grafted with short-dense brushes ($N_p = 846$, $\ell = 22 \text{ nm}$, $d_0 = 34 \text{ nm}$) for (a) pH=3, (b) pH=4, and (c) pH=5. Other parameters are identical to those in Fig. 8.2.	133
8.8	Transverse variation of $ \bar{\psi} $ (magnitude of dimensionless electrostatic potential), \bar{u} (dimensionless EOS velocity), \bar{f} ($\bar{f} > 0$ represents the dimensionless per unit volume EOS body force, while $\bar{f} < 0$ represents the retarding PE-brush-layer-induced per unit volume drag force), n_+ (counterion number density), n_- (coion number density), and n_{H^+} (number density of hydrogen ions). Results are shown for nanochannels grafted with tall-dense brushes ($N_p = 2000$, $\ell = 22 \text{ nm}$, $d_0 = 82 \text{ nm}$) for (a) pH=3, (b) pH=4, and (c) pH=5. Other parameters are identical to those in Fig. 8.2.	134

8.9	Phase space for iso-volume-flow-rate. The lines with numbers denote the $\ell - N_p$ combinations that ensure identical flow rates with the numbers on the lines denoting the dimensionless flow rate, defined in eq.(8.4). The shaded region shows the $\ell - N_p$ combinations that ensure that the grafted PE molecules form brushes whose heights are less than the nanochannel half height. Below this shaded zone the brushes are taller than the nanochannel half height, while above the shaded zone the grafting is so weak that the grafted polymer molecules no longer form the brushes. Results here are shown for $c_\infty = 10^{-2} M$, $\sigma_{ch} = -8 \times 10^{-4} C/m^2$, and $pH = 7$	136
9.1	(Left) Dimensionless PE brush height (\bar{d}) dependent variation of the total dimensionless electrostatic energy (\bar{F}_{elec}) as well as the electrostatic energies associated with charges on the brush ($F_{B,elec}$) and the induced EDL (\bar{F}_{EDL}). In this plot, we consider $c_\infty = 10^{-3} M$, $\ell = 50 nm$, $h = 100 nm$, $N_p = 100$, $f_{ch} = 1$, $a_k = 1 nm$, $T = 300 K$ and $\chi = 0.4$. (Right) Variation of \bar{F}_{elec} with \bar{d} for different values of c_∞ . All other parameters remain identical.	151
9.2	Variation of the PE brush height (d) with salt concentration for different PE separation distance (ℓ) and number of monomers (N_p). In this plot, we consider $h = 100 nm$, $f_{ch} = 1$, $a_k = 1 nm$, $T = 300 K$ and $\chi = 0.4$. We consider three different values of d_0 (dictated by three different combinations of ℓ and N_p), such that the resulting electrostatics always allows the use of Debye-Hückel linearization. The lines that are parallel to the c_∞ axis represent the $d = d_0$ value (i.e., when the brushes are uncharged).	152
9.3	Numerical solution for the variation of the equilibrium height of the nanoconfined BBC PE brushes as a function of the salt concentration. The different cases identified here are as follow. Case 1: $N_p = 2000$, $\ell = 80$, $d_0 = 34 nm$; Case 2: $N_p = 2800$, $\ell = 80$, $d_0 = 49 nm$; Case 3: $N_p = 846$, $\ell = 22$, $d_0 = 34 nm$; Case 4: $N_p = 2000$, $\ell = 22$, $d_0 = 82 nm$; Case 5: $N_p = 8000$, $\ell = 200$, $d_0 = 75 nm$; Case 6: No brushes. Here we use $f_{ch} = \frac{\sigma_{ch}\ell^2}{eN_p} = (-8 \times 10^{-4} C/m^2) \frac{\ell^2}{eN_p}$. Other parameters are identical to those used in Fig. 9.2.	153
9.4	Transverse variation of $ \bar{\psi} $ (magnitude of dimensionless electrostatic potential), n_+ (counterion number density), n_- (coion number density), \bar{u} (dimensionless EOS velocity), and \bar{f} ($\bar{f} > 0$ represents the dimensionless per unit volume EOS body force, while $\bar{f} < 0$ represents the retarding PE-brush-layer-induced per unit volume drag force) for Case 1 ($N_p = 2000$, $\ell = 80$, $d_0 = 34 nm$) [shown in (a)], Case 2 ($N_p = 2800$, $\ell = 80$, $d_0 = 49 nm$) [shown in (b)], Case 3 ($N_p = 846$, $\ell = 22$, $d_0 = 34 nm$) [shown in (c)], Case 4 ($N_p = 2000$, $\ell = 22$, $d_0 = 82 nm$) [shown in (d)], Case 5 ($N_p = 8000$, $\ell = 200$, $d_0 = 75 nm$) [shown in (e)], and Case 6 (No brushes) [shown in (f)]. Other parameters are identical to those used in Fig. 9.2.	155

Chapter 1: Introduction

In this chapter¹, brief descriptions are first provided to elucidate the fundamental concepts regarding the configuration of the polymer and polyelectrolyte (PE) brushes, applications of interfaces grafted with such brushes, and the state of the art in modelling of polymer and PE brushes. Subsequently, the open questions on the topic that the present thesis intends to address are discussed. Finally, the structure and the organization of the thesis are provided.

1.1 Polymer and polyelectrolyte brushes: Fundamental ideas

Polymer brushes (PBs) are assemblies of polymer chains tethered or grafted by one of their extremities to a surface [Fig. 1.1 (left)] or to the backbone of another polymer chain [Fig. 1.1 (right)] [1–6]. When this density of grafting (referred to as σ through out the thesis) becomes large enough to ensure that the lateral separation between adjacent grafted polymer chains is smaller than their radius of gyration (R_g) in a coiled state (in a “good” solvent), the adjacent brushes interact with each other,

¹Contents of this chapter have been published as: *S. Das, M. Banik, G. Chen, S. Sinha and R. Mukherjee, Polyelectrolyte brushes: theory, modeling, synthesis and applications. Soft Matter, 11, 8550-8583 (2015).*

enforcing the attainment of a “brush” like state instead of the coiled state. This “brush” state, therefore, is attained in order to avoid overlapping between the adjacent grafted polymer molecules ensuring that the grafted polymer molecules stretch in a direction normal to the substrate surface as a “brush”. This stretching typically ensures that the length or height d of the polymer brushes scales linearly with the polymer size (or number of monomers per polymer chain) N_p – this signifies a definite stretching of the polymer molecules as compared to their coiled state where $R_g \sim N_p^\nu$ (with Flory exponent $\nu = 3/5$ for good solvent) [4]. Grafting of such “stretched” polymer molecules in form of “brushes” often results in unique multifunctional and stimuli-responsive surfaces. In the simplest case, the interaction between a brush and the surrounding might simply alter between attractive (switch on) and repulsive (switch off), depending on various simple stimuli such as the type of solvent, pH of the surrounding medium, magnitude of the electrostatic forces, etc. Such a simple effect can have a significant influence on properties like the coefficient of friction, work of adhesion, or wetting, which in turn can modulate cell adhesion and growth, protein adsorption, flow incitation, wetting and dewetting, drug release, control of the membrane permeability of a surface, etc. Polyelectrolytes (or PEs) are polymer molecules containing charges – such charges can be present along the entire backbone of the polymer molecule (e.g., polyacrylic acid or PAA, DNA, etc.) or may be localized only at certain places on the polymer molecule [e.g., end of sulfonic acid terminated poly(ethylene glycol) (PEG) chains [7]]. PE brushes, therefore, are brushes formed by such PE molecules. The PE brushes can be grafted on a single interface [Fig. 1.2(a)], or grafted on the inner walls of a nanochannel [Fig. 1.2(b)], or grafted on spheri-

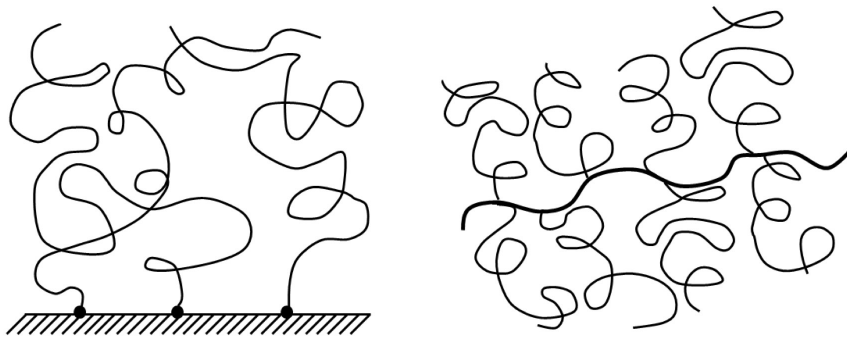


Figure 1.1: Schematic of polymer brushes grafted at the solid-liquid interface (left) and the backbone of another polymer (right). This figure has been reproduced from Das et al. [5]

cal particles [Fig. 1.2(c)]. The basic mechanism of brush formation – namely the close-enough grafting of adjacent polymer molecules enforcing them to form brushes in an effort to avoid mutual overlap – remains identical here. In addition, presence of charges on PE molecules trigger two extremely important effects that have significant implications on the behaviour and functioning of interfaces grafted with PE brushes. Firstly, the free energy of the polymer molecule will now consist of an electrostatic contribution, in addition to the elastic and excluded volume contributions of the uncharged polymer brush [5, 8]. Secondly, under the condition that the PE molecule is in contact with an aqueous solution, this PE charge will enforce the electrolyte ions from the surrounding aqueous solvent to get arranged in a double layer (known as the electric double layer or the EDL) on either sides of the PE-electrolyte interface. These two features can ensure that the PE brushes become far more responsive than the polymer brushes, making them useful for attributing functionalities to the surfaces on which they are grafted for several applications (which are beyond the scope of

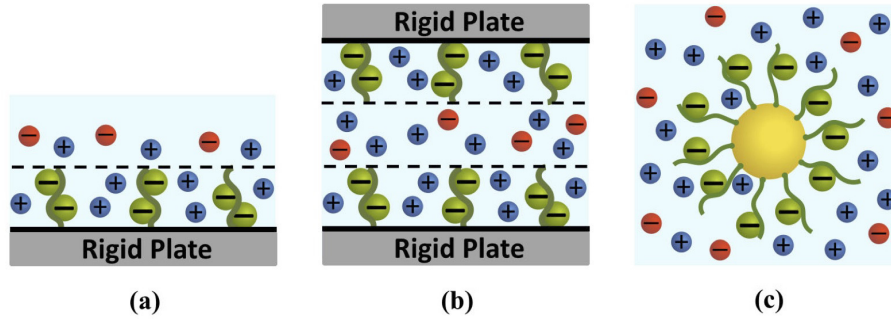


Figure 1.2: Schematic showing (a) interfaces, (b) nanochannels, and (c) spherical particles grafted with negatively charged PE brushes. The charges on the PE brushes are screened by the electrolyte ions forming the Electric Double Layer or the EDL. This figure has been reproduced from Das et al. [5]

surfaces grafted with polymer brushes) such as control of wettability and biocompatibility of surfaces, regulation/manipulation/switching of ion transport, ionic current rectification, developing ionic transistors and diodes, and many more.

The present thesis will focus on a particular aspect of PE brushes, that has received very little attention in context of thermodynamic, electrostatic, and transport modelling. This issue is the theoretical modelling of nanoconfined PE brushes, i.e., PE brushes grafted on the inner walls of a nanofluidic channel. Significance of this modelling effort will be to shed light on how nanoconfined PE brushes behave under different stimuli, which in turn is paramount to explain and control a large number of applications of nanochannels and nanopores functionalized with the PE brushes.

1.2 Polymer and polyelectrolyte brushes: Applications

Grafting of interfaces with polymer and polyelectrolyte brushes allow the interfaces to inherit a variety of functionalities that can be used in different applications depending upon the geometry of the grafting surfaces. For example, flat single interfaces grafted with polymer or PE brushes have been used in applications such as protein analysis and purification [9], fabrication of bioelectronic systems [10], controlling cell adhesion [11] and cell culture [12], regulating proliferation of microorganisms [13], promoting temperature, pH, ion-concentration and light induced wettability changes [14–16], and many more. On the other hand, spherical polymer brushes (or SPBs) can be employed for several other applications. The most important application of these SPBs is in drug delivery; micro/nano particles are functionalized by grafting with polymer brushes, which ensure that these particles can be used as drug carriers that can sense the environmental cues (e.g., specific chemicals secreted by infected cells) for a highly targeted and specific drug delivery [17, 18]. Apart from the drug delivery, SPBs have been used for fabricating “smart” colloidal systems responsive to environmental cues [19], devising enhanced oil recovery techniques [20], preparing stabilized pickering emulsions [21] and superhydrophobic coatings [22], developing new family of colloidal crystals having antibiofouling properties [23], fabricating nanocomposites with tuneable properties [24], and many more.

While the above examples represent the cases for non-confined systems, presence of a confinement (e.g., cases where polymer and PE brushes are grafted on the inner walls of a nanochannel) ensure that such brush-grafted systems can be employed for

applications beyond the capabilities of single brush-grafted interfaces. Some such examples of PE-brush-grafted nanoconfined systems are flow valving [25, 26], ion transport, sensing, and manipulation [27–29], current rectification [30], fabrication of nanofluidic diodes [31, 32], sensing and detection of biomolecules [33, 34], designing of energy converters [35], and many more.

1.3 Theoretical modelling of polymer and polyelectrolyte brushes

1.3.1 State-of-the-art methods

There have been three distinct directions of theoretical and numerical modelling of polymer and PE brushes. Firstly, as with virtually all problems involving polymers, there has been significant research in developing scaling models for both linear and spherical polymer and PE brushes elucidating a number of issues such as brush height in “good” and “poor” solvent, monomer distribution [4–6, 8, 36–38], etc.

A more detailed theoretical modelling invoking self consistent field theory (SCFT) has also been extensively studied in context of describing the behaviour of polymer and PE brushes [38–46]. This theoretical approach becomes useful when predicting the distribution of monomer number density, spatial distribution of the ends of the polymer brushes and fluctuations of these brush ends, effect of local elastic extension, etc. Under certain conditions (for example, when the chains are strongly stretched) the SCFT can be simplified, and it becomes possible to solve the problem of polymer brushes using the strong stretching theory (or SST) [44–46] – main advantage of SST over SCFT is that it allows a much easier analytical calculability of the governing

equations describing the polymer and PE brushes, while the SCFT theory invariably involves numerical calculations.

Finally, there has been considerable mesoscopic (methods such as Brownian simulations) and atomistic simulations to unravel various aspects of polymer and PE brushes beyond the capabilities of scaling and mean field calculations. Some of these issues are effect of explicit distribution of electrolyte ions in the configuration of PE and transition of PE from single to multiple chains [112], morphologies of PE brushes in poor solvent [48], configurations of bottle-brush PEs [49], interaction and friction between layers of charged and neutral polymer brushes and bottlebrush polymers [50], configuration of spherical brushes [51], and many more.

1.3.2 Open questions and main agenda of the thesis

Despite such significant progress in multiscale modelling of the behavior of PE brushes, there are several issues that have received substantially inappropriate attention. The present thesis plans to shed light on three of such important issues. These issues are (a) continuum scale quantification of the morphology and the electrostatics of nanoconfined PE brushes, i.e., PE brushes grafted on inner wall of a nanochannel, with specific attention to the role played by the confinement effects and the conditions that allow decoupling of the electrostatic effects from the non-electrostatic ones, (b) modelling of the pH-dependent electrostatics of these PE brushes and the resulting electrokinetics (electric field mediated ion and liquid transport) in the decoupled regime, and (c) developing mean field models to probe the nanoconfined PE config-

uration and electrostatics and the resulting electrokinetics in the coupled (i.e., when the electrostatic and non-electrostatic effects are coupled) regime.

There has been very little continuum-based modelling of nanoconfined PE brushes. Existing relevant papers [52, 53] rarely shed enough light on the role played by the nanoconfinement effects in the morphology and the electrostatics of the PE brushes. In other words, the effect of parameters such as the relative thickness of the PE brush with respect to the nanochannel half height or possible EDL overlap effects in nanochannels has been rarely investigated in context of nanoconfined PE brush morphology and electrostatics. The first agenda of the thesis will be to develop scaling laws that will pinpoint the role of nanoconfinement in dictating the PE brush morphology and at the same time pinpoint the conditions that will allow decoupling of the electrostatic and the non-electrostatic effects that govern the PE brush behavior. For an appropriately selected parameter space that allows such decoupling, it will require only the solution of the electrostatics problem in order to establish all the significant influences of the EDL in the overall PE brush behavior.

This same decoupling condition will enable a much easier probing of the pH-responsiveness of the PE brushes, as has been done in the present thesis. Such pH-responsiveness allows a triggering of pH-dependent electrostatics and morphological changes in these brushes, making them capable of several novel applications across different disciplines [54, 55]. This has prompted several authors to theoretically model the PE brushes with pH-dependent ionization and charging. The second agenda of this thesis will be to unravel how these existing theoretical studies on pH-responsive PE brushes have failed to account for the appropriate consideration of the H^+ ion con-

centration in the description of the electrostatics of such pH-responsive PE brushes – such inappropriateness stems from the use of Boltzmann distribution to describe the H^+ ion concentration within the PE layer, without using the appropriate free energy minimization consideration to predict the H^+ ion concentration. Such inadequacy leads to catastrophic physical discontinuities in the profiles of H^+ ion concentration. The present thesis proposes a correction in the PE brush monomer distribution that accounts for this physical discrepancy – this monomer distribution is subsequently used to probe the electrokinetics (ionic current and electroosmotic or EOS transport in presence of an applied external electric field) in PE-grafted nanochannels in the decoupled regime elucidating massively dominant ionic current and severely suppressed EOS transport.

The final agenda of the thesis will be to develop mean field models to probe the electrostatics and configuration of nanoconfined PE brushes in the *coupled regime*, i.e., the regime where the electrostatic and non-electrostatic effects are coupled. Subsequently, these PE brush electrostatics and configuration will be used to obtain the ionic current and the EOS flow in nanochannels grafted with these PE brushes – therefore, for the first time continuum scale models that account for the appropriate PE brush configuration and thermodynamics will be invoked to quantify the electrokinetics in soft nanochannels. Both end-charged PE brushes (i.e., brushes containing charges only at their non-grafted ends) as well as backbone-charged brushes (brushes containing charges along their entire backbone) will be considered.

Therefore, this thesis will shed light for the first time on how pH-dependent ionization, salt-dependent electrostatics, and most importantly, the confinement ef-

fects interplay with the non-electrostatic effects of the PE molecule to govern (a) the configuration of the nanoconfined PE brushes and (b) electrokinetic transport in nanochannels grafted with such brushes. It is anticipated that these results will significantly influence the design and performance of PE-brush-grafted nanochannels in terms of applications such as ion sensing, ion manipulation, ionic current rectification, and flow valving.

1.4 Organization of the thesis

The rest of the thesis is organized as follows.

In the *second chapter*, new scaling laws for the nanoconfined PE brushes are proposed [8]. These scaling laws identify (a) the conditions that demarcate between the coupled and de-coupled regimes in the description of the PE brushes and (b) the conditions that enforce that grafted polymer molecules can form brushes whose height do not exceed the nanochannel half height (so that there is no overlap of the brushes from opposite walls).

In the *third chapter*, the electrostatics of the pH-responsive PE brushes in the decoupled regime are probed [56]. This chapter develops the free-energy-based framework that accounts for the first time an appropriate variation of the H^+ ion concentration in the electrostatics of the pH-responsive PE brushes. This chapter further quantifies the role of nanoconfinement in such a description.

In the *fourth chapter*, calculations are provided for the ionic current in nanochannels with such pH-responsive brushes described in the decoupled regime [8].

In the *fifth chapter*, the electroosmotic transport in such nanochannels with pH-responsive brushes are probed [26]. Here too a decoupled regime is considered. Additionally, in this chapter a scaling law is provided to establish why one can neglect the flow-induced PE brush deformation over such nanoscales. The main finding of this chapter is to unravel a unique electroosmotic transport that is remarkably suppressed, which in turn makes such nanochannel potentially popular candidates for ion sensing and current rectification.

In the *sixth chapter*, calculations are provided for the first time for the *coupled regime*. The PE brushes are considered to be end-charged – how the resultant electrostatics (of the PE brush and the resulting EDL) interplay with the PE elastic and excluded volume effects to dictate a given nanoconfinement-induced brush height is explored [57]. The key finding is the *hitherto unknown*, highly non-intuitive dependence of the end-charged PE brush height on the salt concentration.

In the *seventh chapter*, ionic current for nanochannels grafted with end-charged PE brushes and described in the coupled regime is considered. Distinct effects of the salt concentration and pH (assuming the mechanism that produces the end charge to be pH-responsive) on the ionic current is revealed.

In the *eighth chapter*, EOS transport in nanochannels grafted with end-charged PE brushes is explored. Here too a coupled regime is considered. Most importantly, the brushes ensure a most remarkable augmentation in the strength of the EOS transport in nanochannels grafted with such brushes – the results are attributable to the localization of the EDL and the EDL-mediated EOS body force at the brush tip.

In the *ninth chapter*, ionic current and EOS flow in nanochannels grafted with backbone-charged brushes, with the brushes being modelled in the coupled regime, are calculated.

Finally, in the *tenth chapter*, summary and impact of the findings of the present thesis and the scope of the future work are provided.

Chapter 2: Nanoconfined Polyelectrolyte brushes: Scaling laws

In this chapter¹, new scaling laws for nanoconfined polyelectrolyte (PE) brushes have been developed. These scaling laws identify the optimal combination of the grafting density (σ) and the polymer size (N_p) that ensure that the grafted PE molecules simultaneously attain the brush-like configurations and a brush height that is less than half the nanochannel height. We further develop scaling conditions that allow decoupling (the corresponding regime is called the decoupled regime) of the elastic (or entropic) and excluded volume effects of the PE brushes from the electrostatic effects associated with the PE charges and the induced electric double layer (or EDL). For such a decoupled regime, the PE brush height is dictated exclusively by the balance of the elastic (or entropic) and the excluded volume effects and the electrostatic effects are described for a constant PE brush height. Finally, these scaling regimes are demonstrated for brushes formed by the polyacrylic acid (PAA) and the DNA.

¹Contents of this chapter have been published as: *G. Chen and S. Das, Scaling laws and ionic current inversion in polyelectrolyte-grafted nanochannels. J. Phys. Chem. B, Vol. 119, pp. 12714-12726 (2015).*

2.1 Introduction

The foundation of polymer physics rests on describing the behaviour of polymer molecules through the lens of “scaling laws”. These scaling laws provide universally applicable description of polymer configuration in a plethora of different states. Therefore, through “scaling laws”, we can explain how the dimensions of a polymer molecule differ between a coiled state (witnessed in a “good” solvent) and a globule state (witnessed in a “poor” solvent). The cases of polymer and PE brushes are no different. Such scaling laws allow us to infer that the polymer brushes demonstrate a height d that varies linearly with the polymer size N_p [4,6] – this is in sharp contrast to the polymer in a coiled-state in a “good” solvent, where the polymer dimension (quantified by the radius of gyration R_G) scales as $N_p^{3/5}$. Similarly, it is observed that $d \sim \sigma^{1/3}$, confirming the enhancement in the brush height due to the augmentation of the grafting density. With regards to polymer and PE brushes, there are several other useful scaling laws that describe the behavior and the configuration of polymer and PE brushes under several different conditions pertaining to the quality of the solvent and the geometry of the grafting interface [36–38].

This chapter focuses on scaling calculations of the polymer and PE brushes for two specific scenarios that have not yet received proper attention (in context of scaling calculations), but forms the foundational basis for this thesis. Firstly, the scaling laws are proposed to demarcate the “decoupled regime”. The equilibrium of a PE brush molecule is governed by the balance of four effects, namely the elastic, excluded volume, and electrostatic effect associated with the PE molecule and the electrostatic

effect associated with the formation of an electric double layer (or EDL) on either sides of the PE-electrolyte interface [see Fig. 1.2] [4, 5, 45, 46]. By “decoupled” regime, we refer to the regime where the elastic and the excluded volume effects of the PE brushes can be decoupled from the electrostatic effects of the PE brush and the induced EDL. In this regime, the PE brush height is governed strictly by the balance of the elastic and the excluded volume effects, and consequently the electrostatic effects can be described by assuming a constant value of the PE brush height. We identify that attainment of this regime is dictated solely by the properties of the PE brush molecule. Most remarkably, there have been a vast number of studies that have investigated the electrostatics of PE brushes by considering a constant (or an electrostatic-effect-independent) value of the brush height (see the review articles in Refs. [58–64] and the papers cited in these review articles) – this proposed scaling calculation identifies the conditions where these calculations will be valid for planar PE brushes. In the next part of the thesis (Chapters 3-5) describes the thermodynamics, electrostatics, and transport of the nanoconfined PE brushes exclusively in this “decoupled” regime – this makes it all the more necessary to identify the conditions for the attainment of the decoupled regime. In the final part part of the thesis (Chapter 6-9), our analysis will describe the behaviour of the nanoconfined PE brushes under the condition where all the four effects describing the PE brush equilibrium mutually affect each other.

The scaling conditions are next developed to incorporate the “nanoconfinement” effect in the description of the PE brushes. In other words, we pinpoint the conditions that ensure that the PEs grafted on the inner walls of the nanochannel simultaneously attain a “brush” configuration and also attain a height that is smaller than the

nanochannel half height. The proposed scaling laws help to discern the appropriate corresponding combination of σ and N_p – therefore, it becomes possible to identify the necessary $\sigma - N_p$ phase space for a given polymer or PE (here we consider polyacrylic acid or PAA and λ -DNA) corresponding to which one will encounter non-interfering and non-penetrating nanoconfined polymer or PE brushes.

2.2 Scaling Laws for a polyelectrolyte-grafted nanochannel

We consider a nanochannel (height $2h$) grafted with a PE layer (height d and grafting density σ) on each of its walls. The PE layer can be either negative or positively charged [for example, Fig. 1.2(b) shows the case of nanochannel grafted with negatively charged PE brushes]. We shall derive the scaling laws for this nanochannel. But prior to that, we repeat some of the well-known concepts on scaling of polymer brushes and the selection of the equilibrium thickness d_{PB} of the polymer brushes. All grafted polymer systems do not form brushes; rather brushes are formed only when the separation between the two adjacent grafted polymer layers (quantified as $\sigma^{-1/2}$) is smaller than a critical separation distance ($\sigma^{*-1/2}$). The involved physics has been beautifully explained by Milner [6]. Here we briefly summarize that explanation. In a good solvent, the grafted polymer chains demonstrate two mutually contesting tendencies, namely adoption of random-walk configurations and getting maximum exposure and wetting by the solvent. While the first tendency maximizes the configurational entropy and favours short-length and dense brushes, taller and sparse brushes better satisfy the second tendency. For grafted polymer systems, in

case the distance between two adjacent grafted molecules ($\sigma^{-1/2}$) is much smaller than $\sigma^{*-1/2}$, these above two tendencies cannot be satisfied simultaneously. Consequently, the chain stretches out as a “brush” (or in other words, chooses a height d) so as to minimize the total energy by balancing these two tendencies. As has been hypothesized by several other researchers, this critical distance ($\sigma^{*-1/2}$), therefore, should be equal to the radius of gyration of the polymer chain $R \sim a_k N_p^\nu$ (where a_k is the polymer Kuhn length, N_p is the number of monomers in one polymer chain, and the flory exponent $\nu = 3/5$ for the case when the chain is in a “good” solvent). Therefore:

$$\sigma^{*-1/2} \sim a_k N_p^{3/5} \Rightarrow \sigma^* \sim a_k^{-2} N_p^{-6/5}. \quad (2.1)$$

Hence in order to ensure that the polymer grafting leads to formation of brushes, one must have

$$\sigma > \sigma^*. \quad (2.2)$$

Please note that throughout this chapter as well as the rest of the thesis, we shall consider the Kuhn length as a constant, specific to the polymer or PE. In other words, we do not account for the contribution of the electrostatic effects in altering the persistence length for a PE molecule.

For a grafted polymer chain in a brush-like configuration (with a brush height equal to d_{PB}), the free energy can be expressed as:

$$\Delta F_{PB} = \Delta F_{PB,ent} + \Delta F_{PB,VE} \sim k_B T \left[\frac{3}{2} \frac{d_{PB}^2}{N_p a_k^2} + \omega N_p \left(\frac{N_p \sigma}{d_{PB}} \right) \right]. \quad (2.3)$$

In eq.(2.3), $k_B T$ is thermal energy and $\omega = \frac{1-2\chi}{2} a_k^3$ is the excluded volume parameter.

Further the individual free energy contributions are the entropic or chain stretching

contribution ($\Delta F_{PB,ent}$) and the excluded volume contribution ($\Delta F_{PB,VE}$). Finally, the equilibrium height $d_{eq,PB}$ can be obtained by minimizing eq.(2.3) with respect to d_{PB} , yielding:

$$d_{eq,PB} \sim N_p \left(\frac{\omega \sigma a_k^2}{3} \right)^{1/3}. \quad (2.4)$$

Eq.(2.4) yields the well-known scaling law for the polymer brush, where the brush height scales linearly with the polymer size N_p .

With this preliminary background on the scaling concepts of polymer brushes, we now focus our attention to the present issue of scaling for the case of nanochannels grafted with PE brushes. Here there are two issues that are different from the simple scaling ideas of polymer brushes introduced above. They are (a) consideration of charges on the polymer (making it a PE), which in turn triggers the formation of an EDL of electrolyte ions around the PE molecule and (b) selection of appropriate N_p and σ such that the resulting brush height remains smaller than the nanochannel half height.

For a single PE brush, the net free energy change is comprised of the free energy changes associated with the grafted PE molecules as well as the induced EDL. Consequently,

$$\Delta F = \Delta F_{PEB} + \Delta F_{EDL} = \Delta F_{PEB,ent} + \Delta F_{PEB,VE} + \Delta F_{PEB,elec} + \Delta F_{EDL}. \quad (2.5)$$

In eq.(2.5), $\Delta F_{PEB,ent}$, $\Delta F_{PEB,VE}$, $\Delta F_{PEB,elec}$ are the free energy changes associated with the entropic, excluded volume, and electrostatic effects of the PE molecule, whereas ΔF_{EDL} is the free energy change associated with the induced EDL. Eq.(2.5) should be minimized in order to obtain the equilibrium height of the PE brushes. But

prior to that, we shall first like to obtain the scaling for $\Delta F_{PEB,elec}$ and how it compares to the other energy components of the brush (i.e., $\Delta F_{PEB,ent}$ and $\Delta F_{PEB,VE}$). Assuming that an electrostatic potential of average magnitude ψ_0 has been triggered around the vicinity of a single grafted PE molecule, we may write $\Delta F_{PEB,elec}$ for that PE molecule as:

$$\Delta F_{PEB,elec} \sim eN_p f_{ch} \psi_0, \quad (2.6)$$

where e is the electronic charge and f_{ch} ($0 < f_{ch} < 1$) represents the fraction of monomers that are charged. Considering ψ_0 to be some multiple (not too small or not too large) of $k_B T/e$, we may re-write eq.(2.7) as:

$$\Delta F_{PEB,elec} \sim k_B T N_p f_{ch}. \quad (2.7)$$

We next try to find out – through scaling arguments – the conditions that will allow us to use eq.(2.4) even for the height d of the PE brush. In other words, these conditions will ensure that the electrostatic contribution of the grafted PE molecule will not contribute to the selection of the PE brush height; accordingly, just like the case of uncharged polymer brushes, d will be selected by the balance of the elastic and the excluded volume energies of the PE molecule. To identify this condition, we take the ratio of $\Delta F_{PEB,elec}$ and $\Delta F_{PEB,ent}$, yielding [see eq.(2.3) for the expression for $\Delta F_{PEB,ent}$]:

$$\frac{\Delta F_{PEB,elec}}{\Delta F_{PEB,ent}} \sim \frac{2 N_p^2 a_k^2 f_{ch}}{3 d^2}. \quad (2.8)$$

Using eq.(2.4) to replace d in eq.(2.8) (the reasons are expressed above), we may write:

$$\frac{\Delta F_{PEB,elec}}{\Delta F_{PEB,ent}} \sim f_{ch} \left(\frac{a_k}{\sigma \omega} \right)^{2/3}. \quad (2.9)$$

Considering the Kuhn segment to be spherical (with radius of a_k), so that $\omega \sim a_k^3$, we may re-write eq.(2.9) as:

$$\frac{\Delta F_{PEB,elec}}{\Delta F_{PEB,ent}} \sim f_{ch} \left(\frac{1}{\sigma a_k^2} \right)^{2/3}. \quad (2.10)$$

Eq.(2.10) provides the critical value of the grafting density, referred to as σ_c . Note that this critical value is different from the critical value σ^* that dictates the attainment of “brush”-like configuration. The σ_c dictates the relative influence of the electrostatic and the entropic effects of the grafted PE molecule, which in turn governs whether or not the electrostatic effects of the PE molecule influence the selection of the PE brush height. From eq.(2.10), we can express σ_c as [σ_c is defined as $(\frac{\Delta F_{PEB,elec}}{\Delta F_{PEB,ent}})_{\sigma=\sigma_c} \sim 1$]:

$$\sigma_c \sim \frac{f_{ch}^{3/2}}{a_k^2}. \quad (2.11)$$

Therefore, the PE electrostatic effects become comparable to the entropic (and excluded volume effects) only when $\sigma \approx \sigma_c$. This is the case for which the PE electrostatic effects will influence the selection of the PE brush height, assumed to be selected by the balance of the entropic and the excluded volume effects of the PE. On the other hand, for $\sigma \ll \sigma_c$, $\Delta F_{PEB,elec} \gg \Delta F_{PEB,ent}$, whereas for $\sigma \gg \sigma_c$, $\Delta F_{PEB,elec} \ll \Delta F_{PEB,ent}$. For both these cases (i.e., $\sigma \ll \sigma_c$ and $\sigma \gg \sigma_c$), we can consider a decoupled regime, i.e., the electrostatic effects do not influence the selection of the PE brush thickness. Since $\sigma \sim \ell^{-2}$ (where ℓ is the distance of separation between the adjacent grafted PE chains), the above relation will also allow us to identify the de-coupled regime in terms of the critical distance of separation. Please note that in this entire derivation of identifying σ_c , we have not accounted for ΔF_{EDL} . The reason is straightforward. It is the PE charge (and the PE electrostatic effects)

that triggers this EDL formation and the subsequent free energy change. Therefore, ΔF_{EDL} should scale as $\Delta F_{PEB,elec}$. Hence it suffices to represent the scaling of the entire electrostatic effects (i.e., the combination of the PE electrostatic effect and the EDL effects) by considering only $\Delta F_{PEB,elec}$.

For the case where there is no constraint on the height of the PE brush (e.g., PE brush grafted to an interface in an unbounded electrolyte solution), eq.(2.2) and eq.(2.11) suffice to pinpoint the conditions on the grafting density that must be obeyed to simultaneously ensure the formation of a brush-like structure as well as the attainment of decoupled (or coupled) regimes. However, in the present case we are studying the PE-grafted nanochannels. Therefore, there needs to be an additional constraint that the PE brush height (d) should not exceed the channel half height (h). The condition $d > h$ will lead to a number of new physical phenomena (such as interdigitation and compression of PE brushes from the two nanochannel walls), which is beyond the scope of the present analysis. In order to ensure $d < h$, we must have [using $\omega = \frac{1-2\chi}{2}a_k^3$ and assuming that we are in de-coupled regime, i.e., the PE brush thickness d is dictated by eq.(2.4)]:

$$N_p \left(\frac{1-2\chi}{6} \sigma a_k^5 \right)^{1/3} < h \quad (2.12)$$

The corresponding critical σ (denoted as σ_h), should therefore be:

$$\sigma_h \sim \frac{h^3}{N_p^3 a_k^5}. \quad (2.13)$$

By definition, σ_h denotes that critical grafting density that decides whether or not the PE layer thickness exceeds the nanochannel half height. In case $\sigma < \sigma_h$, the PE layer thickness is smaller than the nanochannel half height; on the other hand if $\sigma > \sigma_h$,

the PE thickness is greater than the nanochannel half height. Hence, within the scope of the present study, we must always have

$$\sigma < \sigma_h. \tag{2.14}$$

From the above analysis, we may infer that three conditions [eqs.(2.2,2.11,2.14)] simultaneously dictate the eventual choice of σ and the physical regime (brush or not, de-coupled or not, interpenetrated or not) in which the operation of the PE-grafted nanochannels can be categorized.

2.3 Applications of the scaling laws

To illustrate the applicability of these scaling predictions and the manner in which these predictions allow us to choose our system parameters, we consider two actual examples of PE-grafted nanochannels. In the first example, we consider the PE to be polyacrylic acid (PAA), whereas in the second example, we consider the PE to be λ -DNA. The results are illustrated in Figs. 2.1(a,b). These figures serve as the phase space for selecting the appropriate combination of N_p and σ values that will simultaneously ensure that the grafted PE molecules attain brush-like configuration and at the same time have a thickness d that is smaller than the nanochannel half height h . For example, brush-like configuration is not satisfied for any $\sigma - N_p$ combination below the line representing the variation of σ^* with N_p ; similarly, the brush formed will have a height larger than h for any $\sigma - N_p$ combination above the

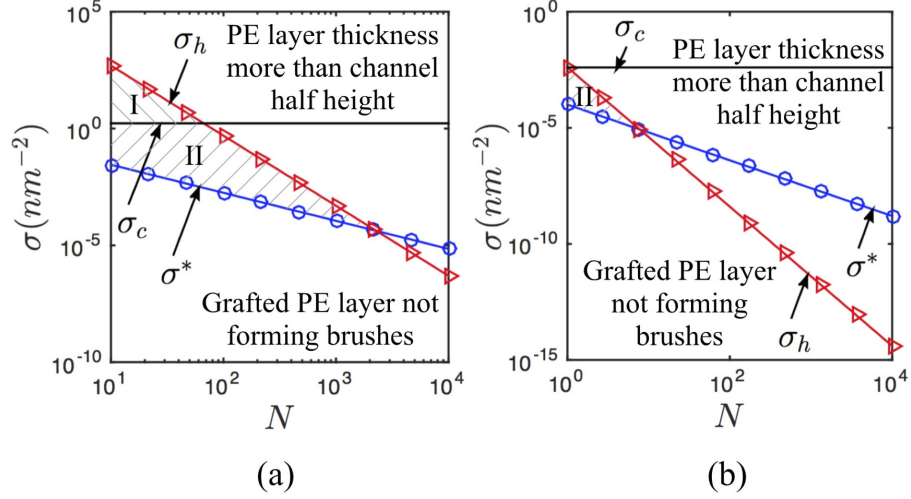


Figure 2.1: Variation of σ^* , σ_h , and σ_c with N_p for (a) grafted PAA chains and (b) grafted λ -DNA chains. The hashed zones in both the plots represent the $\sigma - N_p$ phase space that simultaneously ensure $d < h$ and that the grafted PEs form brush-like configurations. Also these hashed zones are divided into zone I (where $\sigma > \sigma_c$, and hence $\Delta F_{PEB,elec} < \Delta F_{PEB,ent}$) and zone II (where $\sigma < \sigma_c$, and hence $\Delta F_{PEB,elec} > \Delta F_{PEB,ent}$). In these simulations, we use $a_k = 1.5 \text{ nm}$ and $t = 0.4 \text{ nm}$ for PAA chains, whereas $a_k = 100 \text{ nm}$ and $t = 2.5 \text{ nm}$ for DNA chains. Also σ_h is computed for the both the cases considering $h = 100 \text{ nm}$. This figure is taken from Chen and Das [8].

line representing the variation of σ_h with N_p . Therefore, both these conditions (i.e., grafted PEs attain brush-like configuration and $d < h$) are simultaneously satisfied only by that $\sigma - N_p$ combination that lies within the hashed zones in both Figs. 2.1(a) and 2.1(b). Of course, the hashed zone that is below the line representing the variation of σ_c with N_p (please note that σ_c does not depend on N_p and hence is a line parallel to N axis) is the zone where $\Delta F_{PEB,elec} > \Delta F_{PEB,ent}$ (zone II), whereas the zone above this σ_c is zone I where $\Delta F_{PEB,elec} < \Delta F_{PEB,ent}$. We find that while both these zones exist for PAA, for DNA only zone II exists. In order to ensure that one works in the de-coupled regime, one needs to choose a $\sigma - N_p$ combination that

lies deep into any of these two zones well away from the σ_c line. Comparing Figs. 2.1(a,b), we can infer that the two conditions (formation of brush and $d < h$) are met only for a narrow window of values of σ and N_p (in fact for very small N_p) for the DNA chains, whereas for the PAA chains it is satisfied over a much broader ranges of these parameters.

2.4 Conclusions

In this chapter, we derive scaling laws for nanoconfined PE brushes in order to pinpoint the phase space of the system parameters that ensure that (a) the grafted PE layer forms brushes, (b) the brush height is smaller than the nanochannel half height, and (c) the electrostatics of the PE brushes and the resultant EDL can be decoupled from the PE entropic and excluded volume effects. Such phase space forms the basis of selection of parameters throughout the thesis. More importantly, they will be useful for designing of PE-grafted nanochannels and for pinpointing the dominant effects that govern the functioning of these nanochannels.

Chapter 3: Electrostatics of nanoconfined pH and pOH responsive polyelectrolyte brushes in the decoupled regime

In this chapter¹, a free energy based formalism is proposed to study the electrostatics of the nanoconfined pH or pOH responsive polyelectrolyte (PE) brushes in the decoupled regime. This responsiveness is manifested through the H^+ -ion or OH^- -ion concentration-dependent charging of the PE. The proposed model accounts for the appropriate consideration of the H^+ and OH^- ion concentration – evoked through the employment of appropriate free energy procedure to yield these concentrations – in the description of the electrostatics of the PE brushes. It is pinpointed how this lack of appropriate consideration of the H^+ and OH^- ion concentrations leads to unphysical description of these ion concentration profiles for the system with nanoconfined pH or pOH responsive PE brushes. Finally the proposed model rectifies this unphysical condition by proposing a non-unique cubic distribution of the chargeable sites of the PE brushes.

¹Contents of this chapter have been published as: *G. Chen and S. Das, Electrostatics of soft charged interfaces with pH-dependent charge density: effect of consideration of appropriate hydrogen ion concentration distribution. RSC Adv., Vol. 5, pp. 4493–4501 (2015).*

3.1 Introduction

pH or pOH responsive PE brushes are characterized by its chargeable sites that undergo an acid-like or a base-like dissociation reaction [53, 54]. This dissociation reaction, which depends on the local H^+ or OH^- ion concentrations, decides the charging of the PE brushes, thereby ensuring a pH or pOH dependent charging of the PE brushes. This particular model of PE brushes has received considerable theoretical attention, given the extensive use of pH-responsive PE brushes in a large number of applications [54, 55]. The challenge with all of these models is that they focus only on modelling the equilibrium of the PE brushes using simply the Boltzmann distribution to describe the distribution of electrolyte and H^+ and OH^- ions [46, 52, 53]. This Boltzmann distribution represents the minimized free energy equation for a given type of ion only when this equilibrium for this type of ion is dictated solely by the balance of the electrostatic and the entropic energies of the ion. For negatively charged PE brushes (i.e., where the PE brushes get charged by an acid-like ionization), the energy associated with the H^+ ion within the PE brush layer, in addition to the electrostatic and entropic energies, will also consist of the energy associated with the H^+ -ion-concentration-dependent ionization of the PE brushes. Exactly same contribution becomes relevant in the description of the OH^- ion within the PE layer for positively charged PE brushes getting charged due to a base-like ionization and demonstrating OH^- -ion-concentration-dependent charging. Therefore, for these cases it is completely inaccurate to describe these ion concentrations simply by the Boltzmann distribution – the appropriate description must account for this additional

contribution associated with the ionization of the PE brushes, as has been done in this present chapter.

In this chapter, we first develop a free energy formalism in the decoupled regime that in addition to describing the equilibrium electrostatics of the PE brushes as well as the equilibrium distributions of the electrolyte ions, describes the equilibrium of the H^+ (OH^-) ion concentrations for negatively (positively) charged PE brushes by accounting for the contributions of the ionization reactions that charges the PE brushes. This yields completely new expressions for the concentration distribution of the H^+ (OH^-) ions, as compared to those expressed by the Boltzmann distributions. More importantly, these H^+ (OH^-) ion distributions will dictate the charging of the PE brush as well as the electrostatics of the EDL induced by this PE brush layer – consequently, this appropriate description, not only ensures a physically realistic description of the PE brush layer, but also ascertains a correct analysis of the PE layer electrostatics. One major reason why such a flaw in the modelling has so far been overlooked is that typically one has considered much smaller values of H^+ ion concentration as compared to the electrolyte ion concentration; therefore, this possible effect of appropriate H^+ ion concentration description in the overall EDL electrostatics has not been significant enough to warrant a closer look into the problem.

The central result of our analysis is that this appropriate quantification of the H^+ (or OH^-) ion concentration is possible only when there is a non-uniform distribution of the polyelectrolyte chargeable sites (PCS) along the height of the PE brush layer. We show that such a non-uniformity is necessary to ensure continuities in the value and in the gradient of the H^+ (or OH^-) ion concentrations at the

PE-layer-electrolyte interface. It will be demonstrated that this extremely important issue has hitherto remained completely unidentified stemming from the sheer disregard of the explicit H^+ (or OH^-) ion concentration distribution in the modelling of the electrostatics of the pH (or pOH) responsive PE brushes. The second important issue on which this chapter will shed light is the nature of this non-uniformity in the PCS distribution. We establish that this PCS distribution must obey at least a cubic profile, arising from the fact that the four different conditions must be satisfied by the PCS distribution – this is true for both pH and pOH responsive PE brushes. These conditions are the continuities in the value and in the gradient of H^+ (or OH^-) concentration distribution at the PE-layer-electrolyte interface, zero net flux of H^+ (or OH^-) concentration at the PE-layer-rigid-solid interface and constancy in the total number of PCS. We end this chapter with a discussion on examples of different experiments of pH-dependent shape changes of polyelectrolyte brushes [65,66], where our proposed theory can provide useful insights and interpretations.

3.2 Theory

In this chapter, we are interested to obtain the electrostatics in a pH or a pOH responsive PE-brush-grafted nanochannel in the *decoupled regime*. It has already been discussed in Chapter 2 that such a regime is characterized by the fact that the PE layer thickness d is independent of the electrostatic effects of the PE and the induced EDL. Attainment of this decoupled regime is ensured as we consider a $\sigma - N_p$ combination of the grafted PE molecules that is in the hashed zone and also substantially

distanced from the $\sigma = \sigma_c$ line (see Fig. 2.1 in chapter 2). A logical choice can be PAA molecules with $N_p = 100$ and $\sigma = 10^{-2} \text{ nm}^{-2}$. This ensures that the parameters belong to the hashed zone *II* [see Fig. 2.1(a) in chapter 2], substantially distanced from $\sigma = \sigma_c$ line. For such a choice, $\sigma \ll \sigma_c$ and hence $\Delta F_{PEB,elec} \gg \Delta F_{PEB,ent}$. Please note that the analysis that follows is always valid for a nanochannel grafted with a PE brush layer with $\sigma \ll \sigma_c$ (i.e., $\Delta F_{PEB,elec} \gg \Delta F_{PEB,ent}$). Of course, almost identical analysis of the nanoconfined PE layer electrostatics is valid for the other zone (zone *I*, where $\sigma \gg \sigma_c$ and hence $\Delta F_{PEB,elec} \ll \Delta F_{PEB,ent}$); the only difference is that for this case the contribution of $\Delta F_{PEB,elec}$ in the overall ΔF_{PEB} is negligible. Of course, the brushes being PAA they are pH-responsive, i.e., they demonstrate pH-dependent negative charging. Below we provide an analysis that is valid for both negatively charged (or pH-responsive) as well as positively charged (or pOH-responsive) nanoconfined PE brushes [see Fig. (3.1)].

For the case where we are in zone *II*, we may write:

$$\Delta F \approx \Delta F_{PEB,elec} + \Delta F_{EDL} = \int f(\psi, \psi', n_{\pm}, n_{H^+}, n_{OH^-}) d^3\mathbf{r}. \quad (3.1)$$

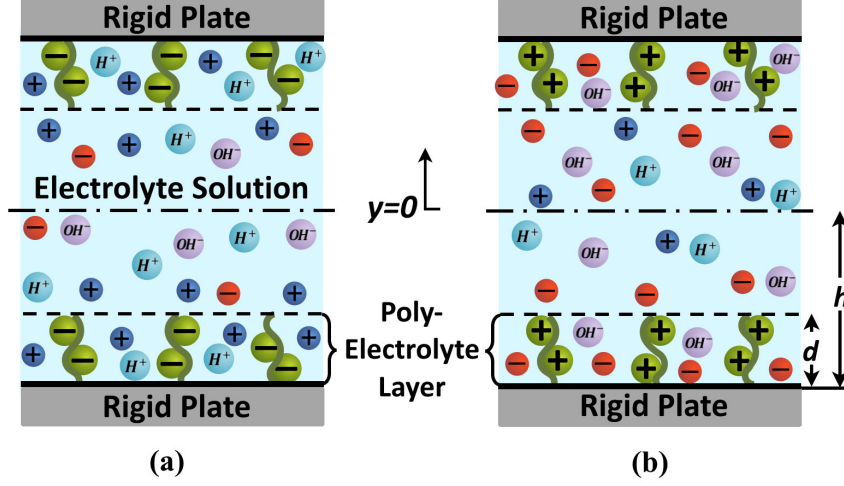


Figure 3.1: Schematic of the nanochannel grafted with (a) negatively charged PE layer and (b) positively charged PE layer.

Here f is the density of the EDL free energy change, expressed as:

$$\begin{aligned}
 f &= k_B T \sum_i \left[n_i \left(\ln \left(\frac{n_i}{n_{i,\infty}} \right) - 1 \right) \right] - \frac{\epsilon_0 \epsilon_r}{2} |\nabla \psi|^2 + e\psi \left[\sum_i z_i n_i - \varphi n_{A^-} \right] \\
 &\quad \text{[for } -h \leq y \leq -h + d, \text{ (negative PE layer)}], \\
 f &= k_B T \sum_i \left[n_i \left(\ln \left(\frac{n_i}{n_{i,\infty}} \right) - 1 \right) \right] - \frac{\epsilon_0 \epsilon_r}{2} |\nabla \psi|^2 + e\psi \left[\sum_i z_i n_i + \varphi n_{BH^+} \right] \\
 &\quad \text{[for } -h \leq y \leq -h + d, \text{ (positive PE layer)}], \\
 f &= k_B T \sum_i \left[n_i \left(\ln \left(\frac{n_i}{n_{i,\infty}} \right) - 1 \right) \right] - \frac{\epsilon_0 \epsilon_r}{2} |\nabla \psi|^2 + e\psi \left[\sum_i z_i n_i \right] \\
 &\quad \text{[for } -h + d \leq y \leq 0]. \tag{3.2}
 \end{aligned}$$

In the first two equations of eq.(3.2), which represent the free energy densities within the negatively (positively) charged PE brush layer, in the right hand side the first term represents the entropic contribution of the ions, the second term represents the self electrostatic energy of the EDL electric field, and the final term represents

the electrostatic energy of the electrolyte, hydrogen, hydroxyl, and the PE ions. In the third equation of eq.(3.2), which represents the free energy density outside the PE brush layer for both negatively and positively charged brushes, all these three terms on the right hand side remain identical with the exception of the electrostatic contribution that no longer consists of the contribution due to the PE ions. Further, ψ is the electrostatic potential, ϵ_0 is the permittivity of free space, ϵ_r is the relative permittivity of the medium, e is the electronic charge, n_i and $n_{i,\infty}$ are the number density and the bulk number density of ionic species i ($i = \pm, H^+, OH^-$). Here the electrolyte salt is assumed to be monovalent and symmetric ($z_+ = -z_- = 1$) and z_i is the valence of the ionic species i ($i = \pm, H^+, OH^-$). Also in eq.(3.2), n_{A^-} and n_{BH^+} are the number densities of the positive and negative PE ions. $\varphi(y)$ is the distribution of the polyelectrolyte chargeable sites (PCS) within the PE brush layer. $\varphi(y)$ is considered to be a *non-unique* cubic function in y ; this ensures avoiding unphysical discontinuities associated with considering a constant φ for a PE layer with $pH(pOH)$ -dependent charge density. Details regarding this choice of $\varphi(y)$ is discussed later in the chapter. The number densities of the PE ions depend on local H^+ (or OH^-) ion concentration values for negative (positive) PE layer and can be expressed as:

$$n_{A^-} = \frac{K'_a \gamma_a}{K'_a + n_{H^+}}, \quad n_{BH^+} = \frac{K'_b \gamma_b}{K'_b + n_{OH^-}}. \quad (3.3)$$

Here the anionic charge of the negatively charged PE layer is attributed to the ionization of the acid HA ($HA \leftrightarrow H^+ + A^-$; ionization constant K_a), whereas the cationic charge of the positively charged PE layer is attributed to the ionization of

base B ($B + H_2O \leftrightarrow BH^+ + OH^-$; ionization constant K_b). Also in eq.(3.3), γ_a and γ_b are the maximum site densities of anionic (for the negatively charged PE layer) and the cationic (for the positively charged PE layer) groups, and $K'_a = 10^3 N_A K_a$, $K'_b = 10^3 N_A K_b$ (N_A is the Avogadro number). Please note that eq.(3.2) is based on the assumption that the EDL can be described by the mean-field electrostatics. Therefore, issues such as ion-ion correlations have not been considered. In fact, effects such as consideration of finite ion sizes and finite solvent polarizability – these non-Poisson-Boltzmann effects can be modelled within the mean-field framework – have also been neglected.

In order to obtain the equilibrium distribution of the electrostatic potential and the ionic distribution for the present case [described by eqs.(3.2,3.3)], we minimize eq.(3.2) with respect to ψ , n_{\pm} , n_{H^+} , and n_{OH^-} . This minimization yields coupled ordinary differential equations for ψ and n_{H^+} (or n_{OH^-}) for negative (or positive) PE layer, which are solved numerically to obtain the equilibrium profiles of ψ , n_{H^+} (or n_{OH^-}), and φn_{A^-} (or φn_{BH^+}). Here we briefly summarize these minimization steps for both negatively (pH-responsive) and positively (pOH-responsive) charged PE brush layer.

Negatively charged PE brush layer

The equilibrium electrostatic potential and the concentration distribution of different ions can be obtained by minimizing ΔF [see eqs.(3.1,3.2) for expression of ΔF] with respect to ψ , n_{\pm} , n_{H^+} , and n_{OH^-} .

Minimization of ΔF with respect to ψ yields:

$$\begin{aligned}\frac{\delta(\Delta F)}{\delta\psi} = 0 &\Rightarrow \frac{\partial f}{\partial\psi} - \frac{d}{dy} \left(\frac{\partial f}{\partial\psi'} \right) = 0 \\ \Rightarrow \frac{d^2\psi}{dy^2} &= \frac{e(n_- - n_+ + n_{OH^-} - n_{H^+} + \varphi n_{A^-})}{\epsilon_0\epsilon_r} \quad [\text{for } -h \leq y \leq -h+d], \\ \Rightarrow \frac{d^2\psi}{dy^2} &= \frac{e(n_- - n_+ + n_{OH^-} - n_{H^+})}{\epsilon_0\epsilon_r} \quad [\text{for } -h+d \leq y \leq 0].\end{aligned}\quad (3.4)$$

Minimization of ΔF with respect to n_{\pm} , n_{H^+} and n_{OH^-} , yields:

$$\frac{\delta(\Delta F)}{\delta n_{\pm}} = 0 \Rightarrow n_{\pm} = (n_{\pm,\infty}) \exp\left(\mp \frac{e\psi}{k_B T}\right) \quad [\text{for } y \geq -h], \quad (3.5)$$

$$\frac{\delta(\Delta F)}{\delta n_{OH^-}} = 0 \Rightarrow n_{OH^-} = (n_{OH^-,\infty}) \exp\left(\frac{e\psi}{k_B T}\right) \quad [\text{for } y \geq -h], \quad (3.6)$$

and

$$\begin{aligned}\frac{\delta(\Delta F)}{\delta n_{H^+}} = 0 &\Rightarrow n_{H^+} = (n_{H^+,\infty}) \exp\left[-\frac{e\psi}{k_B T} \left(1 + \varphi \frac{K'_a \gamma_a}{(K'_a + n_{H^+})^2}\right)\right] \\ &\quad [\text{for } -h \leq y \leq -h+d], \\ \frac{\delta(\Delta F)}{\delta n_{H^+}} = 0 &\Rightarrow n_{H^+} = (n_{H^+,\infty}) \exp\left(-\frac{e\psi}{k_B T}\right) \quad [\text{for } -h+d \leq y \leq 0].\end{aligned}\quad (3.7)$$

Here $n_{\pm,\infty}$ are the bulk number densities of the electrolyte ions (in units of $1/m^3$), $n_{H^+,\infty} = 10^{3-pH_{\infty}} N_A$ (pH_{∞} is the bulk pH) is the bulk number density of hydrogen ions, $n_{OH^-,\infty} = 10^{3-pOH_{\infty}} N_A$ (pOH_{∞} is the bulk pOH) is the bulk number density of the hydroxide ions and $pH_{\infty} + pOH_{\infty} = 14$. Here $n_{+,\infty} = n_{\infty}$ and $n_{-,\infty} = n_{\infty} + n_{H^+,\infty}$. Here n_{∞} is the bulk number density of the electrolyte ions contributed by the added electrolyte salt; n_{∞} is related to the bulk concentration c_{∞} (in M) as $n_{\infty} = 10^3 N_A c_{\infty}$. More importantly, here we assume that the added acid furnishes the same anion as the electrolyte salt. The bulk number densities are the number densities of the

ions in the microchannel reservoirs (where $\psi = 0$) connecting the nanochannel. *The most important contribution of this present chapter is this new governing equation for n_{H^+} [see the first equation of eq.(3.7)] – it can be clearly seen that we embark on an equation different from the Boltzmann distribution for describing n_{H^+} within the PE brush layer. This stems from the use of appropriate free energy minimization in order to arrive at the distribution of n_{H^+} – such an approach has been missing from all the existing continuum models of pH-responsive PE brushes that always (incorrectly) use the Boltzmann distribution to express the H^+ ion number density. It is is easy to see that such an incorrect expression of H^+ ion number density will affect the PE charging and the PE-induced EDL electrostatic potential [see eqs.(3.3,3.4)].*

ψ can be solved by first using eqs.(3.5,3.6,3.7) to replace the ion number densities appearing in eq.(3.4), and then solving the resultant differential equation in ψ in presence of the boundary conditions expressed below:

$$\begin{aligned} \left(\frac{d\psi}{dy}\right)_{y=0} &= 0, & (\psi)_{y=(-h+d)^+} &= (\psi)_{y=(-h+d)^-}, \\ \left(\frac{d\psi}{dy}\right)_{y=-h} &= 0, & \left(\frac{d\psi}{dy}\right)_{y=(-h+d)^+} &= \left(\frac{d\psi}{dy}\right)_{y=(-h+d)^-}. \end{aligned} \quad (3.8)$$

Critical thing to note here is that this differential equation in ψ [see eq.(3.9) for the corresponding dimensionless form] will also contain the unresolved expression for n_{H^+} ; this stems from the fact that while the expressions for the number densities of all other ions (i.e., n_{\pm} , n_{OH^-}) are explicit in ψ [see eqs.(3.5,3.6)], n_{H^+} is implicit in ψ [see eq.(3.7) and note that n_{H^+} also appears in the right hand side of the first equation of eq.(3.7)]. Therefore, we shall have a set of equations for ψ and n_{H^+} that needs to be solved simultaneously. These equations, in dimensionless forms, can be

expressed as:

$$\begin{aligned} \frac{d^2\bar{\psi}}{d\bar{y}^2} &= \frac{1}{2\bar{\lambda}^2} \left[(1 + \bar{n}_{H^+, \infty}) \exp(\bar{\psi}) - \exp(-\bar{\psi}) + \bar{n}_{OH^-, \infty} \exp(\bar{\psi}) - \bar{n}_{H^+} + \frac{\bar{K}'_a \bar{\gamma}_a \varphi(\bar{y})}{\bar{K}'_a + \bar{n}_{H^+}} \right] \\ &\quad [\text{for } -1 \leq \bar{y} \leq -1 + \bar{d}], \\ \frac{d^2\bar{\psi}}{d\bar{y}^2} &= \frac{1}{2\bar{\lambda}^2} \left[(1 + \bar{n}_{H^+, \infty}) \exp(\bar{\psi}) - \exp(-\bar{\psi}) + \bar{n}_{OH^-, \infty} \exp(\bar{\psi}) - \bar{n}_{H^+, \infty} \exp(-\bar{\psi}) \right] \\ &\quad [\text{for } -1 + \bar{d} \leq \bar{y} \leq 0]. \end{aligned} \quad (3.9)$$

$$\begin{aligned} \bar{\psi} &= -\frac{\ln\left(\frac{\bar{n}_{H^+}}{\bar{n}_{H^+, \infty}}\right)}{1 + \frac{\bar{K}'_a \bar{\gamma}_a \varphi(\bar{y})}{(\bar{K}'_a + \bar{n}_{H^+})^2}} \quad [\text{for } -1 \leq \bar{y} \leq -1 + \bar{d}], \\ \bar{\psi} &= -\ln\left(\frac{\bar{n}_{H^+}}{\bar{n}_{H^+, \infty}}\right) \quad [\text{for } -1 + \bar{d} \leq \bar{y} \leq 0]. \end{aligned} \quad (3.10)$$

The corresponding dimensionless boundary conditions become:

$$\begin{aligned} \left(\frac{d\bar{\psi}}{d\bar{y}}\right)_{\bar{y}=0} &= 0, & (\bar{\psi})_{\bar{y}=(-1+\bar{d})^+} &= (\bar{\psi})_{\bar{y}=(-1+\bar{d})^-}, \\ \left(\frac{d\bar{\psi}}{d\bar{y}}\right)_{\bar{y}=-1} &= 0, & \left(\frac{d\bar{\psi}}{d\bar{y}}\right)_{\bar{y}=(-1+\bar{d})^+} &= \left(\frac{d\bar{\psi}}{d\bar{y}}\right)_{\bar{y}=(-1+\bar{d})^-}. \end{aligned} \quad (3.11)$$

In the above equations, $\bar{y} = y/h$, $\bar{\lambda} = \lambda/h$ ($\lambda = \sqrt{\frac{\epsilon_0 \epsilon_r k_B T}{2n_\infty e^2}}$ is the EDL thickness), $\bar{d} = d/h$, $\bar{\psi} = e\psi/(k_B T)$, $\bar{n}_{H^+} = n_{H^+}/n_\infty$, $\bar{n}_{OH^-} = n_{OH^-}/n_\infty$, $\bar{n}_{H^+, \infty} = n_{H^+, \infty}/n_\infty$, $\bar{n}_{OH^-, \infty} = n_{OH^-, \infty}/n_\infty$, $\bar{K}'_a = K'_a/n_\infty$, and $\bar{\gamma}_a = \gamma_a/n_\infty$.

Positively charged PE brush layer

For positively charged PE layer, we have $n_{-, \infty} = n_\infty$ and $n_{+, \infty} = n_\infty + n_{OH^-, \infty}$.

This is under the assumption that the bulk number density of the electrolyte ions contributed by the added electrolyte salt is n_∞ , and the base added produces the

same cations as the added salt. For this case too, the same minimization procedure [i.e., minimizing ΔF with respect to ψ , n_{\pm} , n_{H^+} and n_{OH^-}] is employed. Here n_{OH^-} depends on ψ implicitly [see eq.(3.14) and note the fact that n_{OH^-} also appears in the right hand side of the first equation of eq.(3.14)], while the dependence of n_{\pm} and n_{H^+} on ψ is explicit. The resulting set of equations are:

$$\begin{aligned} \frac{\delta(\Delta F)}{\delta\psi} = 0 &\Rightarrow \frac{\partial f}{\partial\psi} - \frac{d}{dy} \left(\frac{\partial f}{\partial\psi'} \right) = 0 \\ \Rightarrow \frac{d^2\psi}{dy^2} &= \frac{e(n_- - n_+ + n_{OH^-} - n_{H^+} - \varphi n_{BH^+})}{\epsilon_0\epsilon_r} \quad [\text{for } -h \leq y \leq -h+d], \\ \Rightarrow \frac{d^2\psi}{dy^2} &= \frac{e(n_- - n_+ + n_{OH^-} - n_{H^+})}{\epsilon_0\epsilon_r} \quad [\text{for } -h+d \leq y \leq 0]. \end{aligned} \quad (3.12)$$

$$\frac{\delta(\Delta F)}{\delta n_{H^+}} = 0 \Rightarrow n_{H^+} = (n_{H^+,\infty}) \exp\left(-\frac{e\psi}{k_B T}\right) \quad [\text{for } y \geq -h], \quad (3.13)$$

$$\begin{aligned} \frac{\delta(\Delta F)}{\delta n_{OH^-}} = 0 &\Rightarrow n_{OH^-} = (n_{OH^-,\infty}) \exp\left[\frac{e\psi}{k_B T} \left(1 + \varphi \frac{K'_b \gamma_b}{(K'_b + n_{OH^-})^2}\right)\right] \\ & \quad [\text{for } -h \leq y \leq -h+d], \\ \frac{\delta(\Delta F)}{\delta n_{OH^-}} = 0 &\Rightarrow n_{OH^-} = (n_{OH^-,\infty}) \exp\left(\frac{e\psi}{k_B T}\right) \quad [\text{for } -h+d \leq y \leq 0]. \end{aligned} \quad (3.14)$$

Here too we find that the OH^- ion number density is no longer expressed by Boltzmann distribution; rather similar to the case of negatively charged PE layer, we derive a new set of equations, commensurate with the appropriate free energy based picture, for describing the distribution of the OH^- ions.

Finally, the electrolyte ion concentrations are governed by eq.(3.5). Consequently, the resulting set of coupled governing equations will be in ψ and n_{OH^-} . They are

expressed in dimensionless form as:

$$\begin{aligned}\frac{d^2\bar{\psi}}{d\bar{y}^2} &= \frac{1}{2\bar{\lambda}^2} \left[\exp(\bar{\psi}) - (1 + \bar{n}_{OH^-,\infty}) \exp(-\bar{\psi}) - \bar{n}_{H^+,\infty} \exp(-\bar{\psi}) + \bar{n}_{OH^-} - \frac{\bar{K}'_b \bar{\gamma}_b \varphi(\bar{y})}{\bar{K}'_b + \bar{n}_{OH^-}} \right] \\ &\quad [\text{for } -1 \leq \bar{y} \leq -1 + \bar{d}], \\ \frac{d^2\bar{\psi}}{d\bar{y}^2} &= \frac{1}{2\bar{\lambda}^2} \left[\exp(\bar{\psi}) - (1 + \bar{n}_{OH^-,\infty}) \exp(-\bar{\psi}) - \bar{n}_{H^+,\infty} \exp(-\bar{\psi}) + \bar{n}_{OH^-,\infty} \exp(\bar{\psi}) \right] \\ &\quad [\text{for } -1 + \bar{d} \leq \bar{y} \leq 0].\end{aligned}\quad (3.15)$$

$$\begin{aligned}\bar{\psi} &= \frac{\ln\left(\frac{\bar{n}_{OH^-}}{\bar{n}_{OH^-,\infty}}\right)}{1 + \frac{\bar{K}'_b \bar{\gamma}_b \varphi(\bar{y})}{(\bar{K}'_b + \bar{n}_{OH^-})^2}} \quad [\text{for } -1 \leq \bar{y} \leq -1 + \bar{d}], \\ \bar{\psi} &= \ln\left(\frac{\bar{n}_{OH^-}}{\bar{n}_{OH^-,\infty}}\right) \quad [\text{for } -1 + \bar{d} \leq \bar{y} \leq 0].\end{aligned}\quad (3.16)$$

In the above equations, $\bar{\gamma}_b = \gamma_b/n_\infty$ and $\bar{K}'_b = K'_b/n_\infty$.

Solutions of the electrostatics of the negatively-charged PE brush layer is obtained by numerically solving eq.(3.9) and eq.(3.10) in presence of the boundary conditions expressed in eq.(3.11). Similarly, the electrostatics of the positively-charged PE brush layer is obtained by numerically solving eq.(3.15) and eq.(3.16) in presence of the boundary conditions expressed in eq.(3.11). Of course, for the solution of both the cases we need to know the distribution of PCS $\varphi(y)$. Its distribution and its effect on the PE brush electrostatics is discussed in details below.

3.3 Results

Here we provide results only for the case of negatively charged or pH-responsive nanoconfined PE brushes. But these results, qualitatively, are equally valid for the

positively charged brushes, with \bar{n}_{OH^-} replacing n_{H^+} and positive electrostatic potential replacing the negative electrostatic potential.

3.3.1 Electrostatic potential and hydrogen ion concentration profiles for uniform distribution of PCS within the PE brush layer

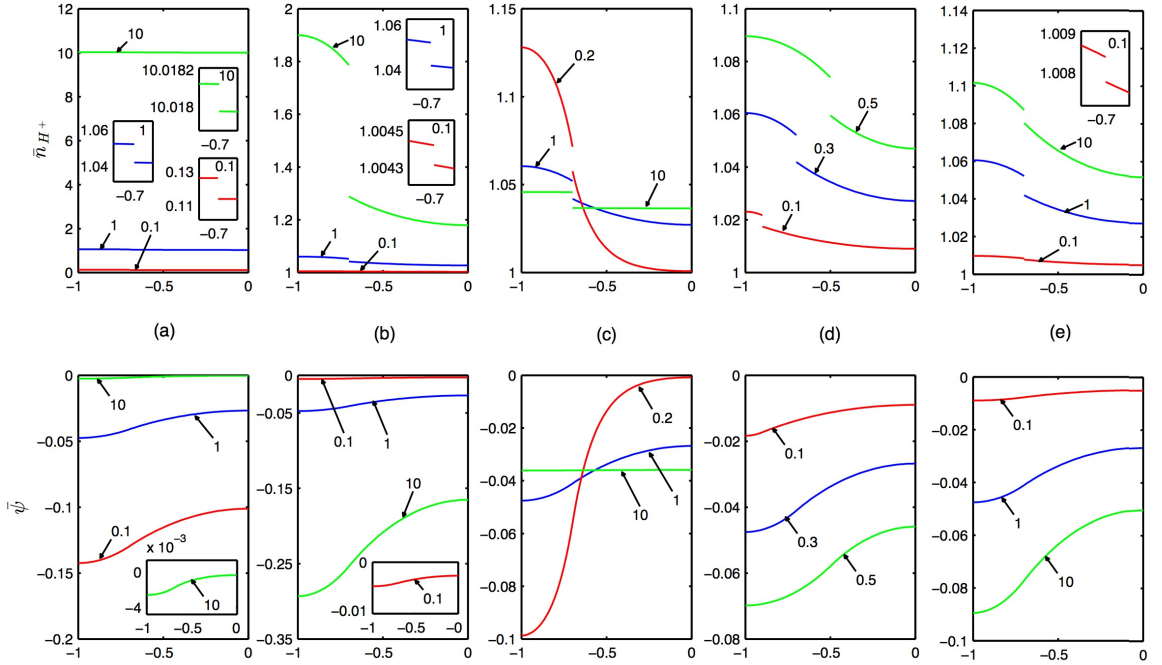


Figure 3.2: Variation of the dimensionless hydrogen ion number density (top panel) and the dimensionless electrostatic potential profile (bottom panel) for the case of uniform distribution of PCS. For all the figures we maintain the four parameters (i.e., $\bar{n}_{H^+, \infty}$, $\bar{\gamma}$, $\bar{\lambda}$, and \bar{K}'_a) as equal to unity and $\bar{d} = 0.3$ except for (a) $\bar{n}_{H^+, \infty} = 0.1, 1, 10$ (b) $\bar{\gamma} = 0.1, 1, 10$ (c) $\bar{\lambda} = 0.2, 1, 10$ (d) $\bar{d} = 0.1, 0.3, 0.5$ and (e) $\bar{K}'_a = 0.1, 1, 10$. In all the figures, the value of the parameter (which is being varied) is indicated. This figure is taken from Chen and Das [56].

The first set of results are obtained for $\varphi = 1$, i.e., we consider that the chargeable sites are distributed uniformly on the PE chains. The most important result,

evident in all the plots of Figure 3.2, is the distinct discontinuity in the profile at the location of the PE-layer-electrolyte interface ($\bar{y} = -1 + \bar{d}$). Identification of this discontinuity is the most significant finding of this chapter. Till date there have been many studies that have considered a pH-dependent charge density of a soft charged interface [46, 52, 53]; however in none of the studies this discontinuity has been identified, since none of the studies cared to consider the explicit hydrogen ion concentration distribution. In other words, these studies simply consider a Boltzmann distribution for the hydrogen ion concentration [i.e., the form expressed in the second part of eq.(3.10)] both inside and outside the PE layer. However, as we demonstrate through an appropriate free energy picture, the dependence of the PE layer reaction on the hydrogen ion concentration ensures that the hydrogen ion concentration no longer obeys a Boltzmann distribution inside the PE layer. Therefore, we encounter two different $\bar{n}_{H^+} - \bar{\psi}$ relationships – one inside the PE layer and one outside the PE layer [two parts shown in eq.(3.10)]. It is precisely for this reason that we encounter two different $\bar{n}_{H^+} - \bar{\psi}$ relationships at the brush-electrolyte interface (located at $\bar{y} = -1 + \bar{d}$), depending on whether we approach the interface from the PE layer side or the electrolyte side. Such a difference ensures that there are discontinuities in the value and in the gradient of $\bar{\psi}$ at $\bar{y} = -1 + \bar{d}$.

Here we discuss the effect of the individual parameters in dictating the profiles of \bar{n}_{H^+} and $\bar{\psi}$, as well as the discontinuity in the \bar{n}_{H^+} profile. Fig. 3.2(a) shows the effect of variation of the dimensionless bulk hydrogen ion concentration $\bar{n}_{H^+, \infty}$. Insets of Fig. 3.2(a) clearly reveals that the extent of discontinuity in \bar{n}_{H^+} values across the two sides of $\bar{y} = -1 + \bar{d}$ increases with a decrease in the value of $\bar{n}_{H^+, \infty}$.

Such a behavior can be attributed to the corresponding variation of $\bar{\psi}$. Lowering of $\bar{n}_{H^+, \infty}$ will enhance the reaction ($\text{HA} \leftrightarrow \text{H}^+ + \text{A}^-$) that produces the polyelectrolyte ions A^- , thereby augmenting the number density of the A^- ions. This happens since the lowering of the hydrogen ion concentration signals a depletion of the hydrogen ions from the system, thereby favoring the forward reaction that produces H^+ ions (of course, along with the A^- ions). Enhanced number density of A^- ensures an enhanced magnitude of $\bar{\psi}$ for smaller values of \bar{n}_{H^+} , which in turn enhances the consequence of the disparity in the $\bar{n}_{H^+} - \bar{\psi}$ relationship leading to a more enhanced discontinuity in the \bar{n}_{H^+} profile. Fig. 3.2(b) demonstrates the effect of variation of the parameter $\bar{\gamma}$. Enhanced $\bar{\gamma}$ implies enhanced value of the PCS (that dissociate to produce the polyelectrolyte ions A^-) thereby enhancing the number density of A^- ions. This in turn augments the magnitude of $\bar{\psi}$ and the extent of discontinuity in the value of \bar{n}_{H^+} (for reasons discussed above) at $\bar{y} = 1 + \bar{d}$. Fig. 3.2(c) represents the effect of variation of the parameter $\bar{\lambda}$. Enhanced $\bar{\lambda}$ signifies larger extent of the EDL overlap in the nanochannel, leading to a much weaker gradient in the value of \bar{n}_{H^+} and $\bar{\psi}$ values – as a consequence it is the gradient of \bar{n}_{H^+} that shows a large discontinuity for weaker $\bar{\lambda}$ at $\bar{y} = -1 + \bar{d}$. However, since there is relatively less deviation in the value of $\bar{\psi}$ for different $\bar{\lambda}$ at $\bar{y} = -1 + \bar{d}$, the discontinuity in the value of \bar{n}_{H^+} (at $\bar{y} = -1 + \bar{d}$) is similar for different $\bar{\lambda}$ values. Fig. 3.2(d) reveals the effect of variation of the parameter \bar{d} . Enhanced \bar{d} increases the magnitude of $\bar{\psi}$ [35] (since there is greater total number of A^- ions), which in turn increases the extent of jump in \bar{n}_{H^+} profile at $\bar{y} = -1 + \bar{d}$. Variation of \bar{K}'_a [the corresponding effect on \bar{n}_{H^+} and $\bar{\psi}$ profiles is shown in Fig. 3.2(e)] produces the most non-trivial and non-monotonic variation of the

\bar{n}_{H^+} profile. Increase in \bar{K}'_a obviously enhances the reaction that produces A^- ions, thereby leading to an enhanced magnitude of $\bar{\psi}$ and a greater extent of discontinuity in the \bar{n}_{H^+} profile (for reasons discussed above). This description remains perfectly valid for the increase of \bar{K}'_a from 0.1 to 1. However, when \bar{K}'_a becomes very large ($= 10$), it effectively indicates a nearly complete dissociation of the chargeable groups (that produce the polyelectrolyte ions A^-). Hence for such a case the number density of the PE ions become effectively pH independent, thereby favoring the fact that \bar{n}_{H^+} profile will now be dictated by Boltzmann distribution both inside and outside the PE brush layer. Accordingly, there is much weaker discontinuity in the \bar{n}_{H^+} profile for $\bar{K}'_a = 10$, although the magnitude of $\bar{\psi}$ keeps on increasing.

3.3.2 Electrostatic potential and hydrogen ion concentration profiles for non-uniform distribution of PCS within the PE brush layer

We have identified that the appropriate consideration of hydrogen ion concentration distribution forbids simultaneous continuities in the gradient and in the value of both the electrostatic potential and the hydrogen ion concentration at the PE-layer-electrolyte interface. We have further identified that such discontinuities result from the contribution of the electrostatic effect of the PE layer ions; this effect introduces a situation where the relationship between $\bar{\psi}$ and \bar{n}_{H^+} are different at the PE-layer-electrolyte interface [see eq.(3.10)], depending on whether the interface is approached from the PE layer side or from the electrolyte side. This can be addressed only if it is ensured that the electrostatic contribution of the PE layer ions is such that

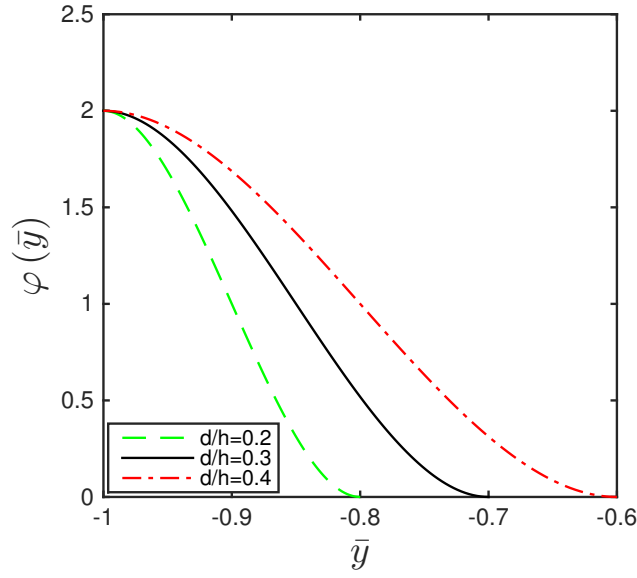


Figure 3.3: Profiles of the cubically varying PCS distribution for various dimensionless PE layer thickness \bar{d} . In the inset we schematically differentiate between (a) the case of uniform PCS distribution and (b) the case of cubic PCS distribution. This figure is taken from Chen and Das [5].

there are simultaneous continuities in the values and in the gradient of $\bar{\psi}$ and n_{H^+} at the PE-layer-electrolyte interface. Additionally, the net flux of the hydrogen ions must be zero at the PE-layer-rigid-wall interface. In a framework that does account for all the necessary contributions to the free energy [see eqs.(3.2)], these issues can only be addressed, by considering a dimensionless concentration (or volume fraction) distribution $\varphi(\bar{y})$ of the chargeable sites. Also, $\varphi(\bar{y})$ must satisfy the constraint:

$$\frac{1}{\sigma a_k^3} \int_{-h}^{-h+d} \varphi dy = N_{cs}, \quad (3.17)$$

where σ is the grafting density (having units of $1/m^2$), a_k is the Kuhn length (hence the volume of a monomer segment is $\sim a_k^3$), and N_{cs} is the number of chargeable sites for a PE molecule. In order to ensure the continuity of hydrogen ion concentrations at

the PE-electrolyte interface as well as satisfy the boundary condition at the PE-solid interface, φ can be any function that satisfies all the following three conditions, along with eq. (3.17):

$$\begin{aligned} \left[\varphi(\bar{y}) \right]_{\bar{y}=-1+\bar{d}} = 0 & \quad \left[\text{ensures } (\bar{n}_{H^+})_{\bar{y}=(-1+\bar{d})^-} = (\bar{n}_{H^+})_{\bar{y}=(-1+\bar{d})^+} \right], \\ \left[\frac{d\varphi(\bar{y})}{d\bar{y}} \right]_{\bar{y}=-1+\bar{d}} = 0 & \quad \left[\text{ensures } \left(\frac{d\bar{n}_{H^+}}{d\bar{y}} \right)_{\bar{y}=(-1+\bar{d})^-} = \left(\frac{d\bar{n}_{H^+}}{d\bar{y}} \right)_{\bar{y}=(-1+\bar{d})^+} \right] (3.18) \\ \left[\frac{d\varphi(\bar{y})}{d\bar{y}} \right]_{\bar{y}=-1} = 0 & \quad \left[\text{ensures } \left(\frac{d\bar{n}_{H^+}}{d\bar{y}} \right)_{\bar{y}=-1} = 0 \right], \end{aligned}$$

All these criteria are satisfied by a *non-unique* cubic distribution of φ expressed as:

$$\varphi(\bar{y}) = \left(\frac{N_{cs}a_k^3\sigma}{d} \right) \left(\frac{4}{d^3} \right) (\bar{y} + 1 - \bar{d})^2 \left(\bar{y} + 1 + \frac{\bar{d}}{2} \right) = \beta (\bar{y} + 1 - \bar{d})^2 \left(\bar{y} + 1 + \frac{\bar{d}}{2} \right), \quad (3.19)$$

where $\beta = \frac{4N_{cs}a_k^3h^3\sigma}{d^4}$.

Fig. 3.3 shows this profile for φ . Under these conditions, the explicit equilibrium electrostatic potential and hydrogen ion concentration distribution can be obtained by numerically solving the coupled equations [eqs.(3.9,3.10)] in presence of the boundary condition expressed in (3.11). Figures 3.4(a-f) show the variation of $\bar{\psi}$ and n_{H^+} profiles for the parameters $\bar{n}_{H^+, \infty}$, $\bar{n}_{OH^-, \infty}$, $\bar{\lambda}$, \bar{d} , \bar{K}'_a , $\bar{\gamma}$, and β . The most important observation that should be made from these figures is that for all the parameter values, there is no longer any discontinuity in the \bar{n}_{H^+} profile. Therefore, using the prescribed remedy of considering a non-uniform distribution of the PCS within the PE layer, we do ensure the removal of the utterly non-physical result of discontinuous hydrogen ion profiles. Figure 3.4(a) demonstrates the effect of considering different values of β . Enhanced β implies enhanced grafting density of the polyelectrolytes

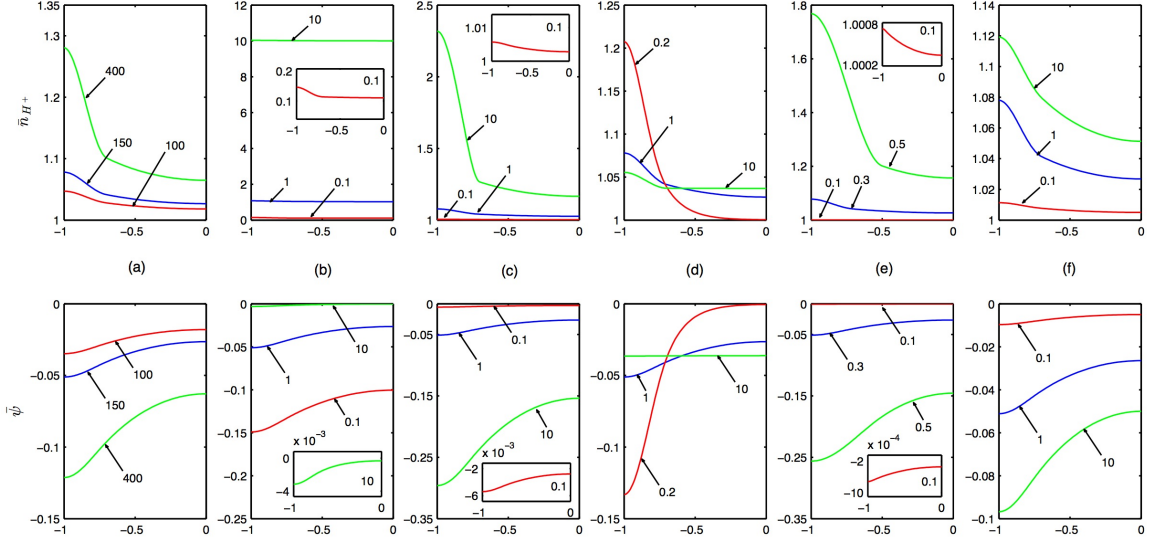


Figure 3.4: Variation of the dimensionless hydrogen ion number density (top panel) and the dimensionless electrostatic potential profile (bottom panel) for the case of uniform distribution of PCS. For all the figures we maintain the four parameters (i.e., $\bar{n}_{H^+, \infty}$, $\bar{\gamma}$, $\bar{\lambda}$, and \bar{K}'_a) as equal to unity, $\bar{d} = 0.3$, and $\beta = 150$ except for (a) $\beta = 100, 150, 400$, (b) $\bar{n}_{H^+, \infty} = 0.1, 1, 10$, (c) $\bar{\gamma} = 0.1, 1, 10$, (d) $\bar{\lambda} = 0.2, 1, 10$, (e) $\bar{d} = 0.1, 0.3, 0.5$, and (f) $K'_a = 0.1, 1, 10$. In all the figures, the value of the parameter (which is being varied) is indicated. This figure is taken from Chen and Das [56].

in the PE brush layer. This, in turn, signifies larger number density of the PE ions and hence larger magnitude of $\bar{\psi}$. There are two crucial issues associated with Figure 3.4(a). Firstly, we find that $\beta = 150$ represent a value that reproduces the $\bar{\psi}$ profile very similar to that of Figure 3.2(a). Therefore, for the subsequent plots [Figure 3.4(b-f)], we shall work with this value of β . More importantly, consideration of non-uniform distribution of chargeable sites in order to remove the non-physical behavior of the \bar{n}_{H^+} profiles (see Figure 3.2) leads to a much steeper \bar{n}_{H^+} profile within the PE layer. This behavior is true for the \bar{n}_{H^+} profiles for all other plots as well [see Figure 3.4(b-f)]. This steepness can be attributed to the fact that \bar{n}_{H^+} now spans larger

ranges of values over a given distance (which is the PE layer thickness) in order to remove the corresponding discontinuities (see Figure 3.2); hence larger the extent of discontinuity in Figure 3.2, steeper will be the corresponding \bar{n}_{H^+} profile within the PE layer. Figure 3.4(b) provides the effect of the variation of the parameter $\bar{n}_{H^+, \infty}$. Qualitatively the variation is very similar to that depicted in Figure 3.2(b), except for the fact that there is no discontinuity in \bar{n}_{H^+} profile here. Figure 3.4(c) represents the effect of the variation of $\bar{\gamma}$. For large $\bar{\gamma}$ ($=10$), the discontinuity in \bar{n}_{H^+} profile is very large [see Figure 3.2(b)]; therefore the \bar{n}_{H^+} profile is extremely steep within the PE layer. More importantly, we can actually find that \bar{n}_{H^+} value at the PE-layer-rigid-solid interface (i.e., at $\bar{y} = -1$) is slightly higher as compared to that in Fig. 3.2(b). This can be attributed to the corresponding cubic distribution of the PCS constituting the PE brush layer – this cubic distribution ensures greater fraction of PCS at $\bar{y} = -1$, which in turn causes greater \bar{n}_{H^+} concentration at $\bar{y} = -1$. Effect of this cubic profile in causing a more augmented value of \bar{n}_{H^+} at the PE-layer-rigid-solid interface is also reflected in Figure 3.4(d) that demonstrates the effect of the parameter $\bar{\lambda}$. From eq. (3.19) we get $[\varphi(y)/\beta]_{\bar{y}=-1} = \bar{d}^3/2$ – hence this enhancement of \bar{n}_{H^+} at the PE-layer-rigid-solid interface is most significant for larger values of \bar{d} ($=0.5$) [see Figure 3.4(e), which illustrates the effect of variation of parameter \bar{d}]. Finally, the non-monotonic behavior of the discontinuity for varying \bar{K}'_a [see Figure 3.2(e)], leads to a non-monotonic steepness variation of \bar{n}_{H^+} (within the PE layer) for the present case where a non-uniform distribution of chargeable sites within the PE layer is considered [see Figure 3.4(f) that demonstrates the effect of variation of the parameter \bar{K}'_a].

3.4 Discussions

Here we also attempt to highlight the relevance of the present calculations in qualitatively interpreting different experimental results on pH-responsive polyelectrolyte brushes. Yameen et al. [65] demonstrated that poly (4-vinyl pyridine) brushes undergo a pH-dependent reaction leading to a reversible switching between the swollen charged hydrophilic state (at low pH; here the polymer is pyridine) and collapsed, neutral hydrophobic state (at high pH; here the polymer is pyridinium). Here the charging occurs via a base-like reaction, when pyridinium, at a small pH, accepts a proton to form pyridine – this ensures that the charging of the PE layer is pH-dependent. Since this charging occurs at a small pH, the pH-dependent PE layer charge density will be typically witnessed at this small pH. Hence at such a pH, by the proposed analysis of this study, there needs to be a given non-uniform distribution of the PCS or monomers with the PCS concentration decaying away from the wall, and this ensures this swollen hydrophilic state. On the contrary, at large pH ($pH > pK_a$) the pyridine loses proton to become uncharged pyridinium. Therefore, at such pH the PE layer is uncharged, and therefore there is no constraint on the distribution of the monomers, enforcing them to remain in collapsed, neutral hydrophobic state.

Hou et al. [66] employed the pH-dependent shape modulation of poly acrylic acid (PAA) to develop a pH-gating ionic transport in a conical nanochannel. PAA contains a carboxylic acid group, which is assumed to form an intramolecular hydrogen bonding at low pH, whereas at high pH ionizes to form COO^- and in the process

is assumed to form hydrogen bonding with the surrounding water molecules. Hou et al. [66] hypothesized that such a transition from intramolecular to intermolecular hydrogen bonding enforced a structural transition of the PAA molecules, enforcing the conical nanochannel to allow water imbibition at the configuration where there is intermolecular hydrogen bonding (i.e., at larger pH). We can provide an alternate explanation, based on our proposed theory. At large pH, where the PAA molecules have ionized to form COO^- (i.e., the PE brush layer has pH-dependent charge density), the PCS will demonstrate a non-uniform distribution, with the PCS concentration decaying away from the wall. This will imply the monomer distribution will also obey a similar qualitative variation. Therefore, the drag is also much larger near the wall; since the flow velocity (which is a surface tension driven imbibition) is much weaker closer to the channel walls, this PE layer configuration (with greater PCS or monomer concentration at near-wall locations) ensures much weaker overall drag and hence a more enhanced flow rate. On the contrary, for smaller pH, the PE layer is uncharged, and hence the PCS or monomers can remain uniformly distributed, thereby inducing a much larger drag force and a weaker flow rate.

3.5 Conclusions

In this chapter, we have provided a rigorous free energy based approach to pinpoint a gross existing error in the modelling of electrostatics of an interface grafted with a pH (or pOH) responsive PE brush layer: we show that for such soft, charged interfaces, it is impossible to have a uniform PCS distribution within the PE layer.

We arrive at this very important conclusion on the basis of the fact that we consider for the first time explicit number density distribution of the H^+ (or OH^-) inside and outside the PE layer. We argue that the monomer distribution is non-uniform and non-unique; it must at least be a cubic distribution. We also demonstrate that our theory can provide qualitative interpretation of a number of experiments involving pH-response-dependent shape transition in polyelectrolyte brushes.

Chapter 4: Ionic Current in pH and pOH responsive polyelectrolyte brush grafted nanochannels in the decoupled regime

In this chapter¹, the ionic current in nanochannels grafted with pH or pOH responsive polyelectrolyte brushes is computed in the decoupled regime. The ionic current results from the electromigration of the induced charge imbalance due to the formation of the net electric double layer or the EDL at the polyelectrolyte-electrolyte interface. Here calculations show the effect of the parameters such as the PE charge content, salt concentration, pH and pOH, acid or base dissociation constants (pK_a or pK_b) etc. on the ionic current. Given the ubiquitous use of the change in the current-voltage response characteristics of a nanochannel to sense a bioanalyte or fabricate a nanofluidic diode or rectifier, these findings are expected to influence several applications associated with functionalized and “smart” PE-grafted nanochannels.

¹Contents of this chapter have been published as: *G. Chen and S. Das, Scaling laws and ionic current inversion in polyelectrolyte-grafted nanochannels. J. Phys. Chem. B, Vol. 119, pp. 12714-12726 (2015).*

4.1 Introduction

Ionic current in a nanofluidic channel refers to the current developed due to the opposite migration of the oppositely charged mobile ions present within an EDL in presence of an externally applied electric field [67,68]. In this chapter, we compute the ionic current induced in the presence of an externally applied axial electric field in a PE-brush-grafted nanochannels, where the PE brushes are modelled in the decoupled regime. We consider the case where the PE brushes are negative and pH responsive. Calculations are provided as a function of several parameters: values of bulk pH (or pH_∞), salt concentration, maximum charge content of the PE, constant of ionization or dissociation of the acid responsible for the PE acquiring the charges, etc.

Quantifying ionic current is central to a number of applications of nanochannels with and without PE grafting; some of these applications are sensing and detecting biomolecules [33], devising nanofluidic diodes and rectifiers [30–32], and so on. For all of these applications, it is paramount to know the base state current. For example, the knowledge of the change of the base state current or the resulting change of the current-voltage characteristics, on account of the passage of a bioanalyte, is fundamental in nanochannel sensing of the bioanalyte [69–71]. Our study describes the fundamental nature of this base current (or base state current-voltage characteristics), including the highly interesting inversion of the base current, which, in turn, will help fabricate a much more efficient PE-grafted nanochannel sensor for biosensing applications.

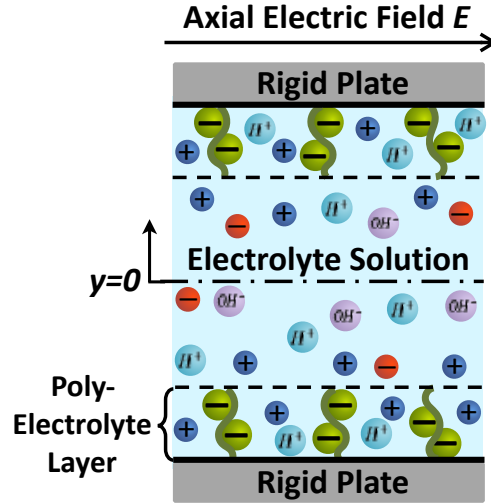


Figure 4.1: Schematic of the nanochannel grafted with (a) negatively charged PE layer and (b) positively charged PE layer. The schematic also shows the direction of the applied electric field that triggers the nanochannel ionic current. The figure is taken from Chen and Das [8].

4.2 Results

In chapter 3, we have provided the detailed calculation for the electrostatics of the pH and pOH responsive PE-brush-grafted nanoconfined systems in the decoupled regime. Once the electrostatic potential has been computed, it can be employed to calculate the corresponding number density distribution of the ions n_i ($i = \pm, H^+ OH^-$) – as has been well illustrated in chapter 3, this number density will always obey the Boltzmann distribution except for the H^+ (OH^-) ions within the PE brush layer for negative (positive) PE brush layer. Subsequently, under the condition that an axial electric field has been applied (see Fig. 4.1), we can obtain the ionic current (i_{ion}) as:

$$i_{ion} = eE \int_{-h}^h \left(\sum_i \mu_i n_i \right) dy, \quad (4.1)$$

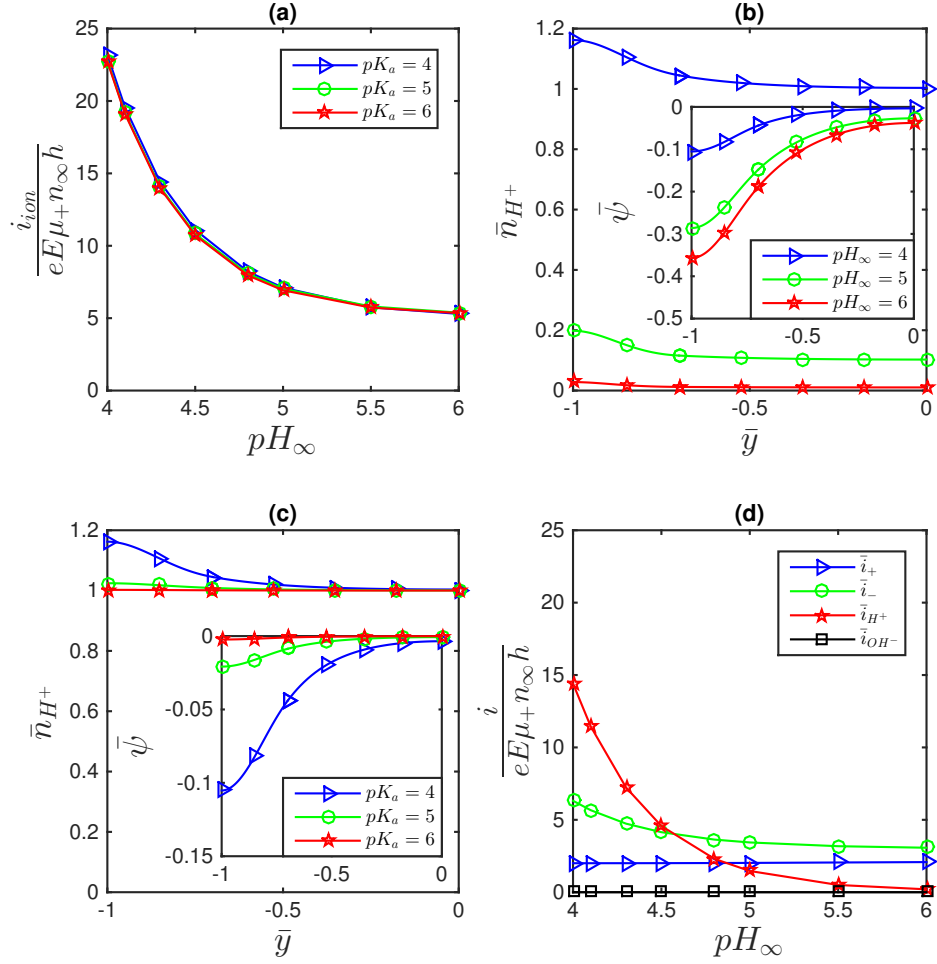


Figure 4.2: (a) Variation of the ionic current with pH_∞ for different values of pK_a for a negatively charged PE layer. Here we consider the electrolyte salt as $NaCl$ and the acid as HCl . The relevant unsigned mobility values are $\mu_+ = \mu_{Na^+} = 5 \times 10^{-8} m^2/Vs$, $\mu_- = \mu_{Cl^-} = 7.9 \times 10^{-8} m^2/Vs$, $\mu_{H^+} = 36 \times 10^{-8} m^2/Vs$, and $\mu_{OH^-} = 20 \times 10^{-8} m^2/Vs$. (b) Variation of the dimensionless number density of H^+ ion ($\bar{n}_{H^+, \infty}$) and the dimensionless electrostatic potential ($\bar{\psi}$) (shown in the inset) with \bar{y} for different values of pH_∞ for $pK_a = 4$. (c) Variation of the dimensionless number density of H^+ ion ($\bar{n}_{H^+, \infty}$) and the dimensionless electrostatic potential ($\bar{\psi}$) (shown in the inset) with \bar{y} for different values of pK_a for $pH_\infty = 4$. (d) Variation of the dimensionless ionic currents with pH_∞ due to different ions [$\bar{i}_+ = \frac{i_+}{eE\mu_+n_\infty h}$, $\bar{i}_- = \frac{i_-}{eE\mu_+n_\infty h}$, $\bar{i}_{H^+} = \frac{i_{H^+}}{eE\mu_+n_\infty h}$, $\bar{i}_{OH^-} = \frac{i_{OH^-}}{eE\mu_+n_\infty h}$] for $pK_a = 6$. For all the plots, we use $c_\infty = 10^{-4} M$ (i.e., $n_\infty = c_\infty \times N_A \times 10^3 = 6.023 \times 10^{22} 1/m^3$), $\gamma_a = 10^{-4} M$, $\bar{d} = 0.3$, $h = 100 nm$, $k_B T = 4.14 \times 10^{-21} J$, $e = 1.6 \times 10^{-19} C$, $\epsilon_0 = 8.8 \times 10^{-12} F/m$, and $\epsilon_r = 79.8$.

where μ_i is the unsigned electrophoretic mobility of species i ($i = \pm, H^+, OH^-$) and E is the magnitude of the applied axial electric field.

Based on the electrostatics study done in Chapter 3, we later optimized our simulation and identified the parameters that are most likely to be encountered in experiments. Fig. 4.2(a) provides the variation of the ionic current with pH_∞ (or bulk pH) for different values of pK_a . Larger pH_∞ will signal a more pronounced depletion of the H^+ and hence a larger extent of dissociation of the acid group producing the PE charge. Accordingly, the PE will be more strongly charged, leading to a larger value of EDL potential [see the inset in Fig. 4.2(c)]. Despite a more augmented value of the EDL potential, however, we witness a reduced value of the ionic current at a larger pH_∞ [see 4.2(a)]. This is non-trivial since in a nanochannel one expects the ionic current to be dominated by the EDL current; hence a larger ionic current for cases with larger EDL electrostatic potential. In the present case however, it is the bulk mobility of the H^+ ions that dictate the overall ionic current at such low pH_∞ . Small pH_∞ indicate a large value of the hydrogen ion concentration – since H^+ ions have very large mobility values, the overall ionic current at such a low pH_∞ gets dictated by this bulk mobility of the H^+ ions leading to a very large ionic current at small pH_∞ . In Fig. 4.2(d), we show the separate contribution of the different ions to this ionic current – the significantly augmented influence of the H^+ ions at low pH_∞ becomes very much evident. Of course, the relatively insignificant variation of the ionic current with pK_a [see Fig. 4.2(a)] can be explained by the corresponding insignificant variation of the hydrogen ion number density with pK_a [see Fig. 4.2(c)]. On the other hand, the effect of variation of pH_∞ on distinctly changing the hydrogen

ion number density – the factor responsible for augmented ionic current at small pH_∞ – is very much clear from Fig. 4.2(b).

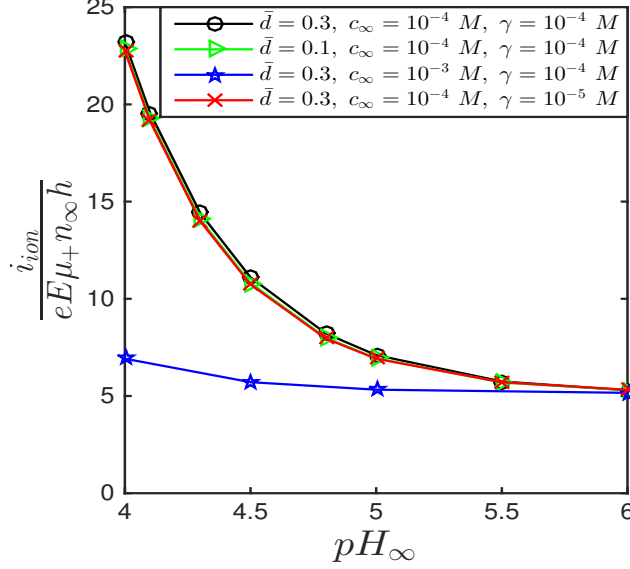


Figure 4.3: Variation of the ionic current with pH_∞ for a negatively charged PE layer for $pK_a = 4$ and for different values of \bar{d} , γ_a , and c_∞ . Other parameters, including the unsigned mobility values of the different ions, are identical to that used in Fig. 4.2.

In Fig. 4.3, we show the effect of the parameters (c_∞ , \bar{d} , and $\bar{\gamma}$, please see Chapter 3 for the definition of these parameters) on the overall nanochannel ionic current. We find that increase in salt concentration increases the ionic current. This increases can be understood by noting that we plot $i_{ion}/(eE\mu_+n_\infty h)$ – hence, based on the plots in Fig. 4.3, $(i_{ion})_{c_\infty=10^{-3} M}$ will be larger than $(i_{ion})_{c_\infty=10^{-4} M}$. The reason for such an increase in the ionic current with an increase in the salt concentration stems from the fact that the ionic current is proportional to the salt concentration. Unlike c_∞ , other parameters have relatively less influence on the overall ionic current.

4.3 Conclusions

In this chapter we have calculated the ionic current for pH-responsive PE-brush-grafted nanochannels, with the brushes being modelled in the de-coupled regime. The calculations establish that the thermodynamics and the electrostatics model for nanoconfined PE brushes in the decoupled regime developed in Chapter 3 can be successfully applied to probe an electrokinetics problem, namely the generation of the ionic current in such brush-grafted nanochannels. Results indicate, most intriguingly, an overall ionic current that is not dictated by the EDL current, despite the current being calculated in a charged nanochannel. We establish that such an occurrence typically occur for small values of bulk pH, when the presence of the excess H^+ ions and their large mobilities completely overwhelm the effect of lowering (at small pH_∞) of the corresponding EDL potential. This ionic current calculation will be an important first step to better analyze and understand the extensive use of the PE-brush-grafted nanochannels for applications (e.g., biosensing, analyte sensing, current rectification, generation of diodic action, etc.) that depend on precise and highly sensitive quantification of the ionic current.

Chapter 5: Electroosmotic transport in pH responsive polyelectrolyte brush grafted nanochannels in the decoupled regime

In this chapter¹, we develop a theory to study the electroosmotic (EOS) transport in a pH-responsive polyelectrolyte-brush-grafted (or soft) nanochannel with the PE brushes being modelled in a decoupled regime. In chapter 3, we have identified that explicit consideration of hydrogen ion concentration is mandatory for appropriately describing the electrostatics of such systems and the resulting monomer concentration must obey a non-unique, cubic distribution. Here, we use this electrostatic calculation to study the corresponding EOS transport. We establish that the effect of pH-responsiveness of the PE brushes introduces two separate issues in the context of the EOS transport in the polyelectrolyte-brush-grafted nanochannels : first is the consideration of the hydrogen and hydroxyl ion concentrations in describing the EOS body force, and second is the consideration of the appropriate drag force that bears the signature of this cubic monomeric distribution. Our results indicate that the strength of the EOS velocity for the

¹Contents of this chapter have been published as: *G. Chen and S. Das, Electroosmotic transport in polyelectrolyte-grafted nanochannels with pH-dependent charge density. J. Appl. Phys., Vol. 117, pp. 185304 (2015).*

pH-dependent case is always smaller than that for the pH-independent case, manifested in an extremely small value of the ratio of EOS to ionic current. Such a nature of the EOS transport will be extremely significant in suppressing the EOS flow strength with implications in a large number applications such as capillary electrophoresis induced separation, electric field mediated DNA elongation, electrophoretic DNA nanopore sequencing, and many more.

5.1 Introduction

Understanding the transport of liquid and ions in nanochannels forms the foundational basis of employability of such nanochannels in different applications in nanoscale sensing, valving, and detection [27–33]. Given the reduced size of the fluidic channels, pressure-driven transport is often not a desired scenario owing to the large pressure drop that scales inversely as the channel height for a given desired value of the flow velocity. Electroosmotic (EOS) transport has evolved as a much more favorable alternative on account of its operating principle that makes it extremely amenable to initiating liquid transport in a charged nanofluidic channel. This principle involves transport of electrolyte ions within the triggered EDL of the nanochannel in presence of an externally applied axial electric field, and the subsequent dragging of water molecules that remain attracted to these ions via the hydrogen bonding. Since counterions are in excess within the EDL, this transport mechanism invariably transports water in the direction in which the counterions migrate in presence of the external axial electric field.

There have been some studies on quantifying the EOS transport in PE-grafted nanochannels – these studies employ both continuum and atomistic simulations [35, 53, 76–79]. Given the fact that the modelling of the pH-dependent ionization is very difficult to capture through atomistic simulations and the fact that the continuum analysis has invariably neglected the appropriate role of H^+ ion concentration in the modelling of the pH-responsive PE-brush-grafted nanochannels (as illustrated in details in chapter 3), there is virtually no study that describes the EOS transport in the PE-brush-grafted nanochannels shedding light on the appropriate role of the pH-responsiveness of the PE brushes.

In this chapter, we provide possibly the first study that quantifies the EOS transport in a nanochannel grafted with pH-responsive PE-brushes, with the brushes being modelled in the decoupled regime with a correct accounting of the contribution of the H^+ ions. In the proposed model, firstly, appropriate monomeric distribution is considered in order to calculate the corresponding drag coefficient that affects the EOS transport. Secondly, we account for the hydrogen and hydroxyl ions, along with the electrolyte ions, for dictating the net charge density that interacts with the applied electric field to trigger the driving EOS body force. The central result of this chapter is that the EOS velocity is substantially weaker for the case of the PE layer systems with pH-dependent charge density. Degree of this lowering is of course a function of the system parameters, and the corresponding variation exhibits richer behavior for those parameters that affect both the monomer distribution as well as the PE-layer-EDL electrostatics. We further demonstrate that such unique EOS behavior can be extremely significant in suppressing the EOS flow strength in polyelectrolyte-grafted

nanochannels. Such suppression is well beyond the extent typically witnessed in standard polyelectrolyte/polymer-grafted or polyelectrolyte/polymer-adsorbed capillaries [80–84] and therefore can have large impact in nanochannel electrophoresis based applications such as ion separation [85, 86], DNA elongation [87], DNA sequencing [88], and many more.

5.2 Theory

5.2.1 Electroosmotic transport in the polyelectrolyte-grafted nanochannel with pH-dependent charge density

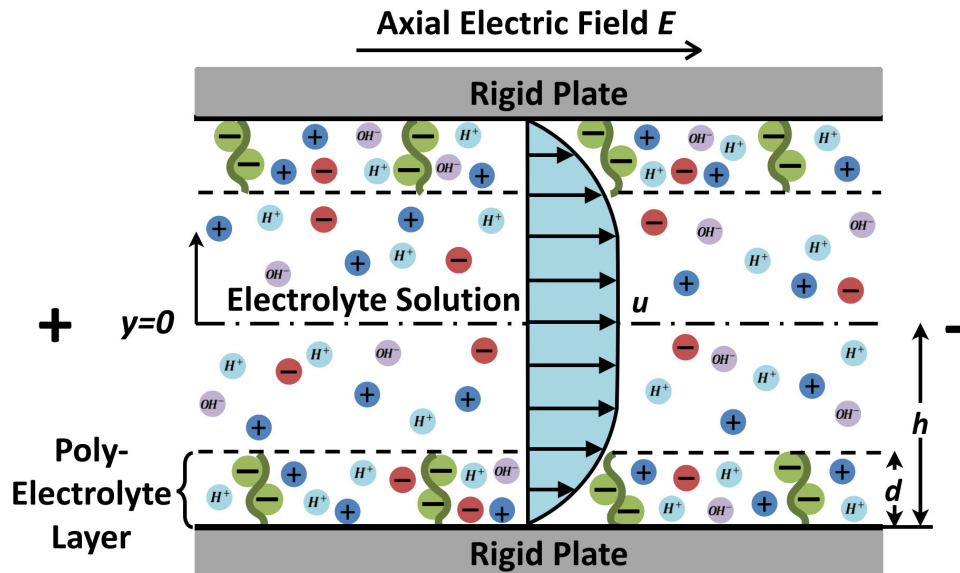


Figure 5.1: Schematic of the electroosmotic flow profile in a PE-grafted nanochannel. The PE ions are shown in green.

As shown in Figure 5.1, we consider a steady-state, one dimensional, fully-

developed axial EOS transport in presence of an externally applied axial electric field E in a PE-grafted nanochannel with pH-dependent charge density. This EOS transport is triggered by the interplay of the applied electric field and the net charge density within the EDL dictated by the number densities of the salt ions as well as H^+ and OH^- ions. Here we shall use the formulation provided in Chapter 3, where one accounts for the contribution of the H^+ ions explicitly within the PE brush layer, in order to quantify these number densities. The equation governing the EOS velocity field u , on the other hand, is given by:

$$\begin{aligned} \eta \frac{d^2 u}{dy^2} + e(n_+ - n_- + n_{H^+} - n_{OH^-})E - \mu_c u &= 0 \quad [\text{for } -h \leq y \leq -h + d], \\ \eta \frac{d^2 u}{dy^2} + e(n_+ - n_- + n_{H^+} - n_{OH^-})E &= 0 \quad [\text{for } -h + d \leq y \leq 0]. \end{aligned} \quad (5.1)$$

In eq.(5.1), η is the dynamic viscosity of the liquid, and $\mu_c = (\frac{\varphi(y)}{b})^2$ (b is a parameter that has a unit of $length/\sqrt{viscosity}$) is the drag coefficient within the PE layer. For definition of the other variables, kindly refer to the discussions following eq.(3.2). Eq.(5.1) is expressed under several simplifying assumptions. Firstly, we assume that the background flow field does not alter the shape of the grafted PE layer under steady state (we discuss the validity of this assumption later). Secondly, the timescale (τ_{EDL}) of distribution of the EDL ions ($\tau_{EDL} \sim \lambda^2/D_{ion} \sim 10^{-10} - 10^{-6}$ s, with EDL thickness $\lambda \sim 1 - 100$ nm and ion diffusivity $D_{ion} \sim 10^{-8} m^2/(Vs)$) is considered much smaller than the time scale associated with the pressure-driven liquid transport [89]. This assumption allows us to consider the EDL ion distribution as quasi-steady with respect to the flow field, thereby sufficing to express the flow field through eq.(5.1) without requiring the coupled Poisson-Nernst-Planck and Navier Stokes equations to

describe the flow field and ion transport [53]. Thirdly, in eq.(5.1) the drag coefficient (μ_c) is expressed assuming that $\mu_c \sim K^2$, where K^{-1} (which varies as φ^{-1}) is the length that screens the background flow from the flow inside the grafted PE molecules. This analysis is borrowed from the idea of flow screening between the inside and the outside of a polymer coil where the background flow velocity is much larger than the velocity inside the polymer coil [90, 91]; the justification of applying this analysis to the present case of grafted PE molecules is that the PE molecules (just like the polymer coil), being grafted, will have a velocity that is much smaller than the background velocity [25]. Finally, we assume that the penetration depth (ℓ_p) of the flow into the polymer brush is at least equal to the height of the PE layer (d). Considering a simplified situation where $\ell_p \sim \ell \sim \sigma^{-1/2}$ (where ℓ is the spacing between grafted PE brushes and σ is the grafting density) [92, 93], such a condition necessitates $\sigma < 1/d^2$. Please note that the ionic number densities (n_i) appearing in eq.(5.1) are the expressions obtained by minimizing the electrostatic free energy – see chapter 3 for the detailed expressions.

Eq.(5.1) can be expressed in dimensionless form as:

$$\begin{aligned} \frac{d^2 \bar{u}}{d\bar{y}^2} + \frac{\bar{E}}{2\bar{\lambda}^2} [\exp(-\bar{\psi}) - (1 + \bar{n}_{H^+, \infty}) \exp(\bar{\psi}) - \bar{n}_{OH^-, \infty} \exp(\bar{\psi}) + \bar{n}_{H^+}] - \bar{\alpha}^2 \varphi^2 \bar{u} &= 0 \\ [-1 \leq \bar{y} \leq -1 + \bar{d}], & \\ \frac{d^2 \bar{u}}{d\bar{y}^2} + \frac{\bar{E}}{2\bar{\lambda}^2} [\exp(-\bar{\psi}) - (1 + \bar{n}_{H^+, \infty}) \exp(\bar{\psi}) - \bar{n}_{OH^-, \infty} \exp(\bar{\psi}) + \bar{n}_{H^+, \infty} \exp(-\bar{\psi})] &= 0 \\ [-1 + \bar{d} \leq \bar{y} \leq 0]. & \end{aligned} \quad (5.2)$$

In eq. (5.2), $\bar{u} = \frac{u}{u_0}$ (where $u_0 = \frac{k_B T \epsilon_0 \epsilon_r E_0}{e \eta}$ is the EOS velocity scale; E_0 is the scale of the electric field), $\bar{E} = \frac{E}{E_0}$, and $\bar{\alpha} = \frac{h}{b\sqrt{\eta}}$. Solution of eq.(5.2) is sought in presence of the following dimensionless boundary conditions:

$$\begin{aligned} \left(\frac{d\bar{u}}{d\bar{y}}\right)_{\bar{y}=-1} &= 0, & (\bar{u})_{\bar{y}=(-1+\bar{d})^+} &= (\bar{u})_{\bar{y}=(-1+\bar{d})^-}, \\ \left(\frac{d\bar{u}}{d\bar{y}}\right)_{\bar{y}=0} &= 0, & \left(\frac{d\bar{u}}{d\bar{y}}\right)_{\bar{y}=(-1+\bar{d})^+} &= \left(\frac{d\bar{u}}{d\bar{y}}\right)_{\bar{y}=(-1+\bar{d})^-}. \end{aligned} \quad (5.3)$$

5.2.2 Electroosmotic transport in the polyelectrolyte-grafted nanochannel with pH-independent charge density

This is the limiting case of the above formulation. Such pH-independence leads to several simplifications, and the resulting equations have been already derived and solved in several previous studies including those by the present author(s). Here we briefly discuss these simplified governing equations, since in the Results section we shall compare this case with the EOS transport in polyelectrolyte-grafted nanochannels. When the charge density of the grafted polyelectrolytes is independent of the pH, the number density of the polyelectrolyte ions is constant, and the corresponding potential distribution (ignoring the explicit hydrogen and hydroxyl ion distribution) can be expressed as:

$$\begin{aligned} \frac{d^2\psi}{dy^2} &= \frac{e(n_- - n_+ + \varphi n_{A^-})}{\epsilon_0 \epsilon_r} & [\text{for } -h \leq y \leq -h + d], \\ \frac{d^2\psi}{dy^2} &= \frac{e(n_- - n_+)}{\epsilon_0 \epsilon_r} & [\text{for } -h + d \leq y \leq 0]. \end{aligned} \quad (5.4)$$

Please note that eq.(5.4) is effectively derived from the simplified version of

the free energy formulation, ψ can be obtained by solving eq.(5.4) in presence of the boundary conditions expressed in eq.(3.8). An analytical solution of ψ becomes possible for weak values of the electrostatic potential which allows the employment of the Debye-Hckel linearization; however, for larger values of the potential a numerical solution is mandatory.

The dimensionless form for eq.(5.3) is:

$$\begin{aligned}\frac{d^2\bar{\psi}}{d\bar{y}^2} &= \frac{1}{2\bar{\lambda}^2} [\exp(\bar{\psi}) - \exp(-\bar{\psi}) + \varphi\bar{\gamma}_a] && [\text{for } -1 \leq \bar{y} \leq -1 + \bar{d}], \\ \frac{d^2\bar{\psi}}{d\bar{y}^2} &= \frac{1}{2\bar{\lambda}^2} [\exp(\bar{\psi}) - \exp(-\bar{\psi})] && [\text{for } -1 + \bar{d} \leq \bar{y} \leq 0].\end{aligned}\quad (5.5)$$

Finally, for this simplified case, the velocity field is expressed as:

$$\begin{aligned}\eta \frac{d^2u}{dy^2} + e(n_+ - n_-)E - \mu_c u &= 0 && [\text{for } -h \leq y \leq -h + d], \\ \eta \frac{d^2u}{dy^2} + e(n_+ - n_-)E &= 0 && [\text{for } -h + d \leq y \leq 0].\end{aligned}\quad (5.6)$$

The corresponding dimensionless form is:

$$\begin{aligned}\frac{d^2\bar{u}}{d\bar{y}^2} + \frac{\bar{E}}{\bar{\lambda}^2} [\sinh(\bar{\psi})] - \bar{\alpha}^2 \varphi^2 \bar{u} &= 0 && [-1 \leq \bar{y} \leq -1 + \bar{d}], \\ \frac{d^2\bar{u}}{d\bar{y}^2} + \frac{\bar{E}}{\bar{\lambda}^2} [\sinh(\bar{\psi})] &= 0 && [-1 + \bar{d} \leq \bar{y} \leq 0].\end{aligned}\quad (5.7)$$

\bar{u} for this pH-independent case will be obtained by solving eq.(5.7) in presence of the Boundary Conditions expressed in eq.(5.3).

5.3 Results

Figs. 5.2-5.4 provide the variation of $\bar{\psi}$, \bar{n}_{H^+} , and most importantly \bar{u} (dimensionless EOS velocity) elucidating the influence of different parameters dictating the

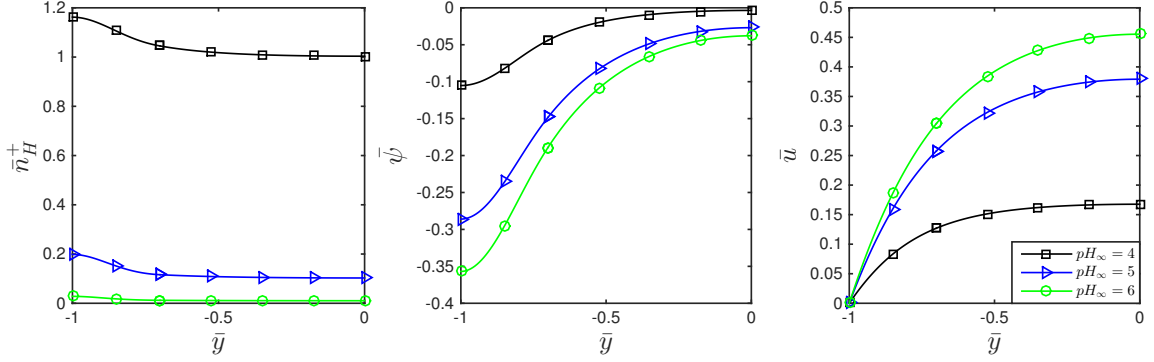


Figure 5.2: Variation of (a) dimensionless hydrogen ion number density, (b) dimensionless electrostatic potential, and (c) dimensionless electroosmotic velocity profile for various bulk pH or pH_∞ values, namely $pH_\infty = 4, 5, 6$. Other parameters used to generate the figures are $c_\infty = 10^{-4} M$, $\bar{d} = 0.3$, $\gamma_a = 10^{-4} M$, $pKa = 4$, $h = 100$ nm, $\alpha = 1$, $u_r = 1$, $N_p a_k^3 \sigma / d = 1$, $k_B T = 4.14 \times 10^{-21}$ J and $e = 1.6 \times 10^{19} C$.

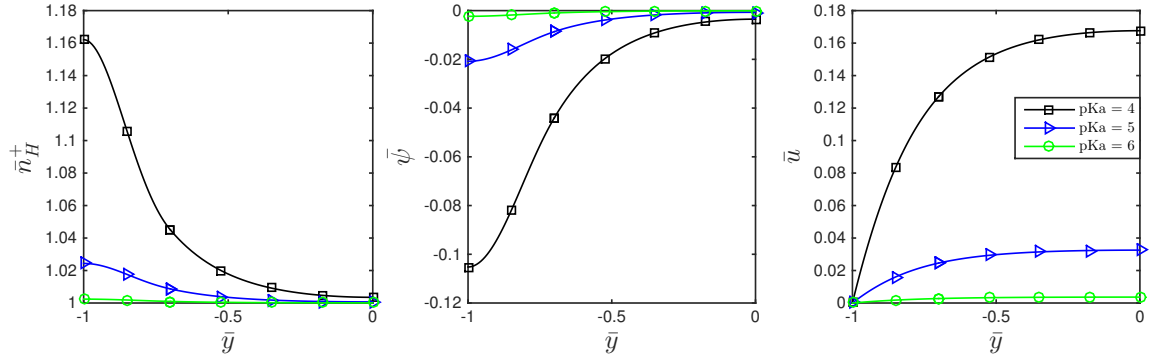


Figure 5.3: Variation of (a) dimensionless hydrogen ion number density, (b) dimensionless electrostatic potential, and (c) dimensionless electroosmotic velocity profile for different pKa values, namely $pKa = 4, 5, 6$ for $pH = 4$. Other parameters used to generate the figures are identical to Figure 5.2

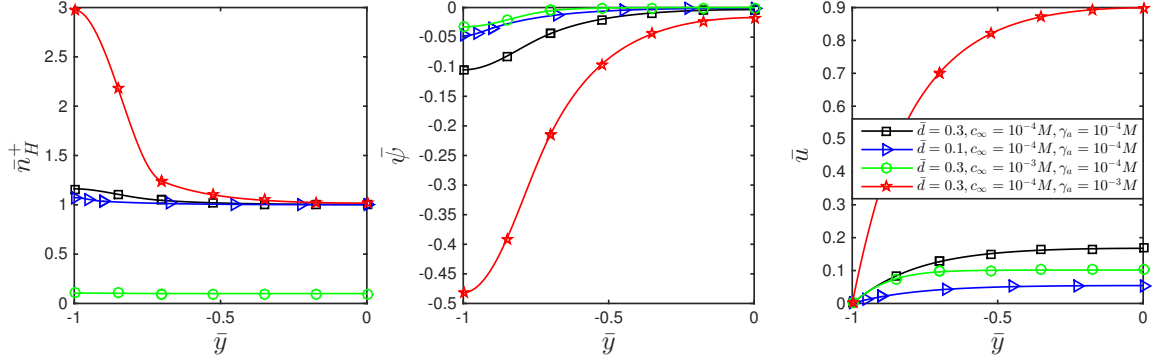


Figure 5.4: Variation of (a) dimensionless hydrogen ion number density, (b) dimensionless electrostatic potential, and (c) dimensionless electroosmotic velocity profile for different sets of parameter space. Other parameters used to generate the figures are $pH = 4$, $pKa = 4$, $h = 100$ nm, $\alpha = 1$, $u_r = 1$, $N_p a_k^3 \sigma / d = 1$, $k_B T = 4.14 \times 10^{-21}$ J and $e = 1.6 \times 10^{19}$ C.

problem. These are the main results of this chapter. Of course in chapter 3, we have discussed the profiles of $\bar{\psi}$ and \bar{n}_{H^+} ; here, we repeat some of these discussions in order to better explain the corresponding variation of the EOS velocity profiles.

Fig. 5.2 quantifies the effect of the variation of bulk pH (or pH_∞). Increase in pH_∞ or equivalently a decrease in the bulk hydrogen ion concentration indicates a condition of depleted hydrogen ions in the medium; this leads to a more enhanced dissociation of the PCS (as discussed in chapter 3). Consequently, for larger pH_∞ , both the electrostatic potential and the EOS velocity get enhanced.

Fig. 5.3 demonstrates the effects of the variation of pKa . Smaller pKa causes a more pronounced dissociation of the PCS, leading to a more enhanced value of the electrostatic potential and the EOS velocity.

Fig. 5.4 shows the effect of parameters \bar{d} (dimensionless brush height), c_∞ (ion concentration), and dimensionless maximum site density ($\bar{\gamma}$). Increase in \bar{d} increases

the total charge of the PE layer [35], which in turn enhances the magnitude of $\bar{\psi}$. This enhancement supersedes the effect of enhanced drag force imparted by a thicker PE layer. As a consequence, there is a net enhancement of the EOS velocity. Increase in $\bar{\gamma}$ implies a larger value of PE charge for a given pH_∞ – this results in an augmented $\bar{\psi}$ and \bar{u} . Finally, smaller ionic concentration leads to an enhanced EDL thickness, which in turn leads to greater uniformity of $\bar{\psi}$ values across the nanochannel. Such uniformity reduces the EOS body force, thereby eventually reducing \bar{u} .

5.4 Discussion

5.4.1 Significance of the present study in different soft-nanochannel-based applications

Electric-field-driven transport in microchannels and nanochannels have been widely used for applications such as separation of ions and charged biological species, stretching of polymers like DNA, sequencing of DNA and many more. Virtually all these applications rely on the electrophoretic transport of the charged species, and rely on their different electrophoretic mobilities. Problem occurs when the EOS transport, triggered on account of the interaction of the applied electric with the ion distribution, gets superposed on the electrophoretic transport of the ions. For example during the electrophoretic separation, the ions get separated from one another on account of their different electrophoretic mobilities inducing different electrophoretic velocities. Resolution of this separation process depends on the extent of difference of their electrophoretic mobility. However, when an EOS velocity, which impacts all the

different ions equally gets superposed, the impact of the difference in electrophoretic mobility gets reduced, thereby worsening the separation resolution. Therefore, it has been a long-term practice to devise different methods that may suppress the electroosmotic flow strength in systems meant for applications that rely on electrophoretic transport of ions. One such method has been the use of a PE or a polymer coating on the inner walls of channels and capillaries [80–84] – presence of such a coating invariably leads to suppressed EOS transport due to increased drag exerted on the flow by the brushes. Here we go one step further and try to investigate the impact of such PE grafting in suppressing the EOS transport for the case where the PEs demonstrate a pH-dependent ionization and charging. In order to provide a quantitative comparison between the suppression behaviors for the pH-dependent and the pH-independent cases, we compare the electric field driven ion current (i_{ion}) and the EOS current (i_{eos}) for the two cases. The ionic current (i_{ion}) for pH-dependent and pH-independent PE-grafted nanochannels can be expressed as:

$$(i_{ion})_{pH-dependent} = eE \int_{-h}^h (\mu_+ n_+ + \mu_- n_- + \mu_{H^+} n_{H^+} + \mu_{OH^-} n_{OH^-}) dy, \quad (5.8)$$

$$(i_{ion})_{pH-independent} = eE \int_{-h}^h (\mu_+ n_+ + \mu_- n_-) dy \quad (5.9)$$

where μ_i is the unsigned electrophoretic mobility of species i ($i = \pm, H^+$ and OH^-).

We can write the EOS current (i_{eos}) for both cases as:

$$(i_{eos})_{pH-dependent} = e \int_{-h}^h u (n_+ - n_- + n_{H^+} - n_{OH^-}) dy, \quad (5.10)$$

$$(i_{eos})_{pH-independent} = e \int_{-h}^h u (n_+ - n_-) dy \quad (5.11)$$

Consequently, we may write:

$$\begin{aligned} & \left(\frac{i_{eos}}{i_{ion}} \right)_{pH\text{-dependent}} \tag{5.12} \\ &= \frac{\mu_{liq}}{\mu_+} \frac{1}{\bar{E}} \frac{\int_{-1}^1 \bar{u} \left[\exp(-\bar{\psi}) - (1 + \bar{n}_{H^+, \infty}) \exp(\bar{\psi}) + \bar{n}_{H^+} - \bar{n}_{OH^-, \infty} \exp(\bar{\psi}) \right] d\bar{y}}{\int_{-1}^1 \left[\exp(-\bar{\psi}) + \frac{\mu_-}{\mu_+} (1 + \bar{n}_{H^+, \infty}) \exp(\bar{\psi}) + \frac{\mu_{H^+}}{\mu_+} \bar{n}_{H^+} + \frac{\mu_{OH^-}}{\mu_+} \bar{n}_{OH^-, \infty} \exp(\bar{\psi}) \right] d\bar{y}}, \end{aligned}$$

where $\mu_{liq} = \frac{k_B T \epsilon_0 \epsilon_r}{e \eta}$.

Similarly for the pH-independent case, we may write:

$$\left(\frac{i_{eos}}{i_{ion}} \right)_{pH\text{-independent}} = \frac{\mu_{liq}}{\mu_+} \frac{1}{\bar{E}} \frac{\int_{-1}^1 \bar{u} [-2 \sinh(\bar{\psi})] d\bar{y}}{\int_{-1}^1 \left[\exp(-\bar{\psi}) + \frac{\mu_-}{\mu_+} \exp(\bar{\psi}) \right] d\bar{y}} \tag{5.13}$$

Please note that the EDL electrostatic potential (ψ) as well as the ionic number densities n_{\pm} (related to ψ through Boltzmann distribution) for the case with pH-independent charge density of the PE brush have been calculated using our previous models [35, 79].

Fig. 5.5 shows the variation of this ratio i_{eos}/i_{ion} for the cases with pH-dependent and pH-independent PE charge density. We clearly find that there is a massive lowering of this ratio for the case with pH-dependent PE charge density, indicating that such a situation massively favours EOS flow suppression, and therefore can be extremely useful for all applications reliant on measuring the soft-nanochannel ionic current.

5.4.2 Scaling calculations for flow induced deformation of PE brushes

A fundamental assumption in this entire derivation is that there is no flow-induced deformation of the grafted PE layers within the nanochannel. Below we propose a scaling estimate to check whether such an assumption is valid.

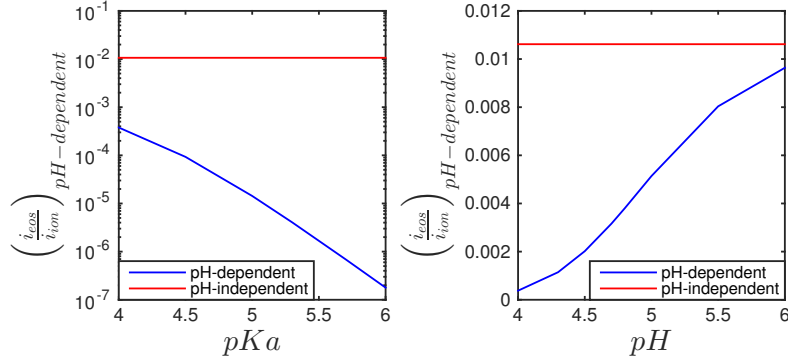


Figure 5.5: Variation of the ratio i_{eos}/i_{ion} for the cases with pH-dependent and pH-independent PE charge density. All the parameters are identical to that used in Fig. 5.2 and 5.3



Figure 5.6: Schematic of the flow induced deformation of the PE brush. The deformation is quantified by the angle θ . The flow is parallel to the grafting surface.

Following Kim et al. [94] we can obtain for stiff polymers (i.e., polymers whose Kuhn length a_k is much larger than the polymer contour length ℓ_{ct}) a closed form analytical expression for the deviation angle θ (with $\theta \ll 1$) of the PE brushes, quantifying the flow-induced deformation (see Fig. 5.6). From this analytical expression, we may write:

$$\theta \sim \frac{\zeta_0 \xi}{\kappa \lambda_\theta^3}, \quad (5.14)$$

where $\zeta_\theta = 3\pi\eta$ is the friction coefficient per unit length (η is the dynamic viscosity), $\lambda_\theta^2 = \zeta_\theta\rho/(\eta\ell_{ct}^2) = 3\pi\rho/\ell_{ct}^2$ (ρ is the number of grafted polymer molecules per unit contour length, i.e., $\rho = 1$ and $\rho = 10$ imply that the distance between two adjacent grafted polymer molecule is ℓ_{ct} and $\ell_{ct}/10$, respectively), κ is the bending rigidity (in units of $J.m$) of the polymer and $\xi = (\dot{\gamma}/\lambda_\theta) \cosh(\lambda_\theta\ell_{ct})$ (where $\dot{\gamma}$ is the shear rate). Consequently, using $\dot{\gamma} \sim u/\ell_{ct}$ (where u is the average flow velocity), we may re-write eq.(5.14) as:

$$\theta \sim \frac{3\pi\eta\dot{\gamma}}{\kappa\lambda_\theta^4} \sim \frac{\eta\dot{\gamma}\ell_{ct}^4}{3\pi\kappa\rho^2} \sim \frac{\eta u\ell_{ct}^3}{3\pi\kappa\rho^2}, \quad (5.15)$$

Table 5.1: Order of magnitude for θ for nano-confined stiff polymer brushes using eq.(5.15). We consider $\kappa \sim 10^{-28} J.m$ and $\eta = 10^{-3} Pa.s$.

u (m/s)	ℓ_{ct} (nm)	ρ	θ
10^{-6}	100	1	10^{-3}
10^{-5}	100	1	10^{-2}
10^{-4}	100	1	10^{-1}
10^{-6}	10	1	10^{-6}
10^{-5}	10	1	10^{-5}
10^{-4}	10	1	10^{-4}
10^{-6}	100	10	10^{-5}
10^{-5}	100	10	10^{-4}
10^{-4}	100	10	10^{-3}

In Table 5.1, we tabulate the possible θ values witnessed under the standard conditions of properties of PE molecules forming the brushes, different values of dimensionless grafting density ρ , and practical values of flow speeds ($10^{-4} - 10^{-6} m/s$) typically witnessed in nanofluidic channels [95]. As shown in the table 5.4.2 the deviation angle $\theta \ll 1$. Therefore, the deformation of nanoconfined stiff polymer brushes can be neglected.

Let us now consider the case where the grafted PE is flexible, i.e., Kuhn length a

Table 5.2: Order of magnitude for θ for nano-confined semi-flexible polymer brushes using eq.(5.15). We consider $\kappa \sim 10^{-28}$ *J.m* and $\eta = 10^{-3}$ *Pa.s*.

u (<i>m/s</i>)	a (<i>nm</i>)	ρ	θ
10^{-6}	10	1	10^{-6}
10^{-5}	10	1	10^{-5}
10^{-4}	10	1	10^{-4}
10^{-6}	1	1	10^{-9}
10^{-5}	1	1	10^{-8}
10^{-4}	1	1	10^{-7}
10^{-6}	10	10^{-1}	10^{-4}
10^{-5}	10	10^{-1}	10^{-3}
10^{-4}	10	10^{-1}	10^{-2}

is much smaller than the contour length ℓ_{ct} . Under this condition, the entire analysis (for the order of magnitude estimate) will remain the same except everywhere a_k will replace ℓ . Therefore, for this case, the grafting density ρ denotes the number of grafted polymer molecules per unit Kuhn length. Therefore, $\rho = 1$ and $\rho = 1/10$ imply that the distance (ℓ) between two adjacent grafted polymer molecule is a_k and $10a_k$. Of course, the brush configuration is attained for grafting distance $< a_k N_p^{3/5}$; hence for large N_p both $\rho = 1$ and $\rho = 1/10$ will form the brush. The same table as before, tabulating θ is shown in Table 5.2.

We can clearly find that the deviation angles θ shown in table 5.4.2 are very small for practical values of flow speed in nanochannels – therefore, we can surely

neglect the deformation of nanoconfined PE brushes.

5.5 Conclusions

In this chapter, we provide a new theory to calculate the EOS flow profile in nanochannels grafted with the PE layers that exhibit a pH-dependent charge density. The results demonstrate distinctly weakened EOS flow strength, and therefore establish such nanochannels as excellent EOS flow suppressors that can be successfully employed for a myriad of applications relying on electrophoretic transport of ions and charged bio-moieties.

Chapter 6: Configuration and electrostatics of end-charged nanoconfined polyelectrolyte brushes in the coupled regime: Salt concentration and pH dictated anomalous shrinking-swelling of the brushes

In this chapter¹, the configuration and the electrostatics of the end-charged polyelectrolyte (PE) brushes grafted on inner walls of a nanochannel has been modelled. The modelling has been done in the coupled regime, i.e., the electrostatic effects of the PE brushes and the induced EDL as well as the elastic and the excluded volume effects of the PE brush are assumed to simultaneously influence the behaviour of these nanoconfined brushes. First, semi-analytical results are proposed for pH-independent, weakly charged brushes. For these brushes, when the confinement effect is weak, i.e., $d_0 < h/2$ (d_0 is the PE brush height without electrostatic effects and h is nanochannel half height), $d > d_0$ (d is the brush height with the electrostatic effects), i.e., the brushes swell due to the

¹Contents of this chapter have been published as: (a) G. Chen and S. Das, *Anomalous shrinking-swelling of nanoconfined end-charged polyelectrolyte brushes: Interplay of confinement and electrostatic effects*. *J. Phys. Chem. B*, Vol. 120, 6848-6857 (2016); (b) G. Chen and S. Das, *Thermodynamics, electrostatics, and ionic current in nanochannels grafted with pH-responsive end-charged polyelectrolyte brushes*. *Electrophoresis*, DOI: 10.1002/elps.201600415 (2016).

electrostatic effects. Further for this case, increase in salt concentration decreases d . On the contrary, for the case where the confinement effect is strong (i.e., $d_0 > h/2$), $d < d_0$ (i.e., the electrostatic effects shrink the brushes) and increase in salt concentration increases the brush height. These findings reveal that the weakly charged, pH-independent end-charged brushes show three unique differences when compared to the behavior of the standard PE brushes with charges along their entire backbone. These differences are (a) presence of a distinct role of the confinement in dictating how electric double layer mediated electrostatic effects govern the height of end-charged brushes, (b) electrostatic-effect-driven shrinking of end-charged brushes for $d_0 > h/2$ (for backbone-charged brushes the electrostatic effects always swell the brushes), and (c) swelling of end-charged brushes with salt concentration for $d_0 > h/2$ (backbone-charged brushes always shrink with increase in salt concentration). In the second part of the chapter, pH-responsive, strongly charged brushes are analyzed numerically and results reveal much richer dependence of the brush height on the salt concentration as a function of the confinement. For example, we now witness that depending on the range of salt concentration, the PE brush height may either decrease or increase with the salt concentration for both weak ($d_0 < h/2$) and strong ($d_0 > h/2$) confinement regimes. These unique effects of confinement and electrostatics on PE brushes reported in this chapter have not been previously reported and we anticipate that these findings will shed new light on the structure and properties of PE-brush-functionalized nanochannels with implications in applications such as fabrication of functionalized-nanochannel-based nanofluidic diodes, valves, biosensors, current rectifiers, etc.

6.1 Introduction

From this chapter onwards, we shall only consider the behavior of the PE brushes in the coupled regime. Consideration of the coupled regime, or equivalently, a thermodynamically self-consistent modelling approach of the PE brushes implies that we account for the elastic and the excluded volume energies of a PE brush, in addition to the electrostatic energy of the PE brush and the energy of the induced electric double layer or EDL, in selecting the equilibrium brush configuration [45, 46]. Such a consideration implies that the analysis is being performed in the coupled regime. To the best of our knowledge, the analysis presented in this chapter will be one of the first studies on self-consistent continuum-based modelling of *nano-confined* PE brushes. Previous continuum-based studies on nano-confined PE brushes, including those that are discussed in chapters 2-5 of this thesis as well as those by other authors [8, 26, 52, 53, 56], have mostly considered the electrostatic problem to be decoupled from the brush equilibrium configuration, which in turn, has been assumed to be dictated solely by the balance of the PE excluded volume and elastic energies. In our recent study (described in chapter 2 of this thesis), we did establish the physical conditions when such a decoupling consideration, which effectively assumes the height of the nanoconfined PE brushes to be independent of the electrostatic or EDL effects, is valid. However, for situations where these physical conditions no longer exist, one will need to include the contributions of the elastic (entropic) and the excluded effects along with the PE electrostatic and the induced EDL effects in deciding the equilibrium of the PE brushes. This has been done in the present formulation,

where the PE brushes are assumed to be end-charged. Please note that such thermodynamically self-consistent modelling, where all the effects are considered, have been done previously for PEs (containing charges either along its entire backbone or localized only at its tip) grafted on single interfaces, i.e., without the confinement effects [45, 46, 96–98].

In this chapter we first analyze, employing semi-analytical approaches, the salt concentration dependent variation of the brush height and the resulting electrostatics for pH-non-responsive, weakly end-charged, nanoconfined brushes. The key finding for such brushes is that the electrostatic effects may shrink or swell the nano-confined PE brushes depending on the original (electrostatic-independent) brush thickness (d_0) (i.e., d_0 is the brush height for uncharged polymer brush). For example, for $d_0 < h/2$ (h is the nanochannel half height), i.e., when the effect of confinement is rather weak, electrostatic effect ensures that we invariably encounter a swelling of the PE brushes, i.e., $d > d_0$ (d is the brush height with the electrostatic effect). Secondly, for this case an increase in electrolyte concentration decreases d . On the other hand, for $d_0 > h/2$, i.e., the case where the confinement effect is much stronger, the electrostatic effects shrink the brush (i.e., $d < d_0$) and increase in salt concentration increases d . These confinement-driven results offer a new window of electrostatic-effects-mediated behaviour of PE brushes – the degree of confinement can be regulated to witness both swelling and shrinking of brushes under identical electrolyte concentration and at the same time ensure opposite dependences of the brush height on salt concentration. It is intriguing to compare these findings corresponding to the end-charged brushes with those for the PE brushes containing charges along their entire backbone. This latter

case has been studied extensively by scaling analysis [101–103], sophisticated mean-field models [104, 105], atomistic simulations [106–108], and experiments [109–113]. Our comparison demonstrates that the effect of confinement and electrostatics lead to deviation of the behavior of the end-charged brushes in three aspects: (a) confinement effects (i.e., whether $d_0 < h/2$ or $d_0 > h/2$) significantly influence the electrostatics-mediated end-charged brush height (b) for end-charged brushes electrostatic effects shrink the brushes for $d_0 > h/2$, while for the backbone-charged brushes the electrostatic effects always swell the brushes, and (c) end-charged brushes swell with increase in salt concentration for $d_0 > h/2$, while backbone-charged brushes invariably shrinks with an increase in the salt concentration. We finally justify these unique differences by a detailed free energy based argument for both the end-charged as well as backbone-charged brushes.

Following this calculation, in the second part of the chapter, we analyze the case of the pH-responsive, strongly end-charged PE brushes. The analysis is carried out numerically. Here we shall like to distinguish between the weakly charged and the strongly charged brushes – weakly charged brushes are those for which the induced EDL electrostatic potential is weak enough to allow the employment of Debye-Hückel linearization, while for the strongly charged brushes the EDL electrostatic potential becomes large enough to forbid the use of the Debye-Hückel linearization. We witness that for the pH-responsive brushes, a much richer salt-concentration dependence of the brush height is ensued – depending on the salt concentration, the brush height may either increase or decrease for both weak ($d_0 < h/2$) and strong ($d_0 > h/2$) confinements. Also, most of the effects are witnessed at large pH, i.e., the pH corre-

sponding to which there is the strongest pH-responsive ionization of the end charge of the PE brushes.

Finally we shall like to pinpoint the key assumptions that have been used to build up these models for pH-responsive and pH-non-responsive brushes. Firstly, we consider a uniform monomer distribution, or equivalently, a stepped monomer profile. Secondly, we do not consider any distribution for the free end of the brushes [98]. Therefore, the contribution of the elastic and excluded volume effects of the brush are modelled similar to the study of Tsori et al. [96]. Finally, the EDL free energy is modelled in a Poisson-Boltzmann (PB) framework, neglecting the effects of the non-PB elements such as finite ion sizes, finite solvent polarization, and ion-ion correlation effects.

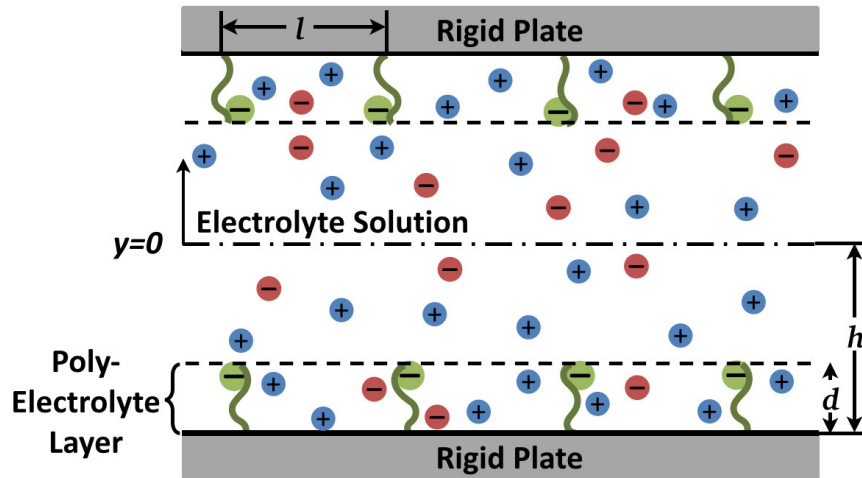


Figure 6.1: Schematic of the nanochannel grafted with end-charged PE layer.

6.2 Theory

We consider a nanochannel of height $2h$ grafted with a layer of end-charged PE molecules (see Fig. 6.1). The density of this charge at the PE tip may or may not be a function of the pH. Of course, the *grafting-density-polymer-size* combination is such that the grafted PE molecules form brushes and also *do not interpenetrate* with the brushes from the opposing wall (see Chapter 2 for details).

6.2.1 Governing Equations for pH-independent PE Brushes

In this case, the charge density at the non-grafted end of the end-charged PE brushes is independent of the local pH. We express the total free energy (F) of a single PE brush as the sum of the free energy associated with the PE brush (F_B) and the free energy associated with the formation of the EDL (F_{EDL}) on account of the charge at the end of the PE brush. Therefore:

$$F = F_B + F_{EDL} = F_{B,els} + F_{B,EV} + F_{B,elec} + F_{EDL}. \quad (6.1)$$

Eq.(6.1) is based on the fact that F_B consists of the elastic contribution ($F_{B,els}$), excluded volume contribution ($F_{B,EV}$), and the electrostatic contribution ($F_{B,elec}$) (due to the charge at the tip of the brush). Again the presence of this charge at the brush-tip triggers an electric double layer or EDL – F_{EDL} represents the energy associated with this EDL that is formed. This charge at the brush tip is quantified in terms of the charge density σ_{ch} (therefore, this charge density is the charge density at the PE-tip-electrolyte interface), which triggers a surface electrostatic potential ψ_s ,

at the PE-tip-electrolyte interface. Hence we may write, considering only the bottom half of the nanochannel, i.e., $-h \leq y \leq 0$:

$$F_{B,elec} = \int \sigma_{ch} \psi_s d^2 \mathbf{r}, \quad (6.2)$$

where this electrostatic contribution of the PE is localized at the PE-electrolyte interface ($y = -h + d$). In eq.(6.2), the charge density σ_{ch} is assumed to be constant and independent of the electrolyte salt concentration and pH. Also following Tsori et al. [96], we can express the elastic (entropic) and the excluded volume free energies of the PE brush as:

$$F_{B,els} = k_B T \frac{3}{2} \frac{d^2}{N_p a_k^2}, \quad (6.3)$$

$$F_{B,EV} = k_B T \frac{\omega N_p^2}{\ell^2 d} \quad (6.4)$$

In eqs.(6.3,6.4), $k_B T$ is the thermal energy, a_k is the PE Kuhn length, N_p is the number of monomer in a PE molecule, d is the PE brush height (to be determined self constantly later), $\omega = \frac{1-2\chi}{2} a_k^3$ is the excluded volume parameter, χ is the Flory-Huggins parameter, and ℓ is the lateral separation between the grafted PEs. Please note that while expressing the elastic and the excluded volume contributions, we have not considered the monomer distribution of the PE molecule along the depth of the PE molecule; in other words, we have considered a uniform monomer profile (or a stepped monomer profile, as proposed by Alexander [1] and de Gennes [2,3]).

Finally, F_{EDL} is expressed as:

$$F_{EDL} = \int \left[\int_{-h}^0 f_{EDL}(\psi, \psi', n_{\pm}) dy \right] d^2 \mathbf{r}, \quad (6.5)$$

where f_{EDL} is the EDL free energy density, ψ is the EDL electrostatic potential, ψ' is the gradient of the EDL electrostatic potential, and n_{\pm} are the number density of the electrolyte ions. The contribution of the EDL free energy is present in the entire nanochannel half height and depends on f_{EDL} that can be expressed as:

$$f_{EDL}(\psi, \psi', n_{\pm}) = -\frac{\epsilon_0 \epsilon_r}{2} \left| \frac{d\psi}{dy} \right|^2 + e\psi (n_+ - n_-) + k_B T \left[n_+ \left(\ln \left(\frac{n_+}{n_{+, \infty}} \right) - 1 \right) + n_- \left(\ln \left(\frac{n_-}{n_{-, \infty}} \right) - 1 \right) \right], \quad (6.6)$$

where ϵ_0 is the permittivity of free space, ϵ_r is the relative permittivity of water, e is the electronic charge, $k_B T$ is the thermal energy, and $n_{+, \infty} = n_{-, \infty} = n_{\infty}$ is the bulk number density of the electrolyte ions (for a nanochannel, this bulk density refers to the density of the ions in the reservoirs connecting the nanochannel [114, 115]). Also eq.(6.6) assumes that the electrolyte ions are monovalent and symmetric and the EDL electrostatics is modelled in a PB framework neglecting the contributions of the non-PB elements such as finite ion size, solvent polarization, and ion-ion correlation effects. Eq.(6.6) further assumes that the relative permittivity values for the solvent are identical inside and outside and the brush. Finally, eq.(6.6) considers that the electrolyte salt concentration is much larger than the H^+ and OH^- ion concentrations, and hence we do not consider the contribution of the number densities of H^+ and OH^- ions in f_{EDL} .

We get the complete free energy expression using eqs.(6.2,6.3,6.4,6.5,6.6) in eq.(6.1).

We subsequently obtain the equilibrium condition by minimizing this complete free energy expression with respect to the different variables. The procedure is discussed in details in the following subsection.

Of course, for an uncharged polymer brush, the free energy is simply the sum of $F_{B,els}$ and $F_{B,EV}$. Consequently, the equilibrium brush height (d_0) is obtained as [by considering eqs.(6.3,6.4)]:

$$\left[\frac{\partial}{\partial d} (F_{B,els} + F_{B,EV}) \right]_{d=d_0} = 0 \Rightarrow d_0 = N_p \left(\frac{a_k^5}{\ell^2} \right)^{1/3} \left(\frac{1-2\chi}{6} \right)^{1/3}. \quad (6.7)$$

Therefore for the uncharged polymer brush, we do recover the condition that the brush height scales as $N_p (a_k^5/\ell^2)^{1/3}$ [4, 5, 96].

6.2.2 Equilibrium conditions and non-dimensionalization for pH-independent PE Brushes

The purpose of this subsection is to demonstrate the effect of the PE end charge and the resulting EDL in a nano-confined system in changing the equilibrium brush height. To obtain this equilibrium condition, we shall minimize the free energy equation [obtained using eqs.(6.2,6.3,6.4,6.5,6.6) in eq.(6.1)] with respect to the variables governing the problem (namely ψ , ψ_s , n_{\pm} and d).

Minimizing with respect to ψ yields:

$$\frac{\delta F}{\delta \psi} = 0 \Rightarrow \frac{d^2 \psi}{dy^2} = -\frac{e(n_+ - n_-)}{\epsilon_0 \epsilon_r}. \quad (6.8)$$

Similarly minimization with respect to n_{\pm} yields:

$$\frac{\delta F}{\delta n_{\pm}} = 0 \Rightarrow n_{\pm} = n_{\infty} \exp \left(\mp \frac{e\psi}{k_B T} \right) \quad (6.9)$$

Using eq.(6.9) in eq.(6.8), we recover the well-known Poisson-Boltzmann equation, expressed as:

$$\frac{d^2 \psi}{dy^2} = \frac{2n_{\infty} e}{\epsilon_0 \epsilon_r} \sinh \left(\frac{e\psi}{k_B T} \right). \quad (6.10)$$

Eq.(6.10) is valid both inside and outside the PE brushes. We shall solve this equation separately inside and outside the brush. The necessary boundary conditions are:

$$\left(\frac{d\psi}{dy}\right)_{y=-h} = 0, \quad \left(\frac{d\psi}{dy}\right)_{y=0} = 0, \quad (\psi)_{(y=-h+d)^-} = (\psi)_{(y=-h+d)^+}. \quad (6.11)$$

Here we assume that the PE brush is grafted at a chargeless surface (located at $y = -h$), there is symmetry at the channel centreline ($y = 0$), and the electrostatic potential calculated from inside and outside the brush is identical at the brush-electrolyte interface (located at $y = -h + d$). We shall need a fourth condition that will relate the electrostatic potential gradient calculated from inside the brush to that calculated from outside the brush in terms of the PE end charge density σ_{ch} . This condition is obtained by minimizing eq.(6.1) with respect to ψ_s [see Appendix for the detailed derivation of eq.(6.12)]:

$$\frac{\delta F}{\delta \psi_s} = 0 \Rightarrow \psi'_s = -\frac{\sigma_{ch}}{\epsilon_0 \epsilon_r} \Rightarrow \left(\frac{d\psi}{dy}\right)_{y=(-h+d)^+} - \left(\frac{d\psi}{dy}\right)_{y=(-h+d)^-} = -\frac{\sigma_{ch}}{\epsilon_0 \epsilon_r} \quad (6.12)$$

Eq.(6.10) can be solved in presence of the boundary conditions expressed in eqs.(6.11,6.12).

Henceforth, we shall like to perform the entire analysis in terms of the dimensionless variables. Eqs.(6.10,6.11,6.12) can be expressed in dimensionless form as:

$$\frac{d^2 \bar{\psi}}{d\bar{y}^2} = \frac{\sinh(\bar{\psi})}{\bar{\lambda}^2}, \quad (6.13)$$

$$\left(\frac{d\bar{\psi}}{d\bar{y}}\right)_{\bar{y}=-1} = 0, \quad \left(\frac{d\bar{\psi}}{d\bar{y}}\right)_{\bar{y}=0} = 0, \quad (\bar{\psi})_{(\bar{y}=-1+\bar{d})^-} = (\bar{\psi})_{(\bar{y}=-1+\bar{d})^+}, \quad (6.14)$$

$$\left(\frac{d\bar{\psi}}{d\bar{y}}\right)_{\bar{y}=(-1+\bar{d})^+} - \left(\frac{d\bar{\psi}}{d\bar{y}}\right)_{\bar{y}=(-1+\bar{d})^-} = -\frac{\bar{\sigma}_{ch}}{\bar{\lambda}^2}. \quad (6.15)$$

In the above equations, $\bar{y} = y/h$, $\bar{d} = d/h$, $\bar{\psi} = \frac{e\psi}{k_B T}$, $\bar{\lambda} = \frac{\lambda}{h}$ ($\lambda = \sqrt{\frac{\epsilon_0 \epsilon_r k_B T}{2n_\infty e^2}}$ being the EDL thickness), and $\bar{\sigma}_{ch} = \frac{\sigma_{ch}}{2n_\infty e h}$. Eq.(6.13), under the assumption of small $\bar{\psi}$ or $|\bar{\psi}| < 1$ [this condition allows to simplify $\sinh(\bar{\psi}) \approx \bar{\psi}$, which is the well-known Debye-Hückel linearization], which is valid for small σ_{ch} (i.e., we consider weakly end-charged PE brushes), can be solved analytically in presence of the boundary conditions expressed in eqs.(6.14,6.15) to yield

$$\begin{aligned}\bar{\psi} &= \frac{\bar{\sigma}}{\bar{\lambda}} \frac{1}{\sinh\left(\frac{1}{\bar{\lambda}}\right)} \cosh\left(\frac{-1+\bar{d}}{\bar{\lambda}}\right) \cosh\left(\frac{\bar{y}+1}{\bar{\lambda}}\right) \quad [\text{for } -1 \leq \bar{y} \leq -1+\bar{d}], \\ \bar{\psi} &= \frac{\bar{\sigma}}{\bar{\lambda}} \frac{1}{\sinh\left(\frac{1}{\bar{\lambda}}\right)} \cosh\left(\frac{\bar{d}}{\bar{\lambda}}\right) \cosh\left(\frac{\bar{y}}{\bar{\lambda}}\right) \quad [\text{for } -1+\bar{d} \leq \bar{y} \leq 0].\end{aligned}\quad (6.16)$$

and $\bar{\psi}_s = \bar{\psi}|_{\bar{y}=-1+\bar{d}}$:

$$\bar{\psi}_s = \frac{\bar{\sigma}}{\bar{\lambda}} \frac{1}{\sinh\left(\frac{1}{\bar{\lambda}}\right)} \cosh\left(\frac{-1+\bar{d}}{\bar{\lambda}}\right) \cosh\left(\frac{\bar{d}}{\bar{\lambda}}\right) \quad (6.17)$$

Once $\bar{\psi}$ is known analytically, one can obtain an analytical expression for f_{EDL} or $\bar{f}_{EDL} = f_{EDL}/(k_B T n_\infty)$ from eq.(6.6)

$$\bar{f}_{EDL} = -\bar{\lambda}^2 \left| \frac{d\bar{\psi}}{d\bar{y}} \right|^2 - 2 \cosh(\bar{\psi}). \quad (6.18)$$

Eq.(6.16) provides the analytical expression for $\bar{\psi}$ and will also provide the analytical expression of $\frac{d\bar{\psi}}{d\bar{y}}$. Therefore, we can obtain an analytical expression for \bar{f}_{EDL} in presence of Debye-Hückel linearization [this linearization further allows us to simplify $\cosh(\bar{\psi}) = 1 + \bar{\psi}^2/2$]:

$$\begin{aligned}
\bar{f}_{EDL} &= -\frac{\bar{\sigma}^2 \cosh^2\left(\frac{-1+\bar{d}}{\lambda}\right)}{\bar{\lambda}^2 \sinh^2\left(\frac{1}{\lambda}\right)} \cosh\left(\frac{2(\bar{y}+1)}{\bar{\lambda}}\right) - 2 \quad [\text{for } -1 \leq \bar{y} \leq -1 + \bar{d}], \\
\bar{f}_{EDL} &= -\frac{\bar{\sigma}^2 \cosh^2\left(\frac{\bar{d}}{\lambda}\right)}{\bar{\lambda}^2 \sinh^2\left(\frac{1}{\lambda}\right)} \cosh\left(\frac{2\bar{y}}{\bar{\lambda}}\right) - 2 \quad [\text{for } -1 + \bar{d} \leq \bar{y} \leq 0].
\end{aligned} \tag{6.19}$$

Therefore the overall free energy of the system [see eqs.(6.1,6.2,6.3,6.4,6.5,6.6,6.19)] can be expressed in dimensionless form as:

$$\begin{aligned}
\bar{F} &= \frac{\alpha \bar{d}^2}{2 N_p} + \beta \frac{N_p^2}{\bar{d}} + \frac{1}{2\gamma} \int_{-1}^0 \bar{f}_{EDL} d\bar{y} + \frac{\bar{\sigma} \bar{\psi}_s}{\gamma} \\
&= \frac{\alpha \bar{d}^2}{2 N_p} + \beta \frac{N_p^2}{\bar{d}} + \frac{\bar{\sigma}^2}{4\gamma \bar{\lambda}} \frac{\cosh\left(\frac{1-2\bar{d}}{\lambda}\right) + \cosh\left(\frac{1}{\lambda}\right)}{\sinh\left(\frac{1}{\lambda}\right)} - \frac{1}{\gamma}
\end{aligned} \tag{6.20}$$

where $\bar{F} = \frac{F}{k_B T}$, $\alpha = \frac{3h^2}{a_k^2}$, $\beta = \frac{(1-2\chi)a_k^3}{2\ell^2 h}$ and $\gamma = \frac{1}{2\ell^2 h n_\infty}$. Eq.(6.20) has been obtained under the condition that the surface integral $\int A d^2 \mathbf{r}$ is approximately equal to $\ell^2 A$ (where A does not vary over the surface). By minimizing eq.(6.20) with respect to \bar{d} we shall finally obtain the algebraic equation governing equilibrium \bar{d} (denoted as $\bar{d}_{eq,PE}$) as:

$$\left(\frac{\delta \bar{F}}{\delta \bar{d}}\right)_{\bar{d}=\bar{d}_{eq,PE}} = 0 \Rightarrow \alpha \frac{\bar{d}_{eq,PE}}{N_p} - \beta \frac{N_p^2}{\bar{d}_{eq,PE}^2} - \frac{\bar{\sigma}^2}{2\gamma \bar{\lambda}^2} \frac{\sinh\left(\frac{1-2\bar{d}_{eq,PE}}{\lambda}\right)}{\sinh\left(\frac{1}{\lambda}\right)} = 0. \tag{6.21}$$

Eq.(6.21) is the new equation governing the effective brush height in presence of the EDL effects triggered by the grafted PE brush with end charge. $\bar{d}_{eq,PE}$ obtained by solving eq.(6.21) will be compared against the dimensionless height of the uncharged brush $\bar{d}_0 = d_0/h$ [see eq.(6.7)].

6.2.3 Governing Equations and Equilibrium for pH-responsive PE Brushes

In case the end-charged PE brushes are pH-responsive, there will be no change in eqs.(6.1,6.3,6.4,6.5); however, there will be changes in the expressions for the electrostatic energies of the PE brush ($F_{B,elec}$) and the EDL energy density f_{EDL} . We can express this modified $F_{B,elec}$ as:

$$F_{B,elec} = \int \psi_s \sigma_{ch,pH} d^2\mathbf{r} = \int \psi_s \sigma_{ch} \frac{K'_a}{K'_a + n_{H^+}|_{y=-h+d}} d^2\mathbf{r}. \quad (6.22)$$

In eq.(6.22), n_{H^+} is the number density of the hydrogen ions, $K'_a = 10^3 N_A 10^{-pK_a}$ (K_a being the dissociation constant of the acid that dissociates to produce the surface charge of the end-charged PE brush), and σ_{ch} is the maximum surface charge density in pH neutral solution, which is assumed to be constant and independent of the electrolyte salt concentration. Finally, the modified EDL energy density can be expressed as:

$$f_{EDL} = -\frac{\epsilon_0 \epsilon_r}{2} \left| \frac{d\psi}{dy} \right|^2 + e \sum_i z_i n_i + k_B T \sum_i n_i \left[n_i \left(\ln \left(\frac{n_i}{n_{i,\infty}} \right) - 1 \right) \right], \quad (6.23)$$

where $i = \pm$, H^+ OH^- and z_i is the valence of species i .

The equilibrium conditions will be obtained by minimizing the final energy equation [obtained by using eqs.(6.3,6.4,6.5,6.22,6.23) in eq.(6.1)] with respect to ψ , n_i (where $i = \pm$, H^+ OH^-), and d . Minimizing with respect to ψ and n_i (where $i = \pm$, H^+ OH^-), we shall eventually get:

$$\frac{d^2\psi}{dy^2} = -\frac{e}{\epsilon_0 \epsilon_r} \sum_i z_i n_i. \quad (6.24)$$

and

$$n_i = n_{i,\infty} \exp\left(-z_i \frac{e\psi}{k_B T}\right), \quad (6.25)$$

Eqs.(6.24, 6.25) are valid both inside and outside the PE brushes. Of course, we shall get a single governing equation in terms of ψ by using eq.(6.25) to replace n_i in eq.(6.24):

$$\frac{d^2\psi}{dy^2} = -\frac{e}{\epsilon_0\epsilon_r} \sum_i z_i n_{i,\infty} \exp\left(-z_i \frac{e\psi}{k_B T}\right), \quad (6.26)$$

where eq.(6.26) is valid both inside and outside the PE brush layer. We consider a system where the electrolyte contains ions of bulk number density n_∞ and an acid that furnishes the same anion as the electrolyte anion of number density $n_{H^+,\infty}$. Under these conditions, we can write: $n_{+,\infty} = n_\infty$ and $n_- = n_\infty + n_{H^+,\infty}$. Consequently, the final form of the equation governing the electrostatic potential distribution will be:

$$\begin{aligned} \frac{d^2\psi}{dy^2} = & -\frac{e}{\epsilon_0\epsilon_r} \left[n_\infty \exp\left(-\frac{e\psi}{k_B T}\right) - (n_\infty + n_{H^+,\infty}) \exp\left(\frac{e\psi}{k_B T}\right) \right] \\ & - \frac{e}{\epsilon_0\epsilon_r} \left[n_{H^+,\infty} \exp\left(-\frac{e\psi}{k_B T}\right) - n_{OH^-, \infty} \exp\left(\frac{e\psi}{k_B T}\right) \right]. \end{aligned} \quad (6.27)$$

Of course, here we shall primarily consider cases in the acidic regime ($pH < 7$) – therefore, the effect of water-dissociated H^+ ions have been neglected. Eq.(6.27) can be expressed in dimensionless form as:

$$\begin{aligned} \frac{d^2\bar{\psi}}{d\bar{y}^2} = & \frac{1}{2\lambda^2} [-\exp(-\bar{\psi}) + (1 + \bar{n}_{H^+,\infty}) \exp(\bar{\psi}) \\ & - \bar{n}_{H^+,\infty} \exp(-\bar{\psi}) + \bar{n}_{OH^-, \infty} \exp(\bar{\psi})], \end{aligned} \quad (6.28)$$

where $\bar{y} = \frac{y}{h}$, $\bar{d} = \frac{d}{h}$, $\bar{\psi} = \frac{e\psi}{k_B T}$, $\bar{\lambda} = \frac{\lambda}{h}$ ($\lambda = \sqrt{\frac{\epsilon_0 \epsilon_r k_B T}{2n_\infty e^2}}$ is the EDL thickness), $\bar{n}_{i,\infty} = \frac{n_{i,\infty}}{n_\infty}$ (where $i = \pm H^+ OH^-$), $\bar{n}_i = \frac{n_i}{n_\infty}$, $\bar{\sigma}_{ch} = \frac{\sigma_{ch}}{2ehn_\infty}$, and $\bar{K}'_a = \frac{K'_a}{n_\infty}$.

$\bar{\psi}$ can be obtained by solving eq.(6.28) numerically in presence of the boundary conditions expressed in eqs.(6.14,6.15) [of course, for the present case, σ_{ch} appearing in eq.(6.15) will be a function of the local pH]. \bar{n}_i can be obtained from $\bar{\psi}$ using eq.(6.25). $\bar{\psi}$ and \bar{n}_i thus obtained will be used in eq.(6.23) to obtain f_{EDL} , which can be expressed in dimensionless form as:

$$\bar{f}_{EDL} = \frac{f_{EDL}}{k_B T n_\infty} = -\bar{\lambda}^2 \left| \frac{d\bar{\psi}}{d\bar{y}} \right|^2 - [\exp(-\bar{\psi}) + (1 + \bar{n}_{H^+, \infty}) \exp(\bar{\psi}) + \bar{n}_{H^+, \infty} \exp(-\bar{\psi}) + \bar{n}_{OH^-, \infty} \exp(\bar{\psi})]. \quad (6.29)$$

Using this \bar{f}_{EDL} we can finally obtain the complete free energy expression in dimensionless form [i.e., the dimensionless version of the equation that can be obtained by employing eqs.(6.3,6.4,6.5,6.22,6.29) in eq.(6.1)]:

$$\bar{F} = \frac{\alpha}{2} \frac{\bar{d}^2}{N_p} + \beta \frac{N_p^2}{\bar{d}} + \frac{1}{2\gamma} \int_{-1}^0 \bar{f}_{EDL} d\bar{y} + \bar{\psi}_s \frac{\bar{\sigma}_{ch}}{\gamma} \frac{\bar{K}'_a}{\bar{K}'_a + \bar{n}_{H^+}|_{\bar{y}=-1+\bar{d}}}, \quad (6.30)$$

where all the variables are defined in eq.(6.20). Finally, the equilibrium dimensionless brush height $\bar{d} = d/h$ can be determined by minimizing eq. (6.30) with respect to \bar{d} .

This minimization is carried out numerically.

Here too this brush height d (or \bar{d} in dimensionless form) will be compared with the brush height (d_0) for an uncharged polymer brush [see eq.(6.7)].

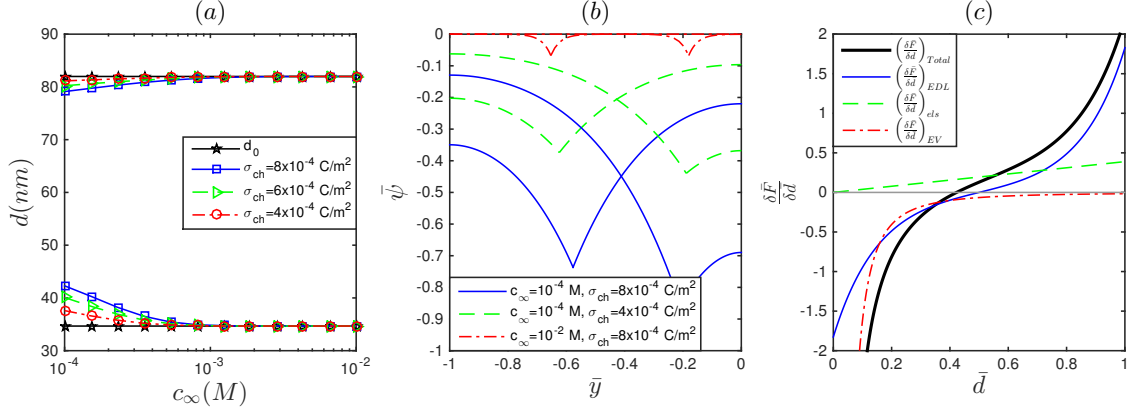


Figure 6.2: (a) Variation of the brush height d_0 (brush height without the electrostatic effects) and d (brush height with electrostatic effects) with electrolyte ion concentration (c_∞) for different values of PE brush end charge density (σ_{ch}) for nanoconfined weakly end-charged, pH-non-responsive PE brushes. Results are shown corresponding to two different (constant) values of d_0 ; for one value, $d_0 < h/2$ (for this case $\ell = 80$ nm, where ℓ is the distance of separation between grafted PEs) while for the other value, $d_0 > h/2$ (for this case $\ell = 22$ nm). (b) Transverse variation of the dimensionless electrostatic potential [$\bar{\psi} = e\psi/(k_B T)$] for different combinations of c_∞ and σ values for $d_0 < h/2$ and $\ell = 80$ nm (plots that show change in sign of the slope for \bar{y} values such that $-1 < \bar{y} < -0.5$) as well as for $d_0 > h/2$ and $\ell = 22$ nm (plots that show change in sign of the slope for \bar{y} values such that $-0.5 < \bar{y} < 0$). Although we provide the variation of $\bar{\psi}$ for these chosen combinations of c_∞ , σ and d_0 , we have checked and ensured that $|\bar{\psi}| < 1$ for the entire parameter space studied in (a). (c) Variation of $\delta \bar{F}/\delta \bar{d}$ and its different components with bar \bar{d} . Parameters for (c) are $c_\infty = 10^{-4}$ M, $\sigma_{ch} = 8 \times 10^{-4}$ C/m², $d_0 < h/2$ and $\ell = 80$ nm. The point where $\delta \bar{F}/\delta \bar{d}$ crosses the \bar{d} axis from negative to positive value denotes the equilibrium \bar{d} . Other parameters used in (a)-(c) are $h = 100$ nm, $N_p = 2000$, $a_k = 1$ nm, and $\chi = 0.4$.

6.3 Results and Discussions

6.3.1 Current understanding on the salt-dependent height variation of PE brushes

Before embarking on the results for the variation of the height of end-charged PE brushes, we shall first like to discuss the salt-dependent variation of height of the PE brushes containing charges along their entire backbone. Virtually all the studies on quantification of PE brush height have been performed with such brushes [104–113] – therefore, analyzing these results first will provide a useful platform to pinpoint the key non-trivialities associated with the height variation of the end-charged brushes. Scaling theories and more rigorous mean field based calculations as well as experiments have predicted that with an increase in the salt concentration the brush height decreases (except for very low salt concentration). Physically such a behavior has been attributed to the fact that at larger salt concentration (or smaller EDL thickness) the repulsive forces between the adjacent monomers of a particular brush is screened over much smaller distances (since the EDL thickness becomes small) – the consequent lowering of the repulsive interactions ensure that the brushes get shrunked with an increase in salt concentration. For exactly the same reason (i.e., the electrostatic repulsion between the monomers of a charged brush), one should expect that the presence of charges on the brushes will lead to a swelling as compared to the case of charge-free brushes – therefore, this swelling should be least at large salt concentration when the screening occurs over much smaller distances, thereby justifying the

lowering of brush height with a rise in salt concentration.

6.3.2 Configuration and electrostatics for weakly-end-charged, pH-non-responsive PE brushes

Here we first discuss the results for the weakly end-charged (amenable to the treatment based on Hebye-Hückel linearization), pH-non-responsive PE brushes. Fig. 6.2(a) shows the effect of the charge density of the end-charged PE brush (σ_{ch}), the electrolyte salt concentration (c_∞), and the confinement effect on the swelling and the shrinking of the PE brush. This is one of the central results of this chapter elucidating the charge effects on the configuration of the nanoconfined end-charged PE brushes. We consider two different values of the uncharged polymer brush height d_0 [see eq.(6.7)] – this value of d_0 dictates the degree of confinement, as discussed below. Specification of d_0 (or $\bar{d}_0 = d_0/h$) specifies the parameters [e.g., ℓ , h , a_k , and χ , or equivalently, α and β , given that $\bar{d}_0 = N_p(\beta/\alpha)^{1/3}$] that dictate the elastic and the excluded volume effects of the PE brush. Depending on the value of d_0 , we find, most remarkably, that the PE-end-charge-induced electrostatic effects may swell or shrink the PE brush. The shrinking (i.e., $d < d_0$, note we use the notations $d_{eq,PE}$ and d interchangeably) occurs if $d_0 > h/2$ (h is the nanochannel half height), while the swelling ($d > d_0$) occurs for $d_0 < h/2$. Here we consider the case of $d_0 < h/2$ as the one where the confinement effect is much less important, given that the grafted PE brushes on the two walls are too far apart from each other to interact. On the other hand, $d_0 > h/2$ represents the case where the brushes are close enough to

interact, thereby ensuring that the confinement effects become important. Under these conditions, we can infer that for the case where the confinement effects are not important electrostatic effects enhance the height of end-charged brushes, whereas when confinement effects become significant one witnesses an opposite trend, i.e., the electrostatic effects make the brushes shrink. For the case of the brushes with charges along the entire backbone, the electrostatic effects (regardless of the value of d_0/h) invariably increase the brush height as compared to the case of uncharged brushes on account of the repulsive interactions between the charged monomers – in this light, such confinement dependent switching of the role of the electrostatic effects in dictating swelling or shrinking of end-charged brushes is a highly non-trivial finding. We provide a free energy based argument to explain this behavior for the pH-non-responsive end-charged brushes. In Fig. 6.2(c), we plot the contribution of $\delta\bar{F}/\delta\bar{d}$ due to the different effects (elastic, excluded volume, and EDL). The equilibrium \bar{d} is provided by the \bar{d} value at which $\delta\bar{F}/\delta\bar{d}$ crosses the \bar{d} axis from negative to positive value (since for that case $\delta^2\bar{F}/\delta\bar{d}^2 > 0$, and the energy is minimized). We observe $\delta\bar{F}_{EDL}/\delta\bar{d} < 0$ for $\bar{d} < 0.5$ and $\delta\bar{F}_{EDL}/\delta\bar{d} > 0$ for $\bar{d} > 0.5$. Given that $\delta\bar{F}_{els}/\delta\bar{d} > 0$ and $\delta\bar{F}_{EV}/\delta\bar{d} < 0$ always, from such a variation of $\delta\bar{F}_{EDL}/\delta\bar{d}$ it is easy to infer the role of the electrostatics in swelling (for $\bar{d}_0 < 0.5$) and shrinking (for $\bar{d}_0 > 0.5$) the brushes. An even more elegant analysis can be provided by the corresponding variation of the total electrostatic energy, as shown in Fig. 6.3. For $\bar{d} < 0.5$, increase in \bar{d} decreases the net energy. This will ensure that for such cases, a larger value of \bar{d} will be preferred, signalling an increase in the brush height with the electrostatic effects. Similarly, for $\bar{d} > 0.5$, a decrease in \bar{d} decreases the net electrostatic energy ensuring that a smaller

value of \bar{d} will result due to the electrostatic effects.

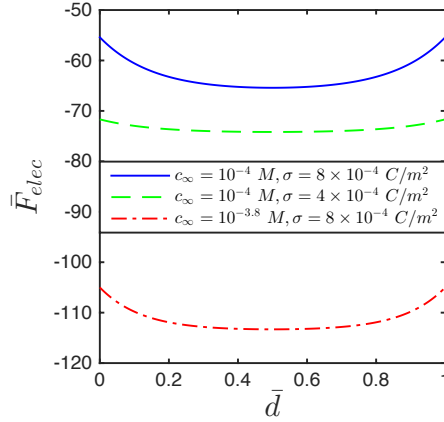


Figure 6.3: Dimensionless PE brush height (\bar{d}) dependent variation of the electrostatic energy \bar{F}_{elec} for different values of c_∞ and σ_{ch} . Parameters are identical to those used for Fig. 6.2(c).

Fig. 6.2(a) also shows that an enhanced value of the charge density σ_{ch} enhances the difference between d and d_0 for a given concentration – this implies that at larger σ_{ch} the brush exhibits an enhanced electrostatic-effect-induced shrinking (swelling) for $d_0 > h/2$ ($d_0 < h/2$). Such a behaviour can be trivially inferred from the fact that a larger σ_{ch} will lead to a more electrostatic effects.

Fig. 6.2(a) also demonstrates that weaker salt concentration leads to a much enhanced difference between d_0 and d , indicating a more dominant EDL effect. The consequence is that \bar{d} increases with the salt concentration for $d_0 > h/2$ (corresponding to which d is less than d_0) and decreases with the salt concentration for $d_0 < h/2$ (corresponding to which d is more than d_0). This is an extremely important finding of our paper in the light of the fact that for the PE brushes with backbone charging one

invariably witnesses, regardless of the value of d_0/h , a decrease in the brush height with an increase in salt concentration (except at very low salt concentration).

To summarize, Fig. 6.2(a) establishes that a hitherto unrevealed interplay between the confinement and the electrostatic effects ensure that the variation of the height of the end-charged brushes are different from that of the most-studied standard case of the PE brushes with backbone charging on three different aspects. These aspects are: *(a) for end-charged brushes, there is a distinct role of the confinement effect (i.e., whether $d_0 < h/2$ or $d_0 > h/2$) in dictating the brush height, (b) for end-charged brushes, for $d_0 > h/2$ we witness that electrostatic effects shrink the brushes, while for backbone-charged brushes the electrostatic effects always swell the brushes, and (c) for end-charged brushes, for $d_0 > h/2$ the brushes swell with an increase in salt concentration, while for backbone-charged brushes the trend has always been found to be reverse.*

It is worthwhile to note that our choices of the system parameters (e.g., grafting density and the polymer size) are such that the grafted PE molecules always attain a brush configuration and even for the case when $d > d_0$, d is always less than the channel half height h . Our proposed theory will fail for the case where $d > h$, since we do not account for interactions associated with the penetration and the interdigitation of the brush layers [116, 117]. Also note that since we work in the Debye-Hückel linearization regime, we make sure that the magnitude of the EDL potential $|\bar{\psi}|$ is always less than unity in the entire nanochannel. In Fig. 6.2(b), we provide sample results for the variation of $\bar{\psi}$ with \bar{y} for four different sets of parameters; we always find $|\bar{\psi}| < 1$. In fact, we have checked and ensured that $|\bar{\psi}| < 1$ for all the different

parameter combination that are studied in Fig. 6.2(a).

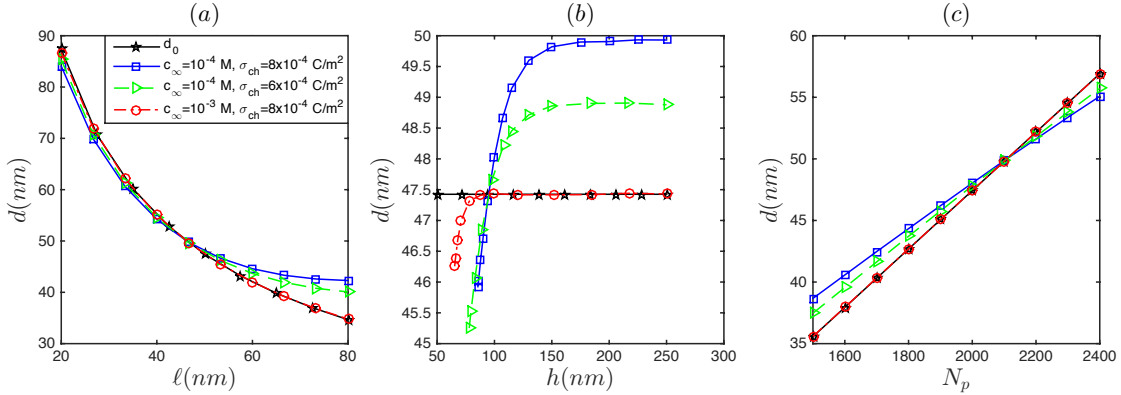


Figure 6.4: Variation of the brush height d_0 (brush height without the electrostatic effects) and d (brush height with electrostatic effects) with (a) ℓ or the distance of separation between adjacent grafted PE brushes (for this case, $h = 100$ nm, $N_p = 2000$, $a_k = 1$ nm and $\chi = 0.4$), (b) h or nanochannel half height (for this case $\ell = 50$ nm, $N_p = 2000$, $a_k = 1$ nm and $\chi = 0.4$), and (c) N_p or PE size (here $h = 100$ nm, $\ell = 50$ nm, $a_k = 1$ nm and $\chi = 0.4$). For each of (a)-(c), variation of d is shown for different values of PE brush end charge density (σ_{ch}) and electrolyte concentration (c_∞). The figure is for nanoconfined, weakly end-charged, pH-non-responsive PE brushes.

In Figs. 6.4(a-c), we showcase the influence of the electrostatic effects in dictating the end-charged PE brush height for different combinations of the system parameters. All the results, most remarkably, can be explained by noting that for $d_0 > h/2$, $d < d_0$ (i.e., electrostatics effects shrink the nanoconfined brush), whereas for $d_0 < h/2$, $d > d_0$ (i.e., the electrostatic effects swell the nanoconfined brushes). For example, Fig. 6.4(a) shows the influence of the spacing ℓ between the grafted

PE brushes. Smaller spacing (or larger grafting density) leads to a larger value of the brush height for both the charged and uncharged brushes. In Fig. 6.4(a), the nanochannel half height is $h = 100 \text{ nm}$. Therefore, for ℓ (typically smaller values of ℓ) for which $d_0 > h/2$, electrostatic effects ensure that $d < d_0$. On the contrary, for ℓ (typically larger values of ℓ) for which $d_0 < h/2$, electrostatic effects ensure $d > d_0$. Fig. 6.4(b) demonstrates the impact of the nanochannel half height h on the height of the nanoconfined brushes. Variation of h does not alter d_0 ; however, it changes the EDL-induced electrostatic effects. For small enough h value, $d_0 > h/2$, and hence the electrostatic effects ensure $d > d_0$. On the other hand, when h becomes large enough to ensure $d_0 < h/2$, we witness $d > d_0$. Fig. 6.4(c) shows the influence of N_p on the relative variation of d and d_0 . d_0 varies linearly with N_p [see eq.(6.7)]. For this plot h is fixed at 100 nm. Therefore, for small enough N_p for which $d_0 < h/2$, electrostatic effects ensure $d > d_0$. On the other hand, for large N_p for which $d_0 > h/2$, we encounter $d < d_0$. For all these three cases [Figs 6.4(a-c)], we find that the weakened salt concentration and the enhanced surface charge density increase this difference between d_0 and d for either of the two situations ($d_0 > h/2$ and $d_0 < h/2$).

6.3.3 Configuration and electrostatics for end-charged, pH-responsive PE brushes

In Fig. 6.5, we show the combined influence of the pH and the salt concentration on the configuration and the EDL electrostatics for nanoconfined end-charged, pH-responsive PE-brushes for $d_0 < h/2$. Fig. 6.5(a) shows the variation of the height of

the end-charged brushes. Since $d_0 < h/2$, following the results for pH-non-responsive brushes (see above), we expect a decrease in the brush height for an increase in the salt concentration. In Fig. 6.5(a), we indeed observe such a decrease in the brush height with salt concentration for higher ranges of salt concentration values. However, for smaller concentration the brush height actually increases with an increase in salt concentration. Importantly, such distinct salt-dependence of brush height is witnessed only for large pH. Larger pH or smaller values of H^+ ion concentration implies a more pronounced ionization of the charge-producing group at the end of the PE brush. In fact for $pH \gg pK_a$, one will witness a complete dissociation of this charge-producing group leading to a maximum value of the charge density (i.e., $\sigma_{ch,pH} \approx \sigma_{ch}$). Consequently, the electrostatic energy has a much larger magnitude for larger pH, leading to such distinct salt-induced alteration of the brush height. Of course, regardless of the salt concentration or pH, the brush height is always more than the corresponding uncharged brush height d_0 (except for very small concentration and very large pH). This non-monotonic (with respect to salt concentration) variation of the brush height for large pH is indeed extremely non-trivial given that weakly end-charged, pH-non-responsive PE brushes demonstrate a monotonic decrease in the brush height with salt concentration for $d_0 < h/2$ [see Fig. 6.2(a)]. The reason for which such non-monotonic behavior did not appear in Fig. 6.2(a) is that we did not investigate for small enough concentrations [since for such concentration values, Debye-Hückel linearization approximation got violated and our analysis for the pH-non-responsive end-charged brushes (see above) was based on this approximation]. This non-monotonicity for the pH-responsive brushes revealed here can be justified

from the corresponding total dimensionless electrostatic energy ($\bar{F}_{elec} = \bar{F}_{B,elec} + \bar{F}_{EDL}$) values. As shown in Fig. 6.6, the variation of \bar{F}_{elec} with respect to d attains a minimum for an intermediate salt concentration. As a consequence, the brush height is largest (or equivalently, there is a maximum difference between the charged and uncharged brush heights) at an intermediate salt concentration, while at very large and very small salt concentration this difference between the charged and uncharged brush heights is much less leading to a much smaller brush height. This explains why one witnesses a non-monotonic variation of the brush height with respect to the salt concentration at a large pH (i.e., the pH corresponding to which there is maximum ionization of the charge producing end group of the PE brush). On the other hand, when pH is very small or hydrogen ion concentration is very large, this ionization is tremendously hindered leading to a very small value of the charge density. As a consequence, the EDL effects are substantially reduced leading to very weak (or no) variation of the brush height with salt concentration [see the plot corresponding to $pH = 3, 4$ in Fig. 6.5(a)].

Fig. 6.5(b) provides the variation of $\bar{\psi}$ with \bar{y} for different combinations of c_∞ and pH . The magnitude of ψ is dictated by the corresponding value of the brush height. For larger brush height, typically witnessed for a given c_∞ but higher pH or a given pH and an intermediate (not too large or not too small) value of c_∞ , the brush occupies larger transverse sections of the nanochannel, leading to a larger value of $\bar{\psi}$ at a given \bar{y} . This is evident for $\bar{\psi}$ values corresponding to $c_\infty = 10^{-4} m$, $pH = 6$ and $c_\infty = 10^{-5} M$, $pH = 6$.

In Fig. 6.7, we study the brush height and electrostatics for pH-responsive

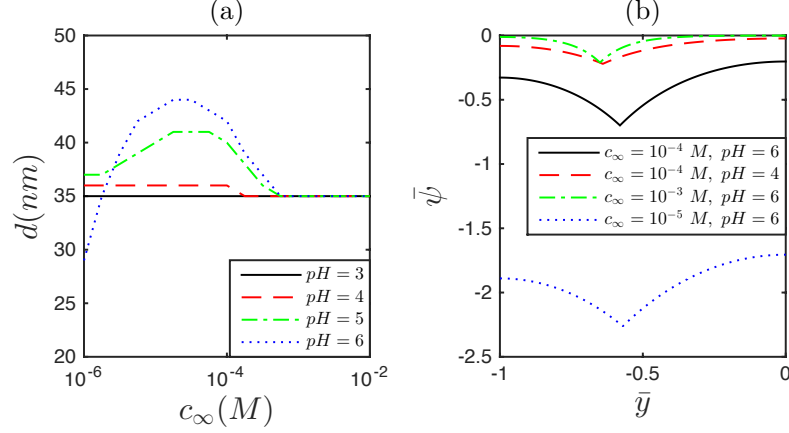


Figure 6.5: *Case for $d_0 < h/2$ for nanoconfined, end-charged, pH-responsive PE brushes:* (a) Variation of the brush height with salt concentration and pH. (b) Transverse variation of the dimensionless electrostatic potential ($\bar{\psi}$) for different combinations of salt concentration and pH. Parameters used for these plots are $N_p = 2000$, $\ell = 80$ nm, $\sigma_{ch} = -0.0008C/m^2$, $d_0 = 34$ nm, $pK_a = 4$, $h = 100$ nm, $\chi = 0.4$, $a_k = 1$ nm, $k_B = 1.38 \times 10^{-23}$ J/K, $T = 300$ K, $e = 1.6 \times 10^{-19}$ C, $\epsilon_0 = 8.8 \times 10^{-12}$ F/m, $\epsilon_r = 79.8$.

brushes for the case $d_0 > h/2$. Here, we find that the EDL effects always decrease the brush height as compared to the uncharged brushes [see Fig. 6.7(a)] (except for very large pH and very small salt concentration). For $d_0 > h/2$, such a decrease in the brush height with respect to d_0 has also been witnessed for the pH-non-responsive brushes [see Fig. 6.2(a)]. Again, these pH-responsive brushes demonstrate an increase (decrease) in the height with an increase in the salt concentration for larger (smaller) values of the salt concentration [see 6.7(a)]. Calculations for pH-non-responsive brushes have identified the variation for larger salt concentration, but not

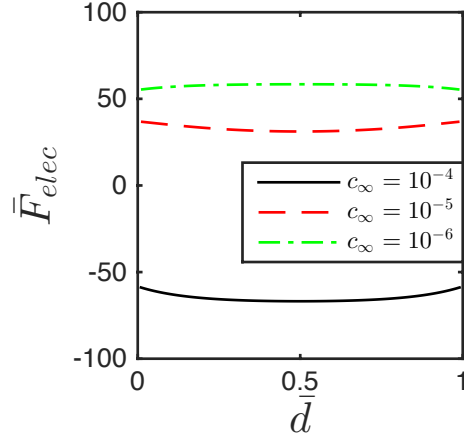


Figure 6.6: Variation of $\bar{F}_{elec} = \bar{F}_{B,elec} + \bar{F}_{EDL}$ with \bar{d} for different salt concentrations (expressed in M). The result is shown for $pH = 6$. All other parameters are identical to that used in Fig. 6.5.

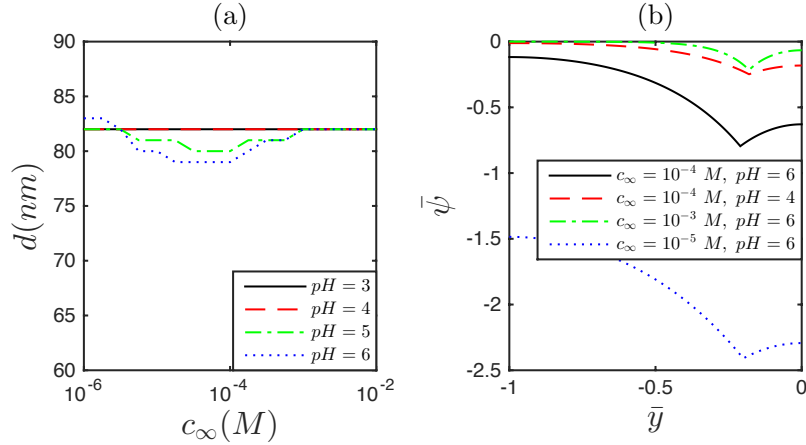


Figure 6.7: Case for $d_0 > h/2$ for nanoconfined, end-charged, pH -responsive PE brushes: (a) Variation of the brush height with salt concentration and pH . (b) Transverse variation of the dimensionless electrostatic potential ($\bar{\psi}$) for different combinations of salt concentration and pH . Parameters used for these plots are $\ell = 22$ nm and $d_0 = 82$ nm. All other parameters are identical to that used in Fig. 6.5.

for smaller salt concentration [see Fig. 6.2(a)]. Like the case of $d_0 < h/2$, here too the \bar{F}_{elec} is minimum for an intermediate \bar{d} (results not shown). As a consequence, the electrostatic-effect-mediated difference between the charged and uncharged brush heights is maximum for the intermediate salt concentration. Consequently, we find this non-monotonic variation of the brush height with salt concentration – it first decreases with the salt concentration, attains a minimum, and then increases with the salt concentration. Again, here too the maximum difference between the charged and the uncharged brush heights is witnessed for a large pH, where the ionization of the charge-producing end-group is maximum. An important issue here is that the difference between the charged (d) and uncharged (d_0) brush heights are extremely small, although we always have $d < d_0$ (except for very small concentration and very large pH). In Fig. 6.7(b), we show the corresponding transverse variation of the dimensionless electrostatic $\bar{\psi}$ for different combinations of pH and salt concentration. Given that the brush height variation between the different cases (corresponding to different combination of pH and salt concentration values) is very small, the electrostatic potential has very little dependence on the brush height. Consequently, the salt concentration and pH entirely dictate $\bar{\psi}$, leading to enhanced $\bar{\psi}$ for the case where the EDL is thicker or the screening is weaker. Consequently, $\bar{\psi}$ is maximum for the case that leads to minimum ion concentration or the largest EDL thickness ($c_\infty = 10^{-5} M$, $pH = 6$) and minimum for the case that leads to maximum ion concentration or the smallest EDL thickness ($c_\infty = 10^{-4} M$, $pH = 5$).

6.4 Conclusions

We showcase here the role of confinement in dictating the height of the end-charged PE brushes for both pH-non-responsive and pH-responsive brushes. These brushes are grafted on the inner walls of a nanochannel, and the enhancement (decrement) of the degree of confinement ensures that the electrostatic effect leads to a shrinking (swelling) of the PE brushes (as compared to the uncharged brushes). More importantly, we witness that the increase in salt concentration may either increase or decrease the brush height depending on the degree of confinement and the pH-responsiveness (or the lack of it) of the brushes. Such behaviors are attributed entirely to the interplay of the confinement and the electrostatic effects; in fact, understanding of such distinct impact of the confinement on the thermodynamics and structure of the PE brushes has been hitherto missing. The results are specially non-trivial when compared to the results for the case where the brushes contain charges along their entire backbone and demonstrate an inevitable lowering of the brush height on increase in salt concentration. Shedding light on such behaviors of the PE brushes will be vitally important for a more controlled PE-grafting-based functionalization of the nanochannels for applications ranging from biosensing and ion manipulation to current rectification and flow valving.

6.5 Appendix: Derivation of eq.(6.12)

Eq.(6.12) is derived by minimizing the overall free energy [see eq.(6.1)] with respect to ψ_s :

$$\begin{aligned}
\frac{\delta F}{\delta \psi_s} &= 0 \\
\Rightarrow \frac{\delta}{\delta \psi_s} \left[\int f_{EDL}(\psi, \psi', n_{\pm}) d^3 \mathbf{r} \right] + \frac{\delta}{\delta \psi_s} \left[\delta(y+h-d) \int \sigma_{ch} \psi_s d^2 \mathbf{r} \right] &= 0 \\
\Rightarrow \frac{\delta}{\delta \psi_s} \left[\int -\frac{\epsilon_0 \epsilon_r}{2} \left| \frac{d\psi}{dy} \right|^2 d^3 \mathbf{r} \right] + \frac{\delta}{\delta \psi_s} \left[\int \sigma_{ch} \psi_s d^2 \mathbf{r} \right] &= 0.
\end{aligned} \tag{6.31}$$

Let us define

$$\frac{d\phi}{dy} = \left(\frac{d\psi}{dy} \right)^2, \tag{6.32}$$

and similarly

$$\frac{d\phi_s}{dy} = \left(\frac{d\psi_s}{dy} \right)^2. \tag{6.33}$$

Consequently, employing divergence theorem, we may write:

$$\begin{aligned}
-\int \frac{\epsilon_0 \epsilon_r}{2} \left| \frac{d\psi}{dy} \right|^2 d^3 \mathbf{r} &= -\frac{\epsilon_0 \epsilon_r}{2} \int \left(\frac{d\phi}{dy} \right) d^3 \mathbf{r} \\
&= -\frac{\epsilon_0 \epsilon_r}{2} \int \phi_s d^2 \mathbf{r}
\end{aligned} \tag{6.34}$$

Using eq.(6.34) in eq.(6.31), we can write:

$$\frac{\delta F}{\delta \psi_s} = 0 \Rightarrow \frac{\delta}{\delta \psi_s} \int \left[-\frac{\epsilon_0 \epsilon_r}{2} \phi_s + \sigma_{ch} \psi_s \right] d^2 \mathbf{r} = 0. \tag{6.35}$$

Eq.(6.35) implies

$$\begin{aligned}
& \frac{\delta}{\delta\psi_s} \left[-\frac{\epsilon_0\epsilon_r}{2}\phi_s + \sigma_{ch}\psi_s \right] = 0 \\
& \Rightarrow -\frac{\epsilon_0\epsilon_r}{2} \frac{\partial\phi_s}{\partial\psi_s} + \frac{\epsilon_0\epsilon_r}{2} \frac{d}{dy} \left(\frac{\partial\phi_s}{\partial\psi'_s} \right) + \sigma_{ch} = 0 \\
& \Rightarrow \frac{\epsilon_0\epsilon_r}{2} \frac{\partial}{\partial\psi'_s} \left(\frac{d\phi_s}{dy} \right) + \sigma_{ch} = 0 \\
& \Rightarrow \frac{\epsilon_0\epsilon_r}{2} \frac{\partial}{\partial\psi'_s} (\psi_s'^2) + \sigma_{ch} = 0 \\
& \Rightarrow \psi'_s = -\frac{\sigma_{ch}}{\epsilon_0\epsilon_r}
\end{aligned} \tag{6.36}$$

Consequently, we can write:

$$\left(\frac{d\psi}{dy} \right)_{y=(-h+d)^+} - \left(\frac{d\psi}{dy} \right)_{y=(-h+d)^-} = -\frac{\sigma_{ch}}{\epsilon_0\epsilon_r}, \tag{6.37}$$

i.e., we recover eq.(6.12)

Chapter 7: Ionic current in nanochannels grafted with end-charged, pH-responsive polyelectrolyte brushes described in the coupled regime

In this chapter¹, calculations are provided to quantify the ionic current in nanochannels grafted with end-charged, pH-responsive PE brushes, with the brushes being modeled in the coupled regime. Therefore, this is possibly the first attempt to study the electrokinetics (ionic current) in a soft nanochannel, where the functionalizing brushes have been modelled in a self-consistent fashion. We witness that the ionic current for smaller pH is much larger despite the corresponding magnitude of the EDL electrostatic potential being much smaller – this stems from the presence of a much larger concentration of H^+ ions at small pH and the fact that H^+ ions have very large mobilities. In fact, this ionic current shows a steep variation with pH that can be useful in exploring new designs for applications involving quantification and characterization of ionic current in PE-brush-grafted nanochannels.

¹Contents of this chapter have been published as *G. Chen and S. Das, Thermodynamics, electrostatics, and ionic current in nanochannels grafted with pH-responsive end-charged polyelectrolyte brushes. Electrophoresis, DOI: 10.1002/elps.201600415 (2016).*

7.1 Introduction

Quantification of the ionic current in PE-brush-functionalized nanochannels is central to ensure successful uses of such nanochannels for applications such as biosensing, analyte sensing, current rectification, diodic action, flow control, etc. In this chapter, we quantify the ionic current in a nanochannel grafted with end-charged, pH responsive PE brushes with the brushes being described in a thermodynamically self-consistent fashion (i.e., the excluded volume and elastic effects of the brushes are considered along with the electrostatic effects of the brushes and the EDL in order to quantify the equilibrium configuration of the brushes). We use the thermodynamic model for the pH-responsive, nanoconfined, end-charged brushes developed in Chapter 6 for the present calculation. While ionic current has been previously studied in PE-brush-grafted nanochannels theoretically [8, 52], this is for the first time a theoretical model on ionic current in PE-brush-grafted nanochannels, appropriately accounting for the PE configuration and thermodynamics, has been developed. The key result is a most remarkable enhancement of ionic current for smaller pH, despite a smaller magnitude of EDL potential at such pH values. We explain such a finding on account of the corresponding large concentration of H^+ ions at small pH and the fact that H^+ ions have very large mobility values. Overall, our theoretical study probes a hitherto unravelled electrokinetics that we believe have the potential to help design nanoscale PE brush based systems with a potential of plethora of applications.

7.2 Calculation of the Ionic Current

Here we consider the generation of the ionic current in presence of an externally applied axial electric field in a nanochannel grafted with pH-responsive, end-charged PE brushes (i.e., the system represented in Fig. 6.1). We quantify the ionic current in this pH-responsive end-charged-brush-grafted nanochannels. The ionic current is ensued due to the EDLs developed around the charged PE brushes and within the electrolyte. In this study, the specifics of the brush configuration in calculation of this EDL has been quantified – accordingly, this study can be considered to be the first study delineating the effect of the PE brush configuration in the calculation of the soft nanochannel (nanochannel grafted with PE brushes) ionic current. We can express this ionic current (i_{ion}) per unit width (having units of A/m) as:

$$i_{ion} = eE \int_{-h}^h \left(\sum_i \mu_i n_i \right) dy, \quad (7.1)$$

where E is the applied axial electric field, μ_i is the unsigned electrophoretic mobility of species i (where $i = \pm, H^+$ and OH^-), and n_i are the ionic number densities.

Using the expressions provided in Chapter 6 for n_i and $n_{i,\infty}$, we may re-write eq.(7.1) as:

$$i_{ion} = 2eEn_{\infty}h \int_{-1}^0 \left[\mu_+ \exp(-\bar{\psi}) + \mu_- (1 + \bar{n}_{H^+, \infty}) \exp(\bar{\psi}) \right] + 2eEn_{\infty}h \int_{-1}^0 \left[\mu_{H^+} \bar{n}_{H^+, \infty} \exp(-\bar{\psi}) + \mu_{OH^-} \bar{n}_{OH^-, \infty} \exp(\bar{\psi}) \right] d\bar{y}. \quad (7.2)$$

7.3 Results

Fig. 7.1 provides the variation of the ionic current per unit applied axial electric field (i_{ion}/E) for the nanochannels grafted with the end-charged, pH-responsive PE brushes for the case where $d_0 < h/2$. Despite the electrostatic potential being smaller (in magnitude) for smaller pH [see Fig. 6.5(b)], we witness a much larger current for smaller pH. For nanofluidic systems, the ionic current is typically a strong function of the EDL ionic current (the ionic current is typically the sum of the EDL ionic current and the bulk ionic current [8]), which in turn is enhanced by the larger electrostatic potential. Therefore, this result where we witness that for larger pH the ionic current is getting reduced despite the electrostatic potential getting enhanced is a highly non-trivial result in context of nanochannel ionic current generation. The reason for such a non-trivial occurrence is the fact that smaller pH implies large concentration of H^+ ions that have significantly larger mobility values (as compared to other ions in the system) due to their small sizes. This combination of larger H^+ ion concentration and its large mobility value ensure a much larger ionic current for smaller pH, despite the corresponding electrostatic potential being small. This same enhanced ionic current is also witnessed, most intuitively, for enhanced salt concentration. Study of this interplay of salt concentration and pH on the ionic current in the end-charged PE-grafted nanochannels is the main important finding of this chapter. In fact, to the best of our knowledge, this is the first study that accounts for the specifics of the PE-brush configuration (rather than assuming it of constant, salt-independent thickness) in the evaluation of the ionic current in the PE-brush-grafted nanochannels.

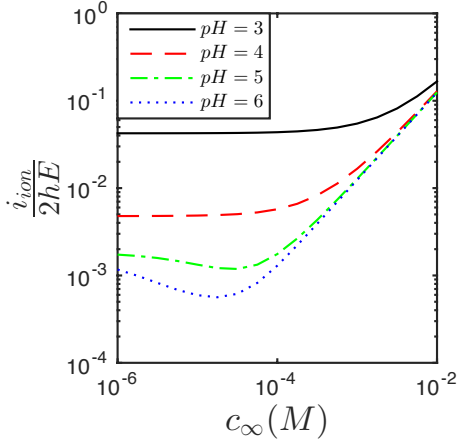


Figure 7.1: Salt-concentration and pH induced variation of the ionic current [in $A/(Vm)$ or S/m] per unit nanochannel cross sectional area per unit applied axial electric field in nanochannels grafted with end-charged and pH-responsive PE brush for the case where $d_0 < h/2$. Parameters used for these plots are $N_p = 2000$, $\ell = 80 \text{ nm}$, $\sigma_{ch} = -0.0008C/m^2$, $d_0 = 29 \text{ nm}$, $pK_a = 4$, $h = 100 \text{ nm}$, $\chi = 0.4$, $a_k = 1 \text{ nm}$, $k_B = 1.38 \times 10^{-23} \text{ J/K}$, $T = 300 \text{ K}$, $e = 1.6 \times 10^{-19} \text{ C}$, $\epsilon_0 = 8.8 \times 10^{-12} \text{ F/m}$, $\epsilon_r = 79.8$.

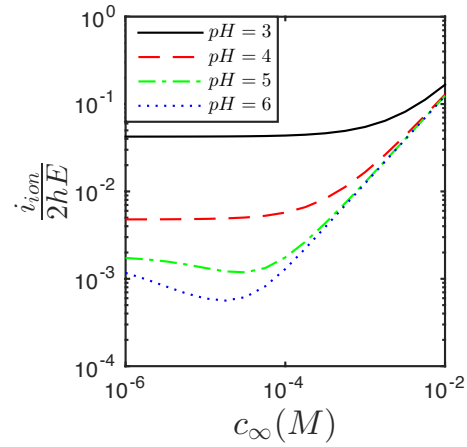


Figure 7.2: Salt-concentration and pH induced variation of the ionic current [in $A/(Vm)$ or S/m] per unit nanochannel cross sectional area per unit applied axial electric field in nanochannels grafted with end-charged and pH-responsive PE brush for the case where $d_0 > h/2$. Parameters used for these plots are $\ell = 15 \text{ nm}$ and $d_0 = 88.2 \text{ nm}$. All other parameters are identical to that used in Fig. 7.1.

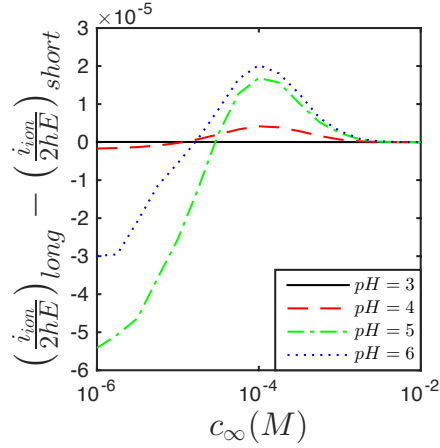


Figure 7.3: Difference in the ionic current (per unit width of the nanochannel per unit applied electric field) between the taller (case studied in Fig. 7.2) and the shorter (case studied in Fig. 7.1) brushes. This difference in ionic current has units of $A/(Vm)$ or S/m .

In Fig. 7.2, we show the variation of the ionic current with c_∞ and pH for the nanochannels grafted with end-charged, pH-responsive PE brushes for the case where $d_0 > h/2$. We get very similar dependence on salt concentration and pH as witnessed for $d_0 < h/2$. The reason is that the ionic current is being dictated by the bulk values of the ion concentrations (salt and H^+) and the integral (across the entire nanochannel height) of the electrostatic potential values. Variation in the brush height triggers a variation in the electrostatic potential distribution [please compare Figs. 6.5(b) and 6.7(b)]; however, the integral of the potential remains almost similar. In Fig. 7.3, we show the distinctly small (but finite) difference in the ionic current between the two cases of $d_0 < h/2$ and $d_0 > h/2$.

7.4 Conclusions

In this chapter, we used the mean field model, developed to quantify the configuration and electrostatics of nanoconfined, end-charged, pH-responsive PE brushes, to estimate electrokinetics (in form of ionic current) in nanochannels grafted with such PE brushes. This is for the first time, the ionic current in a PE-brush-grafted nanochannel has been quantified through a model that appropriately accounts for the brush configuration and does not consider it to be of a constant electrostatic-independent value. We witness that the ionic current is much larger at smaller pH, despite a weaker magnitude of the electrostatic potential at that value. This stems from the large value of H^+ ion concentration at small pH and the fact that hydrogen ions have large mobilities due to their small sizes. To conclude, the present study has provided possibly the first continuum model of PE-brush-grafted nanochannel ionic current that describes the brushes thermodynamically consistently. Equally importantly, it will provide a basis for probing new designs of PE-brush-functionalized nanochannels for a myriad of applications involving ion migration and ion manipulation.

Measurement of ionic current and the corresponding $I - V$ response curve forms the foundation of a large number of applications involving PE-brush grafted nanochannels. For example, appropriate determination of $I - V$ response of a PE-brush grafted nanochannel in presence and in absence of an external ionic species allows sensing of that particular species (e.g., L-tryptophan [69], DNA oligomer [71], hydrogen peroxide [73], enantiomers [118], cysteine [119], Hg^{2+} ions [120], Ag^+ ions

[120], etc.). Very often such a response can be pH-sensitive [28, 73, 119, 120], given that this particular chemical moiety may have a pH-dependent ionization. Therefore, having a theoretical foundation for quantifying the pH-responsive ionic current in a PE-grafted nanochannel in a manner such that the specifics of the PE configuration is also accounted for in the ionic current calculation is central for designing a PE-grafted nanochannel as an efficient bioanalyte and ion sensing device. The present theoretical study does exactly that for a particular design of the PE-grafted nanochannels, where the PEs are end-charged. Another important application of such PE-grafted nanochannels has been ionic current rectification [28, 30]. Typically, such rectification implies that a given applied voltage will lead to a more enhanced (or a rectified) current. Often such rectification elements are PE-grafted *conical* nanochannels, just like the ion and bioanalyte sensing PE-grafted nanochannels. To the best of our knowledge, there exists no continuum theoretical framework that quantifies and therefore helps designing ionic current and current rectification in such conical PE-grafted nanochannels by appropriately accounting for the brush configurations. Our study, focusing on straight nanochannels, will provide important preliminary basis (given that all the equations will remain unchanged) for such a modelling.

Chapter 8: Massive enhancement of electroosmotic transport in nanochannels grafted with end-charged polyelectrolyte brushes

In this chapter¹, calculations are provided to establish that nanochannels grafted with pH-responsive, end-charged polyelectrolyte (PE) brushes demonstrate a massive augmentation in the strength of the electroosmotic (EOS) transport in presence of an external electric field. This contradicts the existing understanding that the electroosmotic transport is severely retarded in channels grafted with PE brushes due to the brush-induced enhanced drag force. We explain this EOS-flow-enhancement by noting that the *end-charged* PE brushes demonstrate a unique ability of localizing the maximum charge density of the electrolyte ions at the location of its end, i.e., far away from the grafting surface. As a result, the maximum driving force on the liquid can be at a location far away from the wall and hence the resulting local liquid velocity suffers very little retardation due to the wall shear stress. We anticipate that the present chapter will unravel a completely new paradigm in the application of functionalized interfaces in regulating nanofluidic transport.

¹Contents of this chapter will be submitted as *G. Chen and S. Das, Massive enhancement of electroosmotic transport in nanochannels grafted with end-charged polyelectrolyte brushes. Scientific Reports (2017).*

8.1 Introduction

It is a standard knowledge that nanochannels and microchannels grafted with PE brushes will invariably lower the flow strength (e.g., electric-field-driven electroosmotic or EOS flow) on account of an enhanced drag on the flow by the polymer molecules [26, 35, 84] and studies have proposed to use this flow-strength reduction for designing EOS flow suppressors [26, 84] that can be useful for a number of applications (e.g., bio-analyte sensing, current rectification, etc.) where appropriate and highly sensitive estimation of the ionic current becomes necessary.

In this study, we report our discovery of a completely opposite effect of PE-brush-grafted nanochannels on EOS transport – *we demonstrate that nanochannels grafted with PE-brushes containing charges only at their non-grafted ends may actually experience a massive augmentation in the strength of the EOS flow.* These end-charged PE brushes are characterized by density of their end charges (σ_{ch}) and have been used for a number of applications such as disassembling amyloid fibrils [7], targeted pH-responsive drug delivery [121], etc. We show that the EOS flow in a PE-brush-free nanochannel having the same surface charge density of σ_{ch} (at its rigid walls) is significantly weaker than the EOS flow in this end-charged PE-brush grafted nanochannels. We attribute this highly non-intuitive effect to the fact that the end-charged brushes allow a localization of the maximum charge density of the electrolyte ions (i.e., the maximum difference between the number densities of counterions and coions forming the electric double layer or EDL) at a location that is far from the grafting surface. As a consequence, the driving body force on the liquid, which is

proportional to the charge density of the electrolyte ions, can be highest or most concentrated at a location where the drag on the flow caused by the wall shear stress is very small. This in turn ensures a massive augmentation of the EOS flow strength. For charged nanochannels with no brushes, this maximum driving force (or equivalently, the maximum difference in the charge density) is at the wall where the no-slip condition retards the flow. On the other hand, for the PE brush with backbone charges, the body force is distributed within the brush height and therefore gets dispersed and does not remain localized away from the wall (unlike the end-charged PE brushes). As a consequence, impact of the EOS body force in driving the flow is somewhat reduced in both brush-free nanochannels and nanochannels grafted with backbone-charged brushes. This justifies this rather remarkable finding where the EOS flow gets enhanced in nanochannels functionalized by end-charged PE brushes.

In addition to discovering this highly non-trivial behavior of the PE-brush-grafted nanochannels in context of the EOS transport, the present chapter provides the first model that accounts for the thermodynamics and the configuration of the PE brushes in a mean field setting for modeling the EOS flow in the PE-grafted-nanochannels. There have been a considerable number of studies on EOS transport in PE-grafted nanochannels ranging from probing of the streaming current generation [35, 79, 122, 123] and suppressed EOS transport [26, 84] to quantifying the influence of the Donnan potential [53]. However, in all of these studies the height of the PE brush layer has been assumed to be constant with no dependence on the salt concentration or pH. On the contrary, in this present study we account for the effect of salt concentration and pH on the brush configuration by describing the brush

height explicitly as an interplay of the brush elastic, excluded volume, and electrostatic energies and the EDL energy. As a consequence, we embark upon a more complete model where the EOS transport depends not only on the EOS body force resulting from the ion concentrations but also the specificities (e.g., strength of the drag force, location of the end charge, etc.) associated with the ion concentration dictated brush height. The second critical issue is the description of the monomer distribution along the PE brush. While these monomers being uncharged (for the present problem) do not contribute to the overall electrostatics, they indeed dictate the drag coefficient that affects the EOS transport. Previous studies on fluid flow in PE brush grafted channels have considered uniform or parabolic or cubic monomer distribution [26, 53, 79, 122, 123]. For the present study, we shall simply consider a uniform monomer distribution that is equivalent to the consideration of the well-known monomer step profile proposed by Alexander [1] and de Gennes [2, 3]. The mean field model developed here, therefore, is coupled with the appropriate description of the fluid flow in order to propose the nanofluidic-transport-enhancing capabilities of the PE-brush-grafted nanochannels that can be extensively employed for engineering novel nanofluidic designs.

8.2 Calculation of the EOS Transport

The main purpose of this chapter is to study the EOS transport triggered in presence of an externally applied axial electric field in such pH-responsive, end-charged (with charge density σ_{ch}) PE-brush-grafted nanochannels [see Fig. 8.1(b)] and demon-

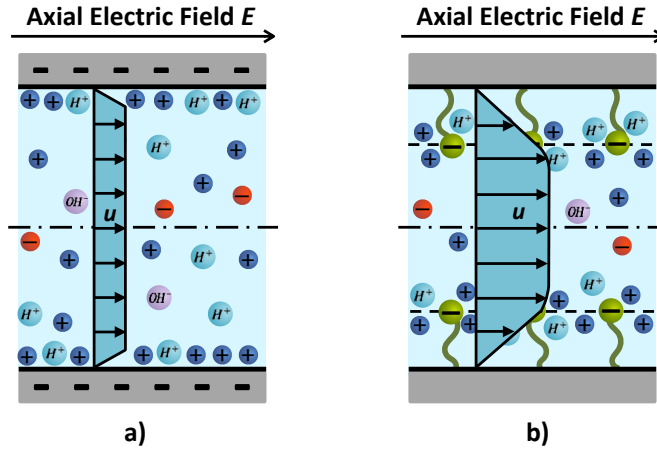


Figure 8.1: Schematic depicting the electroosmotic transport in (a) nanochannels free of PE brushes and (b) nanochannels grafted with end-charged PE brushes. The schematic categorically represents the enhancement of the strength of the EOS transport in nanochannels grafted with end-charged PE brushes.

strate that this EOS transport is significantly stronger than the EOS transport ensued in a brush-free nanochannel with a wall charge density of σ_{ch} [see Fig. 8.1(a)]. This EOS flow in either of the systems (with and without wall-grafted PE brushes) is triggered due to the interaction of the applied electric field E and the imbalance of the ionic number density within the EDL. For the nanochannel grafted with end-charged PE brushes, the thermodynamics discussed in Chapter 6 provides the EDL electrostatic potential and the resulting number densities of various ions, which would eventually provide this ionic number density within the EDL. Considering the EOS flow to be steady, hydrodynamically fully-developed, and uni-directional, we can express the governing equation dictating the flow as (considering the nanochannel bottom

half):

$$\begin{aligned} \eta \frac{d^2 u}{dy^2} + e(n_+ - n_- + n_{H^+} - n_{OH^-}) E - \frac{\eta}{k} u &= 0 \quad [\text{for } -h \leq y \leq -h + d], \\ \eta \frac{d^2 u}{dy^2} + e(n_+ - n_- + n_{H^+} - n_{OH^-}) E &= 0 \quad [\text{for } -h + d \leq y \leq 0], \end{aligned} \quad (8.1)$$

where u is the uni-directional velocity, η is the dynamic viscosity of the liquid, e is the electronic charge, n_i is the number density of the ionic species i , and $k = a_k^2 \left(\frac{d}{\sigma a_k^3 N_p \phi} \right)^2$ is the permeability and $\frac{\sigma a_k^3 N_p \phi}{d}$ is the volume fraction of the PE brush layer. For the present study, very much like Chapter 6 and 7, we consider a stepped profile of the end-charged PE brush – hence we have $\phi = 1$.

Using eq.(6.25) and expressing the bulk number densities of the ions in a manner identical to that in Chapter 6 [please see the discussion following eq.(6.26)], we can express eq.(8.1) in dimensionless form as

$$\begin{aligned} \frac{d^2 \bar{u}}{d\bar{y}^2} - \frac{\bar{E}}{2\bar{\lambda}^2} [-\exp(-\bar{\psi}) + (1 + \bar{n}_{H^+, \infty}) \exp(\bar{\psi}) - \bar{n}_{H^+, \infty} \exp(-\bar{\psi}) + \bar{n}_{OH^-, \infty} \exp(\bar{\psi})] \\ - \left(\frac{a_k^2 \sigma N_p \phi}{d} \right)^2 \bar{u} = 0 \quad [\text{for } -1 \leq \bar{y} \leq -1 + \bar{d}], \\ \frac{d^2 \bar{u}}{d\bar{y}^2} - \frac{\bar{E}}{2\bar{\lambda}^2} [-\exp(-\bar{\psi}) + (1 + \bar{n}_{H^+, \infty}) \exp(\bar{\psi}) - \bar{n}_{H^+, \infty} \exp(-\bar{\psi}) + \bar{n}_{OH^-, \infty} \exp(\bar{\psi})] \\ [\text{for } -1 + \bar{d} \leq \bar{y} \leq 0]. \end{aligned} \quad (8.2)$$

where $\bar{\psi} = e\psi/(k_B T)$, $\bar{u} = u/u_0$ (u_0 is the velocity scale), $\bar{E} = E/E_0$ (u_0 and E_0 are connected as $u_0 = \frac{k_B T}{e} \frac{\epsilon_0 \epsilon_r E_0}{\eta}$), $\bar{n}_{i, \infty} = n_{i, \infty}/n_\infty$, $\bar{y} = y/h$, $\bar{\lambda} = \lambda/h$ ($\lambda = \sqrt{\epsilon_0 \epsilon_r k_B T / (2n_\infty e^2)}$ is the EDL thickness), $\bar{d} = d/h$.

With the knowledge of the dimensionless EDL electrostatic potential $\bar{\psi}$ (see Chapter 6), eq. (8.2) is finally solved numerically in the presence of the following dimensionless

boundary conditions:

$$\begin{aligned} \left(\frac{d\bar{u}}{d\bar{y}}\right)_{\bar{y}=0} &= 0, \quad (\bar{u})_{\bar{y}=-1} = 0, \\ (\bar{u})_{\bar{y}=(-1+d)^-} &= (\bar{u})_{\bar{y}=(-1+d)^+}, \quad \left(\frac{d\bar{u}}{d\bar{y}}\right)_{\bar{y}=(-1+d)^-} = \left(\frac{d\bar{u}}{d\bar{y}}\right)_{\bar{y}=(-1+d)^+}. \end{aligned} \quad (8.3)$$

8.3 Results

8.3.1 Variation of the brush height

In chapter 6 as well our recent papers [124, 125], we have provided detailed analysis on the variation of the height of the nanoconfined, end-charged, pH-responsive PE brushes as a function of degree of confinement (or equivalently, short and tall brushes), pH and salt concentration. We do not repeat those results here, but rather simply summarize the key issues that will be needed to explain the subsequent results on the variation of the EDL electrostatics, ion concentration, and the EOS transport.

A key parameter that dictates the brush height is the degree of confinement, quantified by whether $d_0 < h/2$ (weak confinement) or $d_0 > h/2$ (strong confinement). Here d_0 refers to the height of the uncharged polymer brushes having identical elastic and excluded volume energies as the end-charged PE brushes. For brushes with $d_0 > h/2$, the electrostatic energy contributes to the lowering of the brush height d as compared to d_0 , while for brushes with $d_0 < h/2$, the electrostatic energy ensures that $d > d_0$. The electrostatic effects are maximum for largest pH ($=7$), for which the ionization of the end-charge-producing group is maximum. Consequently, at $pH = 7$ there is maximum difference between d and d_0 – this difference ensures that for a

given salt concentration d has the largest (smallest) value for $pH = 7$ for brushes with $d_0 < h/2$ ($d_0 > h/2$). For such large pH values, increase in salt concentration increases (decreases) the electrostatic free energy for small (large) values of salt concentration. Accordingly, we witness that d first decreases (increases), attains a minimum (maximum), and then increases (decreases) with the salt concentration for brushes with $d_0 > h/2$ ($d_0 < h/2$). It is worthwhile to mention here that the height d_0 of the uncharged brushes can be increased by either increasing the grafting density σ or the polymer size N_p [see eq.(6.7)]. Given that $d_0 \sim \sigma^{1/3}$ and $d_0 \sim N_p$, one will require a much larger (smaller) increase in σ (N_p) in order to ensure a given increase in the brush height. Of course, as will be explained later, the EOS transport in such end-charged PE brush grafted nanochannels will be severely affected depending on whether d_0 increased by increasing σ or by increasing N_p .

8.3.2 EDL electrostatic potential and the ion number density distribution

In Fig. 8.2, we study the transverse variation of the magnitude of the dimensionless EDL electrostatic potential [$|\bar{\psi}| = |e\psi/(k_B T)|$] (top panel) and the number densities of the counterions (n_+) (middle panel) and coions (n_-) (bottom panel). Significance of this figure is that it provides critical understanding about the electrostatics of the problem, which is central to correctly interpret the EOS flow fields. We study all the quantities ($\bar{\psi}$ and n_{\pm}) for $pH = 7$ for five different channel systems: a) nanochannels grafted with short-loose brushes ($N_p = 2000$, $\ell = 80$ nm,

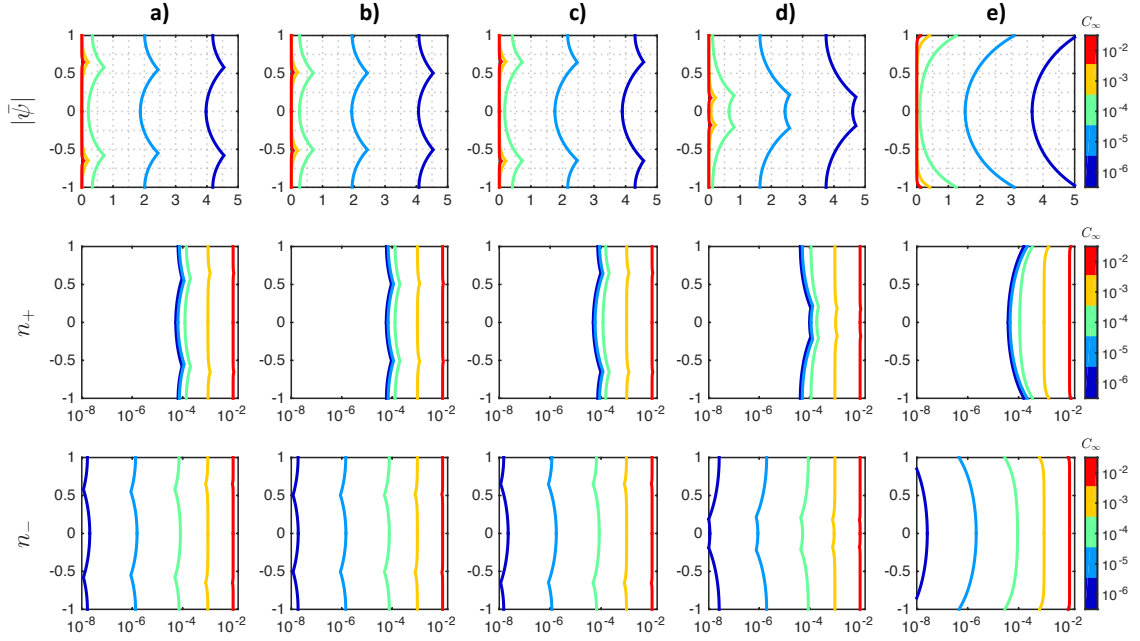


Figure 8.2: Variation of the magnitude of the dimensionless transverse EDL electrostatic potential $|\bar{\psi}|$ (top panel), transverse counterion number density n_+ (middle panel), and transverse coion number density n_- (bottom panel) as functions of the bulk salt concentrations for pH=7. Results are shown for a) nanochannels grafted with short-loose brushes ($N_p = 2000$, $\ell = 80 \text{ nm}$, $d_0 = 34 \text{ nm}$), b) nanochannels grafted with short-loose, but slightly taller brushes ($N_p = 2800$, $\ell = 80 \text{ nm}$, $d_0 = 49 \text{ nm}$), c) nanochannels grafted with short-dense brushes $N_p = 846$, $\ell = 22 \text{ nm}$, $d_0 = 34 \text{ nm}$, d) nanochannels grafted with tall-dense brushes $N_p = 2000$, $\ell = 22 \text{ nm}$, $d_0 = 82 \text{ nm}$, and (e) nanochannels grafted with no brush. Other parameters for all the figures are identical to that in Fig. 6.5.

$d_0 = 34 \text{ nm}$), b) nanochannels grafted with short-loose, but slightly taller brushes ($N_p = 2800$, $\ell = 80 \text{ nm}$, $d_0 = 49 \text{ nm}$), c) nanochannels grafted with short-dense brushes ($N_p = 846$, $\ell = 22 \text{ nm}$, $d_0 = 34 \text{ nm}$), d) nanochannels grafted with tall-dense brushes ($N_p = 2000$, $\ell = 22 \text{ nm}$, $d_0 = 82 \text{ nm}$), and (e) nanochannels grafted with no brush. This variation of the configuration of the grafted brushes (or the complete absence of the brushes) dictates the specific location of the EDL within the nanochannel. As will be discussed later, this location of the EDL along with the EDL thickness (or equivalently, bulk ionic concentration) play vital roles in dictating the overall EOS transport. For example, for the PE-brush-free nanochannel [see Fig. 8.2(e)], the EDL is obviously confined at the wall, whereas for the nanochannels grafted with the PE-brushes [see Fig. 8.2(a-d)], the EDLs are located at the brush tip. This can be understood by noting the location of the maximum value of $|\bar{\psi}|$ for all of these five cases. Variation in the salt concentration has profound influence on the magnitude and the distribution of $|\bar{\psi}|$ for all the five cases. Firstly, the salt-induced alteration of the PE brush height gets manifested in the distribution of the EDL. For brushes with $d_0 > h/2$ ($d_0 < h/2$), brush height first decreases (increases) and then increases (decreases) with the salt concentration [see Figs. 6.5(a),6.7(a)]. Accordingly, the distance of the location of the brush end from the wall first decreases (increases) and then increases (decreases) with the salt concentration for brushes with $d_0 > h/2$ ($d_0 < h/2$) – as a result, the location of the maximum value of the EDL potential decreases (increases) and then increases (decreases) with the salt concentration for brushes with $d_0 > h/2$ ($d_0 < h/2$). Here Figs. 8.2(a-c) represent the cases where $d_0 < h/2$, while Fig. 8.2(d) represents the case where $d_0 > h/2$. Secondly, smaller

salt concentration implies a larger EDL thickness. As a consequence, the extent of spatial decay of $|\bar{\psi}|$ is weak ensuring that there is a distinctly finite value of $|\bar{\psi}|$ even at locations further away from the locations where $|\bar{\psi}|$ is highest. Consequently for weak salt concentration, one witnesses finite $|\bar{\psi}|$ at locations far away from the wall for the PE-brush-free nanochannels, as well as far away on either sides of the charged end of the PE brush for nanochannels grafted with end-charged PE brushes. Finally, $|\bar{\psi}|$ increases in magnitude for smaller salt concentration. It can be easily explained by noting that $|\psi| \sim \sigma_{ch,pH} \lambda$ (where λ is the EDL thickness), thereby justifying enhanced $|\psi|$ for weaker salt concentration (i.e., enhanced λ).

Number density distributions of the ions (n_{\pm}) are commensurate with this $|\bar{\psi}|$ distribution. Consequently, we witness (a) largest (smallest) values of the counterion (coion) number densities at the wall (for PE-brush-free nanochannels) and at the location of the end charge (for end charged PE brush grafted nanochannels) and (b) the ion concentrations demonstrating weakest (strongest) decays for smallest (largest) bulk electrolyte salt concentrations.

8.3.3 Electroosmotic velocity field

In Fig. 8.3, we show the transverse variation of the EOS velocity field for different salt concentration at $pH = 7$ for these five different nanochannel systems. This is the central result of this paper. The key features of these EOS flow fields are as follow. Firstly, for brush-free nanochannels [see Fig. 8.3(e)], the least magnitude of the EOS flow strength as well as the flattest EOS velocity profile (or the profile that

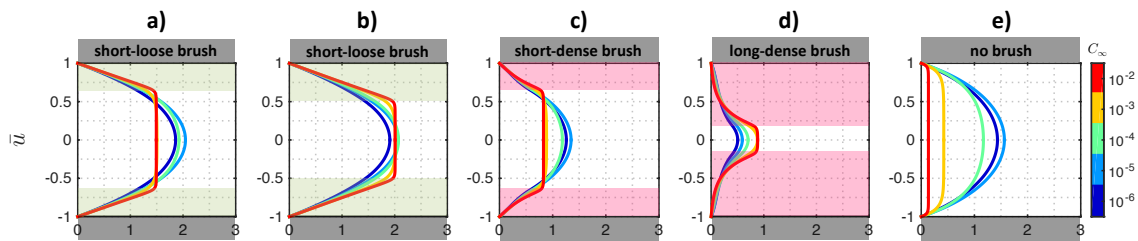


Figure 8.3: Variation of the transverse electroosmotic velocities as functions of the bulk salt concentrations for $\text{pH}=7$. Results are shown for a) nanochannels grafted with short-loose brushes ($N_p = 2000$, $\ell = 80 \text{ nm}$, $d_0 = 34 \text{ nm}$), b) nanochannels grafted with short-loose, but slightly taller brushes ($N_p = 2800$, $\ell = 80 \text{ nm}$, $d_0 = 49 \text{ nm}$), c) nanochannels grafted with short-dense brushes ($N_p = 846$, $\ell = 22 \text{ nm}$, $d_0 = 34 \text{ nm}$), d) nanochannels grafted with tall-dense brushes ($N_p = 2000$, $\ell = 22 \text{ nm}$, $d_0 = 82 \text{ nm}$), and (e) nanochannels grafted with no brush. We represent the loose brushes as light green [see (a) and (b)] and dense brushes as pink [see (c) and (d)]. Other parameters are identical to those in Fig. 8.2.

has closest resemblance to the classical “plug”-shaped EOS flow profile) is witnessed for the largest salt concentration. Also for this case, a decrease in the salt concentration leads to a progressive increase in the magnitude of the EOS flow strength and a progressive decrease in the “plug”-like nature of the flow field. It is trivial to infer that the corresponding variation in ψ [see Fig. 8.2(a), top panel], demonstrating the weakest value and the steepest variation for this largest salt concentration, is responsible for this velocity profile. For nanochannels with short-loose brushes (by “loose”, we imply less dense) [see Fig. 8.3(a), for which $N_p = 2000$, $\ell = 80 \text{ nm}$, $d_0 = 34 \text{ nm}$], we witness, most remarkably, a significantly larger velocity (as compared to the brush-free nanochannels) for large salt concentration. Additionally, we witness that the decrease in the salt concentration first decreases and then increases the strength of the EOS transport particularly in the vicinity of the nanochannel centreline. Further, a decrease in the salt concentration (or equivalently, an increase in the EDL thickness) enforces the velocity profile to suffer a large deviation from its “classical” plug shape. Obviously, the most surprising of all the results is this remarkable enhancement (in particular, for large salt concentration) in the EOS flow strength for nanochannels grafted with the PE brushes, as compared to the EOS flow in brush-free nanochannels. This is completely contrary to the classical understanding that the presence of the brushes lining the nanochannel walls will invariably lower the flow speed on account of PE-induced enhanced drag [26,35]. For the end charged brushes, the EDL is localized at the brush tip that is substantially away from the wall. For larger salt concentration, the EDL thickness being very small, this localization is so strong that the EDL ceases to exist well before the wall. The driving force for

the EOS transport comes from the difference between the counterions (n_+) and coion (n_-) number densities – this difference is maximum within the EDL. Therefore for end-charged brushes, in presence of large bulk salt concentration (i.e., small EDL), this driving force is primarily localized at the location substantially away from wall. As a consequence, the liquid is subjected to a maximum body force at a location where the wall induced retarding shear stress is very minimal. This, in turn, ensures a significantly large influence of the EOS body force, enforcing a large EOS velocity. Therefore, we can infer that this most remarkable scenario where presence of end-charged PE brushes enhance the EOS flow strength is triggered by the localization of the EDL and the corresponding localization of the body force at a distance far away from the wall. It is clear from the above discussions that the key to the development of this augmented EOS transport is the preferential location of the maximum EOS body force away from the wall. This is quantified in Fig. 8.4, where the electroosmotic body force (quantified by those \bar{f} , corresponding to which $\bar{f} > 0$) and the drag force (quantified by those \bar{f} , corresponding to which $\bar{f} < 0$) for each of the five different nanochannel systems and for different salt concentrations are elucidated. One can straightaway compare the case of no brush [Fig. 8.4(e)] and the case of short brushes [see Fig. 8.4(a)] – the results establish that the localization of the maximum EOS body force is substantially away from the wall for the nanochannel with brushes as compared to the nanochannel without the brushes. Also, it is trivial to identify from Fig. 8.4 that the maximum value of the EOS body force occurs for large salt concentration for both nanochannels with and without the brushes. Of course, for small salt concentrations the EDL thickness becomes large – as a consequence, a part

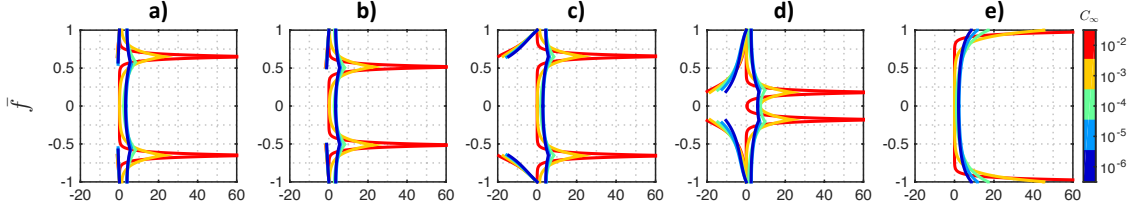


Figure 8.4: Variation of the dimensionless per unit volume forces (\bar{f}) in the transverse direction as functions of the bulk salt concentrations for pH=7. Here $\bar{f} > 0$ represents the dimensionless per unit volume EOS body force, while $\bar{f} < 0$ represents the retarding PE-brush-layer-induced per unit volume drag force. Results are shown for a) nanochannels grafted with short-loose brushes ($N_p = 2000$, $\ell = 80 \text{ nm}$, $d_0 = 34 \text{ nm}$), b) nanochannels grafted with short-loose, but slightly taller brushes ($N_p = 2800$, $\ell = 80 \text{ nm}$, $d_0 = 49 \text{ nm}$), c) nanochannels grafted with short-dense brushes ($N_p = 846$, $\ell = 22 \text{ nm}$, $d_0 = 34 \text{ nm}$), d) nanochannels grafted with tall-dense brushes ($N_p = 2000$, $\ell = 22 \text{ nm}$, $d_0 = 82 \text{ nm}$), and (e) nanochannels grafted with no brush. Other parameters are identical to those in Fig. 8.2.

of the EOS body force is also present near the wall (as the EDLs extend away from the brush tip). Therefore, for such concentration the impact of the localization of the EOS body force at the brush tip gets severely reduced, ensuring minimal (if any) enhancement of the EOS flow speed in brush-grafted nanochannels as compared to the brush-free nanochannels.

A very important question in this context is: *Does the EOS transport depend solely on the value of the brush height or on the parameters that dictate the brush height?* In order to resolve this issue, we probe the EOS transport for the nanochannel

system grafted with end-charged PE brushes of same d_0 as that of Fig 8.3(a) (i.e., $d_0 = 34nm$) but having a larger grafting density ($\ell = 22 nm$) and a smaller N_p ($N_p = 846$) (i.e., we study the case of nanochannels grafted with short and dense brushes) [see Fig. 8.3(c)]. Here, we clearly see that the velocity for the case with larger σ is distinctly smaller (particularly for a large salt concentration), on account of the larger drag force (since drag coefficient $\sim \sigma^{2/3}$). This becomes plainly evident from the comparison of the drag forces (represented by those \bar{f} values for which $\bar{f} < 0$) for these two cases [please see Figs. 8.4(a) and 8.4(c)].

Finally, we are interested to probe the effect of the brush height in the augmentation of the EOS flow strength. For that purpose, we probe the EOS flow behavior for the brushes with heights greater than $d_0 = 34 nm$. We consider a taller brush (as compared to one where $d_0 = 34 nm$) with a large σ ($N_p = 2000$, $\ell = 22 nm$, $d_0 = 84 nm$) [see Fig. 8.3(d) for the corresponding EOS flow profile] and another taller brush (as compared to one where $d_0 = 34 nm$) with a small σ ($N_p = 2800$, $\ell = 80 nm$, $d_0 = 49 nm$) [see Fig. 8.3(b) for the corresponding EOS flow profile]. For the taller brush with large σ , the influence of larger σ in augmenting the drag overwhelms the effect associated with the localization of the EOS body force at the brush tip, resulting in a much smaller velocity (particularly at large salt concentration) [please compare the EOS flow profiles of Figs.8.3(a) and (d)]. Such profound influence of the drag force for taller and more dense brushes can be confirmed by noting the significantly large drag force in Fig. 8.4(d). On the other hand, for taller but less dense brushes [the corresponding EOS flow profile is shown in Fig. 8.3(b)], it is the localization of the EDL at the brush tip that governs the flow, leading to an

EOS flow strength that is more (particularly at large salt concentration) than that for nanochannels grafted with shorter and less dense brushes [the corresponding EOS flow profile is shown in Fig. 8.3(a)]. Of course, this issue gets substantiated when the corresponding forces are compared [i.e., compare the forces shown in Fig. 8.4(a) and (b)] – the drag force is similar for both these cases, but the maximum of the EOS body is located at a greater distance from the wall for the taller brush.

For nanochannels with both kinds of taller brushes (i.e., taller brushes with large σ or large N) as well as shorter brushes (with large or small σ), smallness of the EDL thickness for large salt concentrations will ensure that the velocity profile remains very flat (or “plug”-shaped) outside the brush, while a larger EDL (or equivalently, a larger spatial distribution of the charge density) for smaller salt concentration ensures a velocity profile far deviated from the “plug”-shaped profiles.

8.3.4 pH-responsive electrostatics and EOS velocity fields

In Figs. 8.5,8.6,8.7,8.8, we show the effect of the variation of pH and salt concentration on $|\bar{\psi}|$, \bar{u} , \bar{f} , n_+, n_- , and n_{H^+} for the four different kinds of PE-grafted nanochannel systems. For small pH , the concentration of H^+ ions in the electrolyte solution is so high that the ionization of the end-charge-producing group (this ionization produces the H^+ ions) is severely retarded. Accordingly, the magnitude of the end-charge is substantially lowered. This is reflected in substantially reduced value of $|\bar{\psi}|$ and $|\bar{u}|$ for cases with small pH ($pH = 3, 4$) for all the four different PE-brush-grafted nanochannel systems. On the other hand, for nanochannels grafted with both

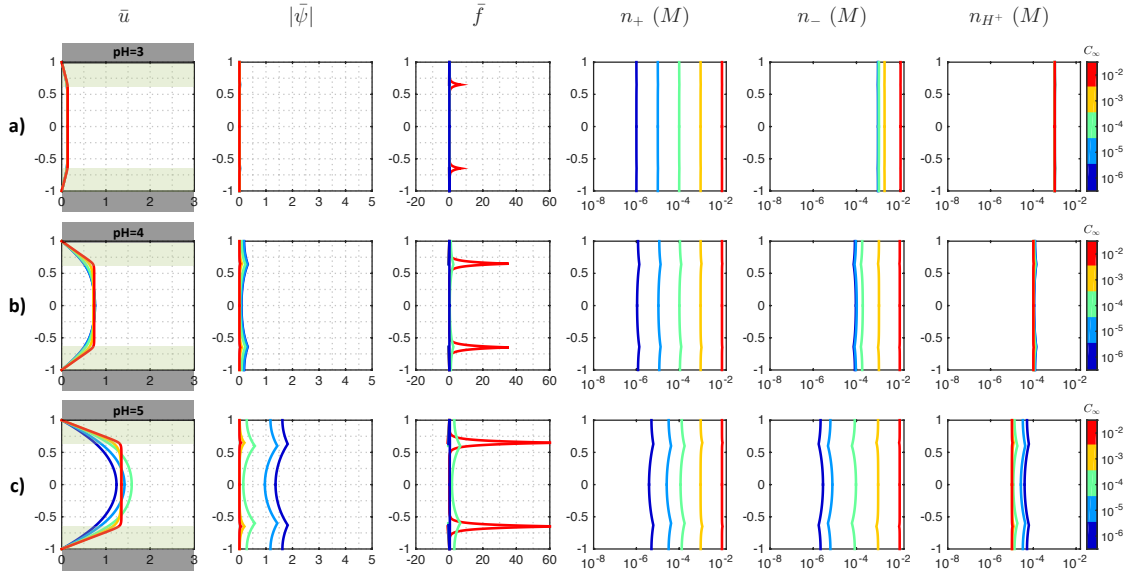


Figure 8.5: Transverse variation of $|\bar{\psi}|$ (magnitude of dimensionless electrostatic potential), \bar{u} (dimensionless EOS velocity), \bar{f} ($\bar{f} > 0$ represents the dimensionless per unit volume EOS body force, while $\bar{f} < 0$ represents the retarding PE-brush-layer-induced per unit volume drag force), n_+ (counterion number density), n_- (coion number density), and n_{H^+} (number density of hydrogen ions). Results are shown for nanochannels grafted with short-loose brushes ($N_p = 2000$, $\ell = 80 \text{ nm}$, $d_0 = 34 \text{ nm}$) for (a) pH=3, (b) pH=4, and (c) pH=5. Other parameters are identical to those in Fig. 8.2.

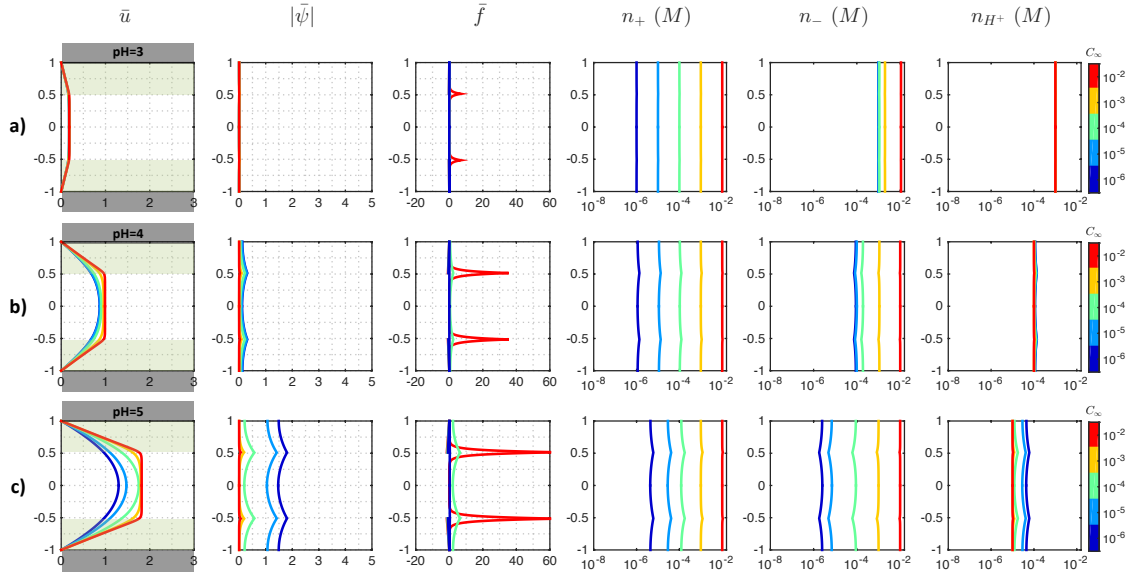


Figure 8.6: Transverse variation of $|\bar{\psi}|$ (magnitude of dimensionless electrostatic potential), \bar{u} (dimensionless EOS velocity), \bar{f} ($\bar{f} > 0$ represents the dimensionless per unit volume EOS body force, while $\bar{f} < 0$ represents the retarding PE-brush-layer-induced per unit volume drag force), n_+ (counterion number density), n_- (coion number density), and n_{H^+} (number density of hydrogen ions). Results are shown for nanochannels grafted with short-loose, but slightly taller brushes ($N_p = 2800$, $\ell = 80 \text{ nm}$, $d_0 = 49 \text{ nm}$) for (a) pH=3, (b) pH=4, and (c) pH=5. Other parameters are identical to those in Fig. 8.2.

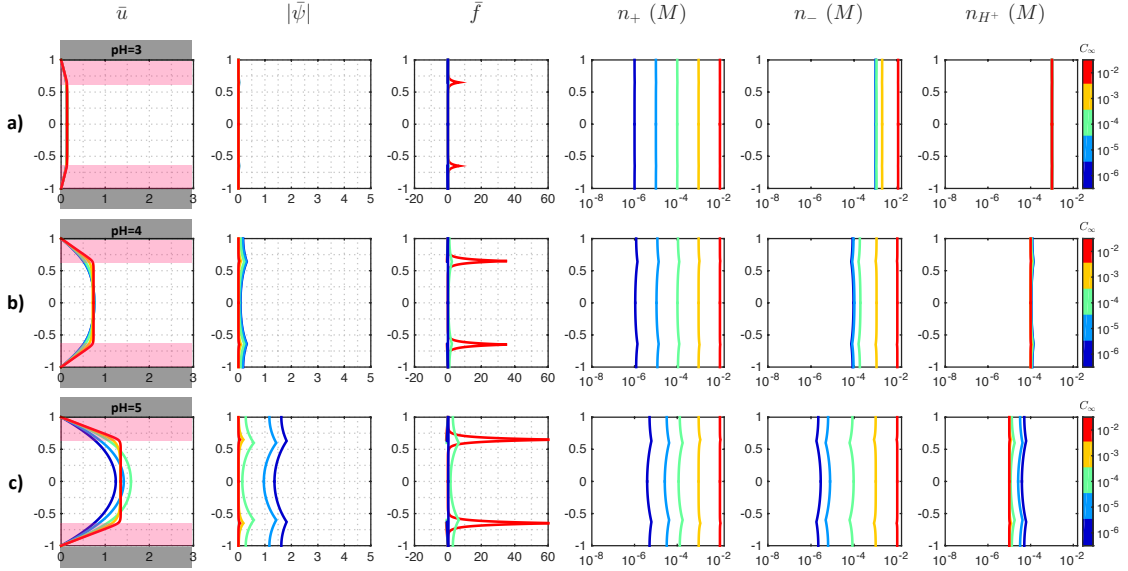


Figure 8.7: Transverse variation of $|\bar{\psi}|$ (magnitude of dimensionless electrostatic potential), \bar{u} (dimensionless EOS velocity), \bar{f} ($\bar{f} > 0$ represents the dimensionless per unit volume EOS body force, while $\bar{f} < 0$ represents the retarding PE-brush-layer-induced per unit volume drag force), n_+ (counterion number density), n_- (coion number density), and n_{H^+} (number density of hydrogen ions). Results are shown for nanochannels grafted with short-dense brushes ($N_p = 846$, $\ell = 22 \text{ nm}$, $d_0 = 34 \text{ nm}$) for (a) pH=3, (b) pH=4, and (c) pH=5. Other parameters are identical to those in Fig. 8.2.

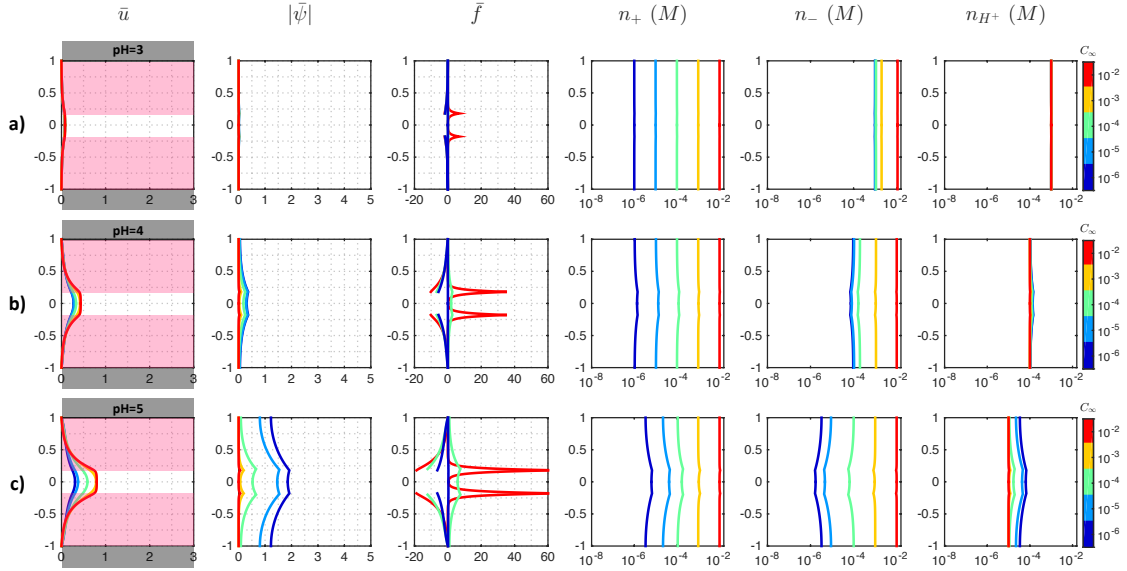


Figure 8.8: Transverse variation of $|\bar{\psi}|$ (magnitude of dimensionless electrostatic potential), \bar{u} (dimensionless EOS velocity), \bar{f} ($\bar{f} > 0$ represents the dimensionless per unit volume EOS body force, while $\bar{f} < 0$ represents the retarding PE-brush-layer-induced per unit volume drag force), n_+ (counterion number density), n_- (coion number density), and n_{H^+} (number density of hydrogen ions). Results are shown for nanochannels grafted with tall-dense brushes ($N_p = 2000$, $\ell = 22 \text{ nm}$, $d_0 = 82 \text{ nm}$) for (a) pH=3, (b) pH=4, and (c) pH=5. Other parameters are identical to those in Fig. 8.2.

short and tall as well as loose and dense brushes, only for $pH \geq 5$ we witness the salt concentration dependent qualitative variation in $|\bar{\psi}|$ and \bar{u} that have been described in Figs. 8.2 and 8.3.

8.3.5 Phase space for the volume flow rate ratio in nanochannels grafted with end-charged PE brushes

The interplay of the grafting density and the monomer size in dictating the strength of the overall EOS transport in nanochannels grafted with the end-charge brushes is summarized in the iso-volume-flow rate (or iso-Q) phase-space plot shown in Fig. 8.9. This phase space is provided for large salt concentration ($c_\infty = 10^{-2} M$) and large pH ($pH = 7$) (i.e., the conditions corresponding to which the EOS transport in PE-brush-grafted nanochannels is most augmented). In this figure, the lines with numbers denote the $\ell - N_p$ combinations that ensure identical dimensionless volume flow rate ratios, expressed as:

$$\bar{Q} = \frac{\int_{-1}^1 \bar{u}_B d\bar{y}}{\int_{-1}^1 \bar{u}_{NB} d\bar{y}}, \quad (8.4)$$

where \bar{u}_B and \bar{u}_{NB} are the dimensionless EOS velocity profiles in nanochannels with and without the brushes, respectively. Of course, in Fig. 8.9, we also show (see the shaded region) the $\ell - N_p$ combination that ensure that the grafted polymer molecules form brushes that have height less than the nanochannel half height (so that there is no interpenetration of the brushes grafted on the two opposing walls of the nanochannel). Therefore, basically we focus on the iso-Q lines that are within this shaded zone. The first and the most important finding is the massive increase in the volume flow rate

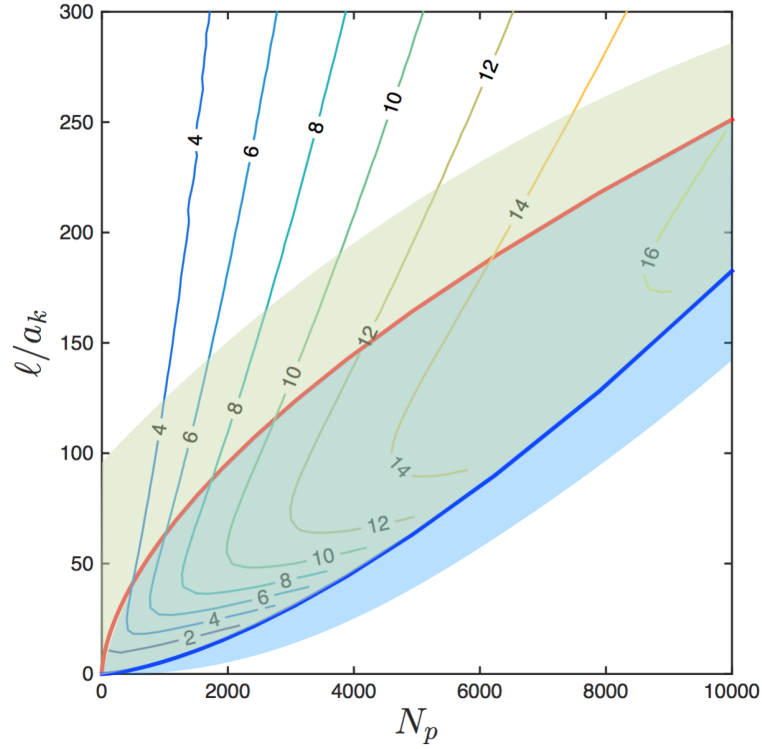


Figure 8.9: Phase space for iso-volume-flow-rate. The lines with numbers denote the $\ell - N_p$ combinations that ensure identical flow rates with the numbers on the lines denoting the dimensionless flow rate, defined in eq.(8.4). The shaded region shows the $\ell - N_p$ combinations that ensure that the grafted PE molecules form brushes whose heights are less than the nanochannel half height. Below this shaded zone the brushes are taller than the nanochannel half height, while above the shaded zone the grafting is so weak that the grafted polymer molecules no longer form the brushes. Results here are shown for $c_\infty = 10^{-2} M$, $\sigma_{ch} = -8 \times 10^{-4} C/m^2$, and $pH = 7$.

for the nanochannels with brushes, evident by the large magnitudes of the volume flow rate ratios [see Fig. 8.9 and eq.(8.4)]. As discussed previously, combination of ℓ and N_p dictate the brush height as well as the drag force and the interplay of these two factors eventually decide EOS flow profile. This flow profile along with the space available for the flow (i.e., the transverse section of the nanochannel not occupied by the brushes) dictate the consequent volume flow rate. For very small ℓ/a_k (or equivalently for a very large grafting density) at a given N_p ($N_p \geq 2000$) the brush height is very large so that the major part of the nanochannel is blocked by the brush, causing a relatively small volume flow rate. Of course, for such a large grafting density, the brush-induced drag force is also substantially high, which contributes to ensure a very small flow rate. On a subsequent increase of ℓ/a_k (or equivalently, a decrease in the grafting density) three things happen: first a slit-like gap opens due to the reduction of the brush height, second the brush-induced drag reduces, and third the effect of the localization of the EOS body force (on account of the localization of the EDL at the brush end, particularly for large salt concentration as has been studied in Fig. 8.9) away from the wall starts becoming important. All these three factors contribute to enhancing the flow rate. How these three factors pan out and how they interplay to influence the final flow rate with a further increase of ℓ/a_k decides the above iso-Q phase diagram. A further increase in ℓ/a_k leads to a greater gap opening and a lesser effect of the localization of the EOS body force away from the wall (both caused by a reduction in the brush height) and a further weakening of the drag force – the consequence is a further increase in the flow rate. Here the central factor is this localization of the body force away from the wall – while an increase in ℓ/a_k

and a consequent lowering of the brush height makes this localization closer to the wall, its influence coupled with an augmented flow-passage area and a substantially reduced (or even non-existent) brush-induced drag ensures this augmented flow rate. However, beyond a certain value of ℓ/a_k , the brush height becomes so small that this localization effect is virtually non-existent and this, in turn, ensures a net reduction in the flow rate. In this way, we can explain why the flow rate first increases and then decreases with an increase in ℓ/a_k for a given N_p .

8.4 Discussions

8.4.1 Impact of the choice of the monomer profile

Quantification of the monomer distribution along the brush length is critical for quantifying the drag coefficient used in the modelling of the EOS transport. In the present study, we have considered a uniform monomer profile (or equivalently, a stepped monomer profile where $\phi = 1$) as proposed by Alexander [1] and de Gennes [2, 3] and subsequently used in a large number of studies on electrokinetic transport in PE-grafted nanochannels [35, 53, 79, 123]. Of course, a more complete model would have necessitated a more appropriate form of the monomer profile that is self-consistent with the presence of PE electrostatic contribution due to the presence of the charge only at the PE tip. Mishra et al. [126] and Zhulina and Borisov [45] respectively proposed a parabolic and an exponentially decaying monomer distribution for the case where the PE brushes contained charges along its entire backbone. However, for the present case where the PE electrostatics is due to the presence of

only PE end charge, monomer distribution remains unknown. While developing this model by first estimating the appropriate monomer distribution for the end-charged PE brushes is indeed a possibility, we refrain from doing that and provide our results for the simplistic case of uniform monomer profile. The reason is that we believe that the consideration of a non-uniform, decaying (along the brush height) monomer profile, if at all, will only strengthen the central message of the present paper, which is the enhancement of the EOS flow by end-charged PE brushes. This stems from the fact that for such a monomer distribution, the monomer density will be least near the brush tip and accordingly the PE-induced drag force will be much smaller (as compared to the case of $\phi = 1$) near the brush tip. Accordingly, the retardation to the flow near the PE-tip (i.e., where the EOS body force is localized) due to the wall shear and the PE drag will reduce even further, thereby ensuring an even further augmentation of the EOS transport.

8.5 Conclusions

In this study, we describe the most remarkable EOS flow *enhancement* in nanochannels grafted with the end-charged PE brushes, completely contrary to the findings of the existing studies demonstrating substantial EOS flow reduction in PE-grafted nanochannels [26, 35, 84]. Of course, the critical difference between these previous studies and the present study is that for all these previous studies the PE brush is charged along its entire backbone, while in the present case the PE molecule contains charge only at its non-grafted end located far away from the grafting sur-

face. As a consequence for the end-charged brush, the EDL and the EDL-induced maximum body force for driving the EOS-flow is localized near the brush free end (i.e., far away from the wall), ensuring that the resulting flow is subjected to very weak wall-induced retarding shear force enabling a very large EOS transport. We witness much larger EOS flow strength as compared to nanochannels without the PE brushes; however, an increase in the brush height enhances the EOS flow strength progressively only when the parameters that dictate the increase in the brush height does not additionally increase the drag coefficient. We believe that the present study proposes a hitherto unknown application of the PE-brush-grafted nanochannels of *enhancing* the EOS transport – we anticipate that this finding will open up new avenues of manipulating the nanofluidic transport using nano-functionalized interfaces.

Chapter 9: Electrokinetics in nanochannels grafted with backbone-charged polyelectrolyte brushes

In this chapter¹, calculations are provided to quantify the electroosmotic (EOS) transport in nanochannels grafted with backbone-charged polyelectrolyte brushes, with the brushes being modelled in the coupled regime. “Backbone-charged” or BBC signifies the condition where the PE brushes have charges along their entire backbone. The speciality of the theory provided here is that it accounts for the first time the specificities of the PE brush configuration in determining the transport in nanochannels grafted with such brushes. Such BBC PE brushes grafted at a single interface is known to exhibit monotonic shrinking in height with an increase in concentration. Here we demonstrate that such monotonic shrinking occurs even in presence of nanoconfinement, regardless of the extent of the confinement. Secondly, and more importantly, we witness that although the EOS transport in such BBC PE brush grafted nanochannels is typically weaker than the EOS transport in rigid, charged nanochannels having a surface charge equal to the

¹One part of this chapter has been partly published as *G. Chen and S. Das, Anomalous shrinking-swelling of nanoconfined end-charged polyelectrolyte brushes: Interplay of confinement and electrostatic effects. J. Phys. Chem. B, Vol. 120, 6848-6857 (2016)* and the other part will be submitted as *G. Chen and S. Das, Transport in nanochannels grafted with backbone-charged polyelectrolyte brushes. Soft Matter (2017)*.

volume charge associated with the brushes, it is possible to identify certain combination of parameters at large salt concentration where the EOS transport in brush-grafted nanochannels may become stronger.

9.1 Introduction

While the electroosmotic (EOS) transport in end-charged brushes revealed a number of extremely fascinating cases (see Chapter 8), the majority of problems on nanochannels grafted with PE brushes involve brushes that contain charges along their entire backbone. Such brushes are denoted here as “backbone-charged” (BBC) brushes in order to differentiate them from end-charged brushes. In this chapter, for the first time the electrokinetic transport in nanochannels grafted with BBC PE brushes has been modelled by explicitly accounting for the PE brush configuration. In other words, we first quantify the equilibrium brush height by balancing the elastic, excluded volume and electrostatic energies of the brush with the electrostatic energy of the EDL. The resulting information of the EDL electrostatics and the brush equilibrium height is subsequently used to calculate the EOS transport. For simplicity, we consider the stepped monomer profile that helps to specify a drag force exerted on the fluid flow as well the appropriate expressions for the contributions of the elastic, excluded volume, and the electrostatic energies of the PE molecule.

Our findings reveal the well-known charge and concentrations dependence of the variation of the BBC PE brush height [103] – we witness (a) brush height d is always greater than d_0 (equivalent height for the uncharged brush) regardless of the extent

of confinement and salt concentration and (b) brush height decreases monotonically with the salt concentration. Our main findings, however, are the elucidation of the EOS transport in nanochannels grafted with BBC PE brushes of different sizes and grafting densities. First and foremost, we reveal that for large concentration, EOS transport even in BBC PE brushes can outweigh that in brush-less channels in case the grafting density is weak. However, such enhancement is not possible in case the grafting density is large or the salt concentration is weak. We explain all our findings in terms of detailed PE brush architecture as well as the competition of the EOS driving force and the retarding drag force. Finally, we tabulate the key differences between the EOS transport in nanochannels grafted with end charged and BBC brushes.

9.2 Theory

9.2.1 Derivation of the Governing Equations for the Equilibrium Brush Height

We consider a nanochannel whose inner walls are grafted with the BBC negative PE brushes with constant charge density (i.e., pH-non-responsive charge density) along their backbone. We shall first derive its equilibrium configuration and electrostatics; subsequently, we shall use these information to compute the EOS transport in the nanochannel grafted with these BBC negative PE brushes. In order to obtain the equilibrium configuration and electrostatics of these nanoconfined brushes, we start

from the free energy consideration. Free energy of the system can be expressed as:

$$F = F_B + F_{EDL} = F_{B,els} + F_{B,EV} + F_{B,elec} + F_{EDL}. \quad (9.1)$$

Eq.(9.1) is based on the fact that the free energy of the system consists of the free energy associated with the PE brush (F_B) and the free energy associated with the resulting formation of the EDL (F_{EDL}). We further assume that F_B consists of an elastic contribution ($F_{B,els}$), an excluded volume contribution ($F_{B,EV}$), and an electrostatic contribution ($F_{B,elec}$).

These individual energy components associated with the PE brushes can further be expressed as (considering only the bottom half of the nanochannel):

$$F_{B,els} = \frac{3k_B T}{2} \frac{d^2}{N_p a_k^2}, \quad (9.2)$$

$$F_{B,EV} = \frac{a_k^3 (1 - 2\chi) k_B T}{2} \frac{N_p^2}{\ell^2 d}. \quad (9.3)$$

In eqs.(9.2,9.3), $k_B T$ is the thermal energy, d is the PE brush height (to be determined self constantly later), v_0 is the excluded volume parameter, χ is the Flory-Huggins parameter, $k_B T$ is the thermal energy, a_k is the Kuhn length, N_p is the size (or the number of monomers) of a polyelectrolyte chain, and ℓ is average spacing between the grafted PE brushes. It is very easy to see that $F_{B,els}$ and $F_{B,EV}$ have expressions identical to that for the end-charged brushes [see eqs.(6.3,6.4)], which stems from the fact that here too we consider a stepped monomer profile (i.e., monomer concentration $\phi = 1$ inside the brush and $\phi = 0$ outside the brush) [1-3].

It is worthwhile to mention here that for this case as well, the height d_0 for the uncharged brush will be obtained from the balance of the elastic and excluded volume

free energies of the brush, yielding an expression identical to eq.(6.7)

For the PE brush, we may express $F_{B,elec}$ as:

$$F_{B,elec} = \int f_{B,elec} d^3\mathbf{r} = \int (-en_{PE,ch}\psi) d^3\mathbf{r} = -\ell^2 \int_{-h}^{-h+d} dy, \quad (9.4)$$

where $f_{B,elec}$ is the electrostatic energy density of the PE brush, e is the electronic charge, $n_{PE,ch}$ is the (constant) number density of the PE backbone charges, ψ is the electrostatic potential, and n_∞ is the bulk number density of the electrolyte ions.

We consider a uniform distribution of the monomers and $n_{PE,ch}$ is related to N_p as $n_{PE,ch} = N_p f_{ch}/(\ell^2 d)$. This present calculation differs from that of the end-charged PE brushes in this expression of $F_{B,elec}$. It is straightforward to see that while $F_{B,elec}$ for end-charged brushes is a surface integral (on account of the charged being localized at the tip), $F_{B,elec}$ for the present case is a volume integral (on account of the presence of the charges along the entire backbone of the PE brushes). Finally, F_{EDL} takes the same form as that for the end-charged brushes, i.e.,

$$F_{EDL} = \int \left[\int_{-h}^0 f_{EDL}(\psi, \psi', n_\pm) dy \right] d^2\mathbf{r} = \ell^2 \int_{-h}^0 f_{EDL}(\psi, \psi', n_\pm) dy, \quad (9.5)$$

where $f_{EDL}(\psi, \psi', n_\pm)$ is the EDL free energy density expressed as:

$$f_{EDL}(\psi, \psi', n_\pm) = -\frac{\epsilon_0 \epsilon_r}{2} \left| \frac{d\psi}{dy} \right|^2 + e\psi (n_+ - n_-) + k_B T \left[n_+ \left(\ln \left(\frac{n_+}{n_{+, \infty}} \right) - 1 \right) + n_- \left(\ln \left(\frac{n_-}{n_{-, \infty}} \right) - 1 \right) \right]. \quad (9.6)$$

Here ϵ_0 is the permittivity of free space, ϵ_r is the relative permittivity of water, e is the electronic charge, $k_B T$ is the thermal energy, and $n_{+, \infty} = n_{-, \infty} = n_\infty$ is the bulk

number density of the electrolyte ions.

Therefore, we can obtain the complete free energy expression by using eqs.(9.2,9.3,9.4,9.5,9.6) in eq.(9.1). The equilibrium will be obtained by minimizing this complete free energy expression with respect to ψ , n_{\pm} and d .

Minimizing with respect to ψ we shall get back the classical Poisson equation that will have different forms inside and outside the polymer layer, i.e.,

$$\begin{aligned} \frac{\delta(F)}{\delta\psi} = 0 &\Rightarrow \frac{\partial f}{\partial\psi} - \frac{d}{dy} \left(\frac{\partial f}{\partial\psi'} \right) = 0 \\ \Rightarrow \frac{d^2\psi}{dy^2} &= \frac{e \left(n_- - n_+ + \frac{N_p f_{ch}}{\ell^2 d} \right)}{\epsilon_0 \epsilon_r} \quad [\text{for } -h \leq y \leq -h + d], \\ \Rightarrow \frac{d^2\psi}{dy^2} &= \frac{e(n_- - n_+)}{\epsilon_0 \epsilon_r} \quad [\text{for } -h + d \leq y \leq 0]. \end{aligned} \quad (9.7)$$

Minimizing with respect to n_{\pm} we shall get back the classical Boltzmann distribution for both inside and outside the polymer layer, i.e.,

$$\frac{\delta F}{\delta n_{\pm}} = 0 \Rightarrow n_{\pm} = n_{\infty} \exp \left(\mp \frac{e\psi}{k_B T} \right). \quad (9.8)$$

Using eq.(9.8) we can recover the Poisson-Boltzmann equation modified to account for the contribution of the number density of the PE charges:

$$\begin{aligned} \frac{d^2\psi}{dy^2} &= \frac{2n_{\infty}e}{\epsilon_0 \epsilon_r} \sinh \left(\frac{e\psi}{k_B T} \right) + \frac{e}{\epsilon_0 \epsilon_r} \frac{N_p f_{ch}}{\ell^2 d} \quad [\text{for } -h \leq y \leq -h + d], \\ \frac{d^2\psi}{dy^2} &= \frac{2n_{\infty}e}{\epsilon_0 \epsilon_r} \sinh \left(\frac{e\psi}{k_B T} \right) \quad [\text{for } -h + d \leq y \leq 0]. \end{aligned} \quad (9.9)$$

Similar to the procedure adopted for the analysis of end-charged brushes, here too we shall do the minimization of the free energy with respect to d , which in turn will yield the equation governing the equilibrium brush thickness $d_{eq,PE}$ after non-dimensionalizing the different equations. The detailed procedure is illustrated in the following subsection.

9.2.2 Non-dimensionalization and analytical solutions for the Equilibrium Brush Height

To obtain the analytical solution for the equilibrium height of the BBC PE brushes, let us first non-dimensionalize the free energy. Eq. (9.1) can be expressed in the following dimensionless form:

$$\bar{F} = \bar{F}_{B,els} + \bar{F}_{B,EV} + \bar{F}_{elec} \quad (9.10)$$

where $\bar{F} = \frac{F}{k_B T}$, $\bar{F}_{B,els} = \frac{F_{B,els}}{k_B T} = \frac{\alpha}{2} \frac{\bar{d}^2}{N_p}$, $\bar{F}_{B,EV} = \frac{F_{B,EV}}{k_B T} = \beta \frac{N_p^2}{\bar{d}}$, $\bar{F}_{elec} = \frac{F_{B,elec} + F_{EDL}}{k_B T} = \frac{1}{2\gamma} \int_{-1}^0 \bar{f} d\bar{y}$, $\bar{y} = \frac{y}{h}$, $\bar{d} = \frac{d}{h}$, $\alpha = \frac{3h^2}{a_k^2}$, $\beta = \frac{a_k^3}{2\ell^2 h} (1 - 2\chi)$, $\gamma = \frac{1}{2\ell^2 h n_\infty}$ and $\bar{f} = \frac{f_{EDL} + f_{B,elec}}{k_B T n_\infty}$.

Of course, using eqs.(9.4,9.5,9.6,9.8) one can express \bar{f} as:

$$\begin{aligned} \bar{f} &= -\bar{\lambda}^2 \left| \frac{d\bar{\psi}}{d\bar{y}} \right|^2 - 2 \cosh(\bar{\psi}) - \frac{2\bar{\psi}\gamma N_p f_{ch}}{\bar{d}} \quad [\text{for } -1 \leq \bar{y} \leq -1 + \bar{d}], \\ \bar{f} &= -\bar{\lambda}^2 \left| \frac{d\bar{\psi}}{d\bar{y}} \right|^2 - 2 \cosh(\bar{\psi}) \quad [\text{for } -1 + \bar{d} \leq \bar{y} \leq 0], \end{aligned} \quad (9.11)$$

where $\bar{\psi} = \frac{e\psi}{k_B T}$ and $\bar{\lambda} = \frac{\lambda}{h}$ ($\lambda = \sqrt{\frac{\epsilon_0 \epsilon_r k_B T}{2n_\infty e^2 z}}$ being the EDL thickness).

Employing the Debye-Hückel linearization (valid for $|\bar{\psi}| < 1$), we can write eq.(9.9) in dimensionless form as:

$$\begin{aligned} \frac{d^2 \bar{\psi}}{d\bar{y}^2} &= \frac{1}{\bar{\lambda}^2} \left[\sinh(\bar{\psi}) + \frac{\gamma N_p f_{ch}}{\bar{d}} \right] \approx \frac{1}{\bar{\lambda}^2} \left[\bar{\psi} + \frac{\gamma N_p f_{ch}}{\bar{d}} \right] \quad [\text{for } -1 \leq \bar{y} \leq -1 + \bar{d}], \\ \frac{d^2 \bar{\psi}}{d\bar{y}^2} &= \frac{\sinh(\bar{\psi})}{\bar{\lambda}^2} \approx \frac{\bar{\psi}}{\bar{\lambda}^2} \quad [\text{for } -1 + \bar{d} \leq \bar{y} \leq 0] \end{aligned} \quad (9.12)$$

Now $\bar{\psi}$ can be solved analytically using eq.(9.12) with the following boundary condi-

tions:

$$\begin{aligned}
\left(\frac{d\bar{\psi}}{d\bar{y}}\right)_{y=(-1+\bar{d})^+} &= \left(\frac{d\bar{\psi}}{d\bar{y}}\right)_{y=(-1+\bar{d})^-}, \\
(\bar{\psi})_{(y=-1+\bar{d})^-} &= (\bar{\psi})_{(y=-1+\bar{d})^+}, \\
\left(\frac{d\bar{\psi}}{d\bar{y}}\right)_{y=-1} &= 0, \quad \left(\frac{d\bar{\psi}}{d\bar{y}}\right)_{y=0} = 0.
\end{aligned} \tag{9.13}$$

This analytical solution for $\bar{\psi}$ is:

$$\begin{aligned}
\bar{\psi} &= -\frac{\gamma N_p f_{ch}}{\bar{d}} \left[1 + \frac{\sinh\left(\frac{-1+\bar{d}}{\lambda}\right)}{\sinh\left(\frac{1}{\lambda}\right)} \cosh\left(\frac{\bar{y}+1}{\lambda}\right) \right] \quad [\text{for } -1 \leq \bar{y} \leq -1 + \bar{d}], \\
\bar{\psi} &= -\frac{\gamma N_p f_{ch}}{\bar{d}} \frac{\sinh\left(\frac{\bar{d}}{\lambda}\right)}{\sinh\left(\frac{1}{\lambda}\right)} \cosh\left(\frac{\bar{y}}{\lambda}\right) \quad [\text{for } -1 + \bar{d} \leq \bar{y} \leq 0].
\end{aligned} \tag{9.14}$$

Using eq.(9.14), we can re-express eq.(9.11) as:

$$\begin{aligned}
\bar{f} &= -\frac{\gamma^2 N_p^2 f_{ch}^2}{\bar{d}^2} \frac{\sinh^2\left(\frac{-1+\bar{d}}{\lambda}\right)}{\sinh^2\left(\frac{1}{\lambda}\right)} \cosh\left(2\frac{\bar{y}+1}{\lambda}\right) - 2 + \frac{\gamma^2 N_p^2 f_{ch}^2}{\bar{d}^2} \quad [\text{for } -1 \leq \bar{y} \leq -1 + \bar{d}], \\
\bar{f} &= -\frac{\gamma^2 N_p^2 f_{ch}^2}{\bar{d}^2} \frac{\sinh^2\left(\frac{\bar{d}}{\lambda}\right)}{\sinh^2\left(\frac{1}{\lambda}\right)} \cosh\left(\frac{2\bar{y}}{\lambda}\right) - 2 \quad [\text{for } -1 + \bar{d} \leq \bar{y} \leq 0]
\end{aligned} \tag{9.15}$$

Consequently, the total dimensionless electrostatic free energy $\bar{F}_{elec} = \bar{F}_{B,elec} + \bar{F}_{EDL} =$

$\frac{F_{B,elec} + F_{EDL}}{k_B T}$ can be expressed as:

$$\bar{F}_{elec} = -\frac{\gamma N_p^2 f_{ch}^2 \bar{\lambda}}{2\bar{d}} \frac{\sinh\left(\frac{\bar{d}}{\lambda}\right) \sinh\left(\frac{1-\bar{d}}{\lambda}\right)}{\bar{d} \sinh\left(\frac{1}{\lambda}\right)} - \frac{1}{\gamma} + \frac{\gamma N_p^2 f_{ch}^2}{2\bar{d}}. \tag{9.16}$$

In the above equation, the first two terms on the RHS represent the energy associated with the EDL formation (\bar{F}_{EDL}), while the second term represents the electrostatic energy associated with the charges on the brush ($\bar{F}_{B,elec}$). Therefore

eq.(9.10) can be now expressed as:

$$\bar{F} = \frac{\alpha}{2} \frac{\bar{d}^2}{N_p} + \beta \frac{N_p^2}{\bar{d}} + \frac{\gamma}{2} \frac{N_p^2 f_{ch}^2}{\bar{d}} \left[1 - \frac{\bar{\lambda} \sinh\left(\frac{\bar{d}}{\bar{\lambda}}\right) \sinh\left(\frac{1-\bar{d}}{\bar{\lambda}}\right)}{\sinh\left(\frac{1}{\bar{\lambda}}\right)} \right] - \frac{1}{\gamma} \quad (9.17)$$

Of course the exact value of \bar{d} can be obtained from the equation yielded by minimizing this free energy expression [see eq.(9.17)] with respect to the dimensionless brush height \bar{d} . The resulting equation (see below) will be solved to obtain equilibrium \bar{d} .

$$\begin{aligned} \left(\frac{\delta \bar{F}}{\delta \bar{d}} \right)_{\bar{d}=\bar{d}_{eq,PE}} &= 0 \\ \Rightarrow 0 &= \alpha \frac{\bar{d}_{eq,PE}}{N_p} - \beta \frac{N_p^2}{\bar{d}_{eq,PE}^2} + \\ & \frac{\gamma}{\bar{d}_{eq,PE}^2} \frac{N_p^2 f_{ch}^2 \sinh\left(\frac{-1+\bar{d}_{eq,PE}}{\bar{\lambda}}\right) \left[\cosh\left(\frac{\bar{d}_{eq,PE}}{\bar{\lambda}}\right) - \frac{\bar{\lambda}}{\bar{d}_{eq,PE}} \sinh\left(\frac{\bar{d}_{eq,PE}}{\bar{\lambda}}\right) \right]}{\sinh\left(\frac{1}{\bar{\lambda}}\right)}. \end{aligned} \quad (9.18)$$

9.2.3 Numerical Solutions for the Equilibrium Brush Height

The proposed analytical approach will remain valid only when the backbone charge density of the BBC PE brushes is small enough to ensure that the induced electrostatic potential remain small ($|\bar{\psi}| < 1$), allowing the employment of the Debye-Hückel linearization approach. In case this charge density is not small and we get $|\bar{\psi}| > 1$, we shall need to obtain a numerical solution to the problem. For such a case, ψ will be obtained by solving eq.(9.9) numerically in presence of the boundary conditions expressed in eq.(9.13). Subsequently, this ψ will be used in eq.(9.11) to obtain \bar{f} , which in turn will provide the total free energy [by using eq.(9.10)]. This final energy equation will subsequently be minimized with respect to \bar{d} numerically to obtain the numerical solution.

9.2.4 Calculation of the EOS transport

The analyses in the previous subsections provide the equilibrium brush height d as well as the equilibrium electrostatics (in terms of ψ , n_{\pm}). These equilibrium values will be subsequently used in equation governing the EOS transport (see below):

$$\begin{aligned} \eta \frac{d^2 u}{dy^2} + e(n_+ - n_-)E - \frac{\eta}{k}u &= 0 \quad [\text{for } -h \leq y \leq -h + d], \\ \eta \frac{d^2 u}{dy^2} + e(n_+ - n_-)E &= 0 \quad [\text{for } -h + d \leq y \leq 0], \end{aligned} \quad (9.19)$$

where all the variables are defined in eq.(8.1).

Eq.(9.19) can be expressed in dimensionless form as

$$\begin{aligned} \frac{d^2 \bar{u}}{d\bar{y}^2} - \frac{\bar{E}}{\lambda^2} \sinh(\bar{\psi}) - \left(\frac{a_k^2 \sigma N_p \phi}{\bar{d}} \right)^2 \bar{u} &= 0 \quad [\text{for } -1 \leq \bar{y} \leq -1 + \bar{d}], \\ \frac{d^2 \bar{u}}{d\bar{y}^2} - \frac{\bar{E}}{\lambda^2} \sinh(\bar{\psi}) &= 0 \quad [\text{for } -1 + \bar{d} \leq \bar{y} \leq 0], \end{aligned} \quad (9.20)$$

where all the dimensionless variables are defined in eq.(8.2). Eq.(9.20) will be solved numerically in presence of the boundary conditions expressed in eq.(8.3).

9.3 Results

9.3.1 Free Energy Variation and Equilibrium Brush Height: Results from Analytical Solution

In Fig. 9.1 (left) we show the variation (with \bar{d}) of the total dimensionless electrostatic energy (\bar{F}_{elec}) as well as the electrostatic energies associated with charges on the brush ($F_{B,elec}$) and the induced EDL (\bar{F}_{EDL}). Presence of charges on the PE

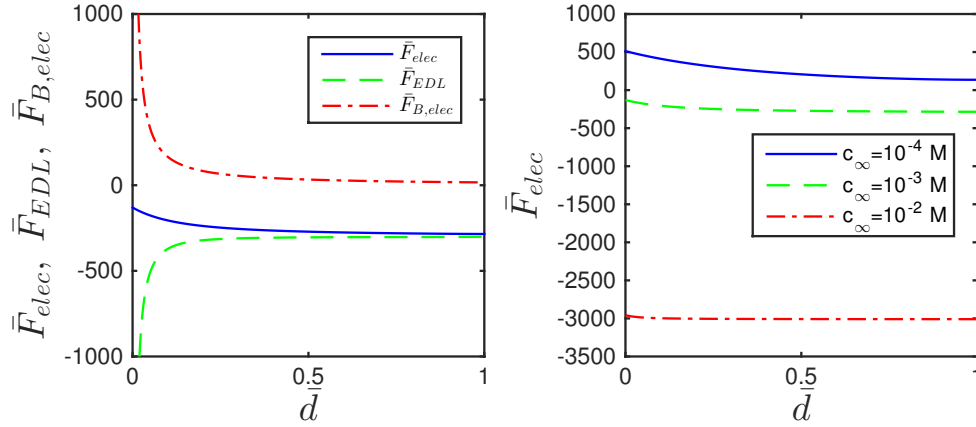


Figure 9.1: (Left) Dimensionless PE brush height (\bar{d}) dependent variation of the total dimensionless electrostatic energy (\bar{F}_{elec}) as well as the electrostatic energies associated with charges on the brush ($\bar{F}_{B,elec}$) and the induced EDL (\bar{F}_{EDL}). In this plot, we consider $c_\infty = 10^{-3} M$, $\ell = 50 nm$, $h = 100 nm$, $N_p = 100$, $f_{ch} = 1$, $a_k = 1 nm$, $T = 300 K$ and $\chi = 0.4$. (Right) Variation of \bar{F}_{elec} with \bar{d} for different values of c_∞ . All other parameters remain identical.

brushes creates an unfavorable energy quantified by $F_{B,elec} > 0$ – this is effectively a manifestation of the repulsion effects triggered by the interacting charged monomers. The induced EDL lowers the energy (since $F_{EDL} < 0$) and the overall energy (though positive) decreases at larger \bar{d} (since greater brush height implies greater distance between the monomers and hence lesser repulsion). This explains why one should expect to witness an enhancement of the polymer brush thickness (\bar{d}) when the polymer brushes contain charges. In other words, regardless of the value of \bar{d}_0 , one would expect that $\bar{d} > \bar{d}_0$ due to the electrostatic effects. Fig. 9.1 (right) also reveals that the increase in salt concentration leads to a less steeper variation of \bar{F}_{elec} with \bar{d} –

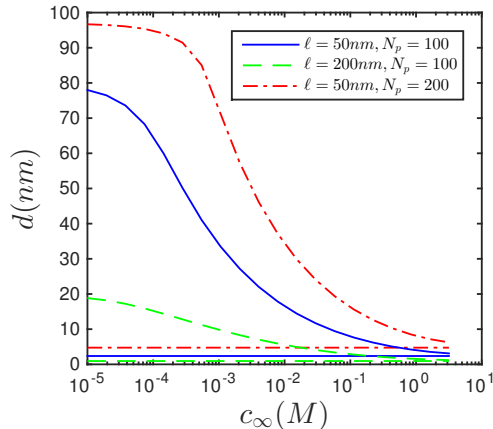


Figure 9.2: Variation of the PE brush height (d) with salt concentration for different PE separation distance (ℓ) and number of monomers (N_p). In this plot, we consider $h = 100 \text{ nm}$, $f_{ch} = 1$, $a_k = 1 \text{ nm}$, $T = 300 \text{ K}$ and $\chi = 0.4$. We consider three different values of d_0 (dictated by three different combinations of ℓ and N_p), such that the resulting electrostatics always allows the use of Debye-Hückel linearization. The lines that are parallel to the c_∞ axis represent the $d = d_0$ value (i.e., when the brushes are uncharged).

as a consequence, one would expect a lesser difference between \bar{d} and \bar{d}_0 at a larger salt concentration. Since for this case, \bar{d} is always greater than \bar{d}_0 , this will signal a decrease in \bar{d} with an increase in the salt concentration. Therefore, through such a simple free energy based argument we can explain why one finds (in simulations and experiments) a decrease in the height of brush (containing charges along the entire backbone) with an increase in the salt concentration.

Fig. 9.2 shows the variation of \bar{d} for the case of PE brushes with backbone charging as a function of the salt concentration for three different values of d_0 (or

equivalently three different combination values of ℓ and N_p). One can clearly witness a monotonic decrease of the brush height with an increase in salt concentration for all combinations of ℓ and N_p . Also we find that the electrostatic effects always swell the brush, i.e., $\bar{d} > \bar{d}_0$ for any value of \bar{d}_0 and c_∞ .

9.3.2 Equilibrium Brush Height: Results from Numerical Solution

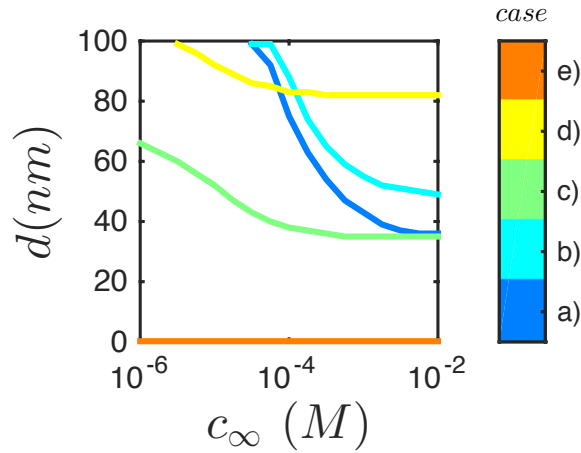


Figure 9.3: Numerical solution for the variation of the equilibrium height of the nanoconfined BBC PE brushes as a function of the salt concentration. The different cases identified here are as follow. Case 1: $N_p = 2000$, $\ell = 80$, $d_0 = 34 \text{ nm}$; Case 2: $N_p = 2800$, $\ell = 80$, $d_0 = 49 \text{ nm}$; Case 3: $N_p = 846$, $\ell = 22$, $d_0 = 34 \text{ nm}$; Case 4: $N_p = 2000$, $\ell = 22$, $d_0 = 82 \text{ nm}$; Case 5: $N_p = 8000$, $\ell = 200$, $d_0 = 75 \text{ nm}$; Case 6: No brushes. Here we use $f_{ch} = \frac{\sigma_{ch}\ell^2}{eN_p} = (-8 \times 10^{-4}C/m^2) \frac{\ell^2}{eN_p}$. Other parameters are identical to those used in Fig. 9.2.

In Fig. 9.3, we provide the variation of the equilibrium brush height obtained numerically, i.e., we work with those combinations of d_0 and salt concentrations that

enforce $|\bar{\psi}| > 1$, thereby forbidding the use of the analytical solution. In this figure we apply $f_{ch} = \frac{\sigma_{ch}\ell^2}{eN_p}$, where $\sigma_{ch} = -8 \times 10^{-4}C/m^2$ is the surface charge used in Chapter 8. This allow us to quantify charge location effect on EOS, while the total amount of charge in space is identical for both end/backbone-charged PE brush grafted nanochannels, and for rigid nanochannels (charge on surface of the substrate). Regardless of the extent of confinement or the salt concentration, we witness (a) $d > d_0$ and (b) a decrease in d with c_∞ . These observations are well reported for PE brushes [103,109,110]. Here we avoid discussing further well-known details about attainment of *osmotic regime* or *salted regime* by the brushes [101,103]. We are more interested to understand how this combination of the brush height and the resulting EDL electrostatics affect the overall EOS transport. Of course, we shall only use the numerically-obtained quantities, since that will allow us to explore much wider ranges of salt concentration and PE brush properties.

9.3.3 Electrostatics and electroosmotic transport: Numerical results

In Fig. 9.4, we show the variation of $|\bar{\psi}|$, n_\pm , \bar{u} , and \bar{f} for these six different cases studied in Fig. 9.3. $|\bar{\psi}|$ is dictated by the interplay of the salt concentration and the salt-concentration-dictated brush height (see Fig.9.3). Obviously, small concentration implies very weak screening and hence maximum repulsion between the charges of the BBC PE brushes, thereby leading to a very high brush value that is often equal to or more than the nanochannel half height. Of course, here we only consider those brush height values that are less than or equal to the nanochannel half height. From

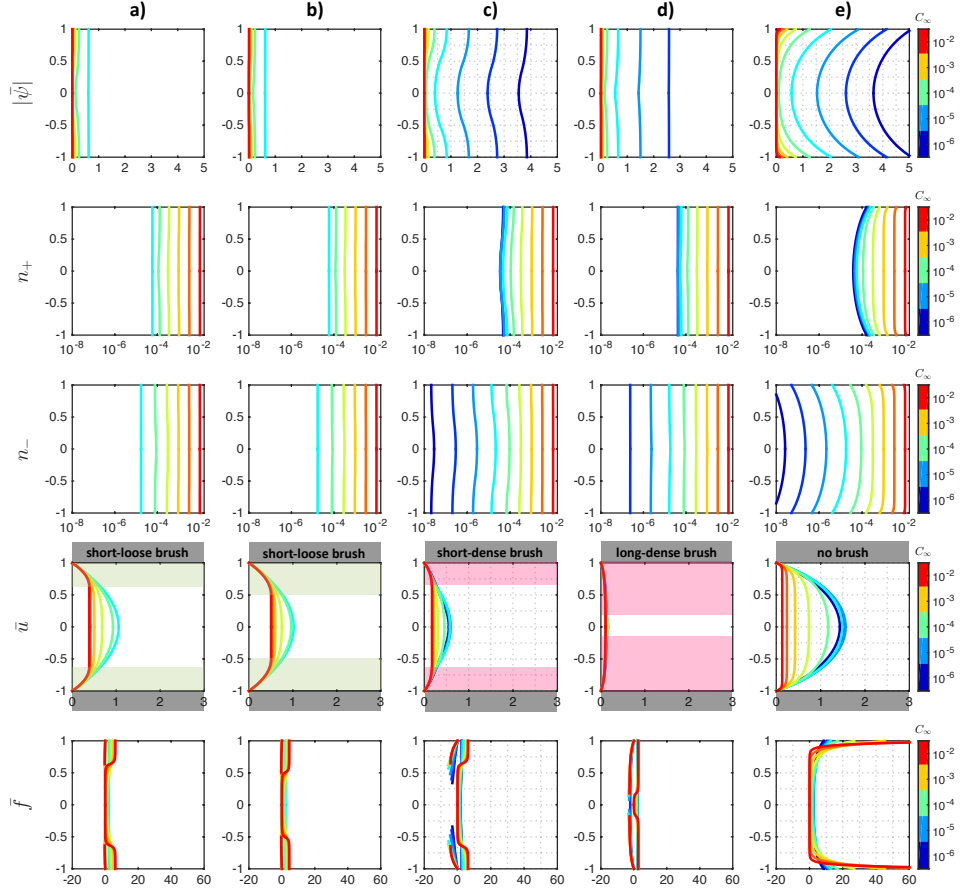


Figure 9.4: Transverse variation of $|\bar{\psi}|$ (magnitude of dimensionless electrostatic potential), n_+ (counterion number density), n_- (coion number density), \bar{u} (dimensionless EOS velocity), and \bar{f} ($\bar{f} > 0$ represents the dimensionless per unit volume EOS body force, while $\bar{f} < 0$ represents the retarding PE-brush-layer-induced per unit volume drag force) for Case 1 ($N_p = 2000$, $\ell = 80$, $d_0 = 34$ nm) [shown in (a)], Case 2 ($N_p = 2800$, $\ell = 80$, $d_0 = 49$ nm) [shown in (b)], Case 3 ($N_p = 846$, $\ell = 22$, $d_0 = 34$ nm) [shown in (c)], Case 4 ($N_p = 2000$, $\ell = 22$, $d_0 = 82$ nm) [shown in (d)], Case 5 ($N_p = 8000$, $\ell = 200$, $d_0 = 75$ nm) [shown in (e)], and Case 6 (No brushes) [shown in (f)]. Other parameters are identical to those used in Fig. 9.2.

Fig. 9.3, we find that for weak to intermediate salt concentrations, most of the cases (Cases 1, 2, 4, 5) have $d \geq h$ (i.e., the nanochannel half height). Therefore, the brushes from the opposing walls occupy occupy the entire nanochannel and as a result demonstrates uniform $|\bar{\psi}|$ value across the nanochannel [see the figures for $|\bar{\psi}|$ in Fig. 9.4(a,b,d,e)]. Therefore, one does not witness non-uniform variation of $|\bar{\psi}|$ across the nanochannel typically associated with small c_∞ [e.g., the variation witnessed for the case of brush-free nanochannels, see Fig. 9.4(f)]. For the BBC PE brush grafted nanochannels, only for Case 3 ($N_p = 846$, $\ell = 22$, $d_0 = 34 \text{ nm}$), $d < h$ for small concentrations – consequently, there is a distinct non-uniformity in $|\bar{\psi}|$ across the nanochannel for small c_∞ [see Fig. 9.4(c)]. Finally, it is worthwhile to note that for all the six nanochannel systems, we witness a larger average $|\bar{\psi}|$ for smaller c_∞ – this can be attributed to the well-known enhanced-screening-induced lowering of $|\bar{\psi}|$ for large c_∞ . Finally, the ion number densities n_\pm are found to be commensurate with the ψ distribution. Therefore, (a) n_\pm demonstrate uniform (non-uniform) values across the nanochannels for cases where $|\bar{\psi}|$ is uniform (non-uniform) and (b) n_+ shows maximum (minimum) values and n_- shows minimum (maximum) values for small (large) values of c_∞ . We shall use these information on EDL electrostatics to eventually study the EOS flow field in these different nanochannel systems.

The most important results of this chapter are the variation of the EOS flow profiles for these six different nanochannel systems, elucidating the role of brush configurations and grafting (or a complete absence of the brushes) as well as the salt concentrations in dictating the EOS flow profiles. For loose brushes [cases 1, 2 and 5 represented in Figs. 9.4(a,b,e), respectively], we clearly witness $(u)_{EOS,brush} >$

$(u)_{EOS,no\ brush}$ for large salt concentrations. Therefore, even for BBC PE brushes, very much like the end-charged brushes, we do witness an increase in EOS velocity, as compared to that in the brush-free nanochannels for large salt concentration and loose brush. The large salt concentration ensures that the EDL is localized – accordingly, when combined with a finite height of the brush, this will imply that average EOS body force is generated away from the wall (please see the corresponding \bar{f} plots in Fig. 9.4) and hence responsible for triggering a larger liquid velocity. On the other hand, the looseness of the brush ensures weak drag force (also witnessed in the \bar{f} plots in Fig. 9.4). These two factors combine to ensure $(u)_{EOS,brush} > (u)_{EOS,no\ brush}$ for cases where brushes are loose and c_∞ is large. This also justifies larger u for a given c_∞ but longer and loose brushes [compare velocity profiles in Fig. 9.4(a,b,e)]. For such loose brushes, however, for smaller c_∞ , $(u)_{EOS,brush} < (u)_{EOS,no\ brush}$ and one witnesses a progressive increase in $(u)_{EOS,brush}$ with a decrease in c_∞ . We also compare the EOS velocity profiles for nanochannels with dense brushes [cases 3 and 4, demonstrated in Fig. 9.4(c,d) respectively]. Substantially large drag force (as witnessed in the \bar{f} plots in Fig. 9.4) ensures $(u)_{EOS,brush} \ll (u)_{EOS,no\ brush}$ for all salt concentration values.

In this context, it is worthwhile to pinpoint the differences in the EOS flow profile between the nanochannels with BBC and end-charged grafted brushes. We do such a thing in Table 9.1.

Table 9.1: Summary of the findings for EOS transport for nanochannels with BBC and end-charged brushes. Here u_B , u_{NB} , $u_{B,EC}$, $u_{B,BBC}$, $u_{B,LC}$, and $u_{B,SC}$ respectively denote EOS velocity in nanochannels grafted with brushes, no-brushes, end-charged brushes, backbone-charged brushes, brushes in presence of large salt concentration, and brushes in presence of small salt concentration.

Brush Grafting	Brush height	c_∞	Result
Loose Brush	Large c_∞	End Charged	$u_B \gg u_{NB}$
Loose Brush	Large c_∞	Backbone Charged	$u_B > u_{NB}, \frac{ u_{B,EC}-u_{NB} }{ u_{B,BBC}-u_{NB} } > 1$
Loose Brush	Small c_∞	End Charged	$u_B \leq u_{NB}$
Loose Brush	Small c_∞	Backbone Charged	$u_B \ll u_{NB}$
Loose Brush	c_∞ range	End Charged	$u_{B,LC} \leq u_{B,SC}$
Loose Brush	c_∞ range	Backbone Charged	$u_{B,LC} < u_{B,SC}$
Dense Brush	Large c_∞	End Charged	$u_B > u_{NB}$
Dense Brush	Large c_∞	Backbone Charged	$u_B \ll u_{NB}$
Dense Brush	Small c_∞	End Charged	$u_B < u_{NB}$
Dense Brush	Small c_∞	Backbone Charged	$u_B \ll u_{NB}$
Dense Brush	c_∞ range	End Charged	$u_{B,LC} \leq u_{B,SC}$
Dense Brush	c_∞ range	Backbone Charged	$u_{B,LC} < u_{B,SC}$

9.4 Conclusions

In this chapter, we develop mean field based models to analyze the EOS transport in nanochannels grafted with BBC PE brushes. The employment of the mean field approach allows, for the first time, accounting of the thermodynamically consistent PE brush configuration and electrostatics in the calculations of the EOS velocity field. The results while establishing classical notions about salt-concentration-induced lowering of the brush height and lowering of the EOS transport due to the augmented drag force exerted by the brushes, also reveal the highly non-intuitive enhancement in the EOS velocity for loose brushes in presence of large salt concentration. In summary, the findings of the present and the previous chapter combine to shed light on a hitherto unknown design of a PE-brush-grafted nanochannel that has the most remarkable capability of *enhancing* liquid transport.

Chapter 10: Summary, impact of the present thesis, and scope of future research

In this chapter, we shall summarize the key contributions of the thesis and its impact in the broad soft matter community. Finally, we shall end with the scope of future research.

10.1 Key contributions: Summary and Impact

The following have been the key findings, contributions, and impact of the present thesis:

- We developed new *scaling laws* to describe the conditions that will ensure that polymer molecules grafted on the inner walls of a nanochannel will **form brushes**, and yet will not interpenetrate with the brushes from the opposite wall. These scaling laws are important to define a new regime for analyzing polymer and PE brushes in a nanoconfined state, i.e., for the first time the impact of nanoconfinement (in a non-interpenetrating set up) is being analyzed.
- We developed new *scaling laws* to determine the conditions that will allow **decoupling** the nanoconfined brush electrostatics problem from the non-electrostatic one. Such decoupling is at the heart of studying the PE brush electrostatics

by describing the PE brush to be of constant electrostatic-effect-independent height. Our analysis provides the first mathematical justification of such an assumption. Identification of the decoupling regime will allow tackling of much more involved electrostatic problems (e.g., brush behavior in presence of multivalent counterions) theoretically that would have been otherwise difficult to carry out.

- We developed models for probing the *electrostatics* of nanochannels grafted with pH responsive PE brushes, with the brushes being modelled in the decoupled regime. Our models discover major lacuna in the state of the art models for pH-responsive PE brushes. In all the existing models the H^+ ion concentration has been modelled simplistically using Boltzmann distribution. Such an approach forbids the accounting of the contribution of the pH-dependent ionization reaction (within the PE brush layer) in the description of the H^+ ion equilibrium. The eventual result is a grossly unphysical discontinuous H^+ ion concentration profile. Our model rectify this problem by proposing a non-unique cubic distribution of the monomers.
- We developed models to compute the *electrokinetics* (ionic current and electroosmotic transport) in nanochannels grafted with PE brushes, with the brushes being modeled in the decoupled regime. The analysis, in addition to providing a detailed accounting of the influence of the different system parameters, pinpoint the usefulness of nanochannels grafted with pH-responsive PE brushes as excellent EOF flow suppressors. Such flow suppressing action will make these

channels ideal for carrying out applications that necessitate precise determination of minute ionic current changes for ion sensing and current rectification.

- We next propose models to study the nanoconfined PE brush *electrostatics* in the **coupled regime**. The models are based on mean field approaches that quantify the PE brush configuration accounting for both non-electrostatic and electrostatic effects. We first study the problem of end-charged nanoconfined brushes – i.e., we consider brushes containing charges only at their non-grafted ends. Most remarkably, we witness that brushes may actually swell with an increase in the salt concentration. This is completely contrary to what happens for brushes containing charges along their entire backbone. We anticipate that discovery of such nanoconfined brushes with a new response regime (with respect to salt concentration) will allow opening up new horizons of nanofluidic designs with end-charged-brush-functionalized nano-interfaces.
- We use the configuration and electrostatic description of the nanoconfined *end-charged* PE brushes to obtain the *electrokinetics* (ionic current and EOS flow) in nanochannels grafted with such brushes. Therefore, for the first time electrokinetics in PE-brush-grafted nanochannels have been computed by accounting for the appropriate thermodynamics and configuration of the brushes. We witness, most amazingly, that EOS flow can be severely *enhanced* in PE-brush-grafted nanochannels as compared to EOS flow in brush-free nanochannels. We identify that such a behavior stems from the localization of the EDL and the electroosmotic body force at the brush end (where the charge is localized),

thereby enforcing a large liquid velocity under the influence of negligible wall shear stress. This finding completely overturns the classical understanding of the massive reduction in flow in brush-grafted nanochannels. In fact, such massively enhanced EOS flow in brush-grafted nanochannels may now be used for a variety of applications of generating augmented nanofluidic transport.

- Finally, we develop mean field models to study the configuration, electrostatics, and transport in *backbone-charged* (BBC) PE brushes. The results indicate progressive lowering of brush height with salt concentration. More importantly, one can identify certain parameter combination where EOS transport even in such BBC PE brush grafted nanochannels can be enhanced in comparison to the EOS transport in brush-free nanochannels.

10.2 Scope of future research

Theories: Further investigation in the configuration of PE

We have used a step function as the PE monomer distribution, which allow us to use the Alexander-de-Gennes theories to model the elastic and excluded volume effect on PE brushes. However over the past 30 years, researchers have witnessed non-uniform monomer density inside the polymer or PE brushes from experiments and molecular dynamic simulations. Theorists also applied hypothesis about the chain free ends that they may be located within the PE brushes rather than the brush-electrolyte interface. On one hand, all these proposed models require more detailed theories, which may not be valid for all kinds of PE brushes. For example, our end-

charged PE brush systems (Chapter 6-7) cannot be modeled using the well-accepted "parabolic profile" for polymer brush. On the other hand, some part of the proposed model is found coincident with our finding, yet some part is self-contradicting or need more investigation according to our research. For instance, by considering the explicit hydrogen ion distribution in pH-responsive PE grafted nanochannels(Chapter 3), we find the PE charge should vanish smoothly (2nd order continuity) at the PE-brush-electrolyte interface, which is close to the "parabolic profile" where the monomer number vanish at the interface (1st order continuity); However, the charge distribution are often assumed to be uniform for the "parabolic" PE model, which we proved to be incorrect. Therefore, the configuration of PE brush systems (planar brush and brush grafted on cylindrical or spherical surfaces) remain to be probed, and the first step can focus on solving the contradiction mentioned above.

Applications and designs: The completed modeling of PE-grafted Nanochannels coupling the thermodynamics, electrostatics and electrokinetics presented in this dissertation will allow us to improve the current nanofluidic systems, such as:

1. *High-efficient reversible pH-responsive ionic sensing based on the PE-brush-grafted nanochannels.* The enhancement of EOS velocity in nanochannels by grafting PE brush inside the nanochannel is shown in chapter 8-9, which will improve the sensing efficiency. Also full range of PE characteristics can manipulated in the numerical model, which will help to design a nanofluidic systems to achieve multiple purposes.
2. *Sensitive and reversible pH-responsive ionic gating based on the PE-brush-grafted nanochannels.* The presented model can help to select a set of parameters that ensures the PE brush height varies dramatically with pH or salt concentration.

These parameters, according to our scaling laws, should ensure that the electrostatic effect dominates the configuration of the PE chains.

Bibliography

- [1] S. Alexander, *J. Phys.*, **38**, 977 (1977).
- [2] P.-G. de Gennes, *J. Phys.*, **37**, 1443 (1976).
- [3] P.-G. de Gennes, *Macromolecules*, **13**, 1069 (1980).
- [4] R. R. Netz and D. Andelman, *Phys. Rep.* **380**, 1 (2003).
- [5] S. Das, M. Banik, G. Chen, S. Sinha, R. Mukherjee, *Soft Matt.* **11**, 8550 (2015).
- [6] S. T. Milner, *Science* **251**, 905 (1991).
- [7] P. A. Rühls, J. Adamcik, S. Bolisetty, A. Sánchez-Ferrera, and R. Mezzenga, *Soft Matt.* **7**, 3571 (2011).
- [8] G. Chen and S. Das, *J. Phys. Chem. B* **119**, 12714 (2015).
- [9] P. Jain, G. L. Baker, and M. L. Bruening, *Ann. Rev. Anal. Chem.* **2**, 387 (2009).
- [10] T. K. Tam, J. Zhou, M. Pita, M. Ornatska, S. Minko, and E. Katz, *J. Am. Chem. Soc.* **30**, 10888 (2008).
- [11] O. H. Kwon, A. Kikuchi, M. Yamato, and T. Okano, *Biomaterials* **24**, 1223 (2003).
- [12] S. Dey, B. Kellam, M. R. Alexander, C. Alexander, F. R. A. J. Rose, *J. Mater. Chem.* **21**, 6883 (2011).
- [13] G. Gao, K. Yu, J. Kindrachuk, D. E. Brooks, R. E.E W. Hancock, and J. N. Kizhakkedathu, *Biomacromolecules* **12**, 3715 (2011).

- [14] B. Xin and J. Hao, *J. Chem. Soc. Rev.* **39**, 769 (2010).
- [15] F. Zhou and W. T. S. Huck, *Chem Commun.* **48**, 5999 (2005).
- [16] S. Samanta and J. Locklin, *Langmuir* **24**, 9558 (2008).
- [17] K. Knop, R. Hoogenboom, D. Fischer, and U. S. Schubert, *Angew. Chem. Int. Ed.* **49**, 6288 (2010).
- [18] J. S. Suk, Q. Xu, N. Kim, J. Hanes, and L. M. Ensign, *Adv. Drug Deliver. Rev.* *doi* : 10.1016/j.addr.2015.09.012 (2015).
- [19] V. Goel, J. Pietrasik, H. Dong, J. Sharma, K. Matyjaszewski, and Krishnamoorti, *Macromolecules* **44**, 8129 (2011).
- [20] H. ShamsiJazeyi, C. A. Miller, M. S. Wong, J. M. Tour, and R. Verduzco, *J. Appl. Polym. Sci.* **131**, 40576 (2014).
- [21] J. O. Zoppe, R. A. Venditti, O. J. Rojas, *J. Colloid Interface Sci.* **369**, 202 (2012).
- [22] C. Jiang, Y. Zhang, Q. Wang, and T. Wang, *J. Appl. Polym. Sci.* **129**, 2959 (2013).
- [23] H. Suzuki, M. Murou, H. Kitano, K. Ohno, and Y. Saruwatari, *Colloid. Surf. B* **84**, 111 (2011).
- [24] G. V. Ramesh, S. Porel, and T. P. Radhakrishnan, *Chem. Soc. Rev.* **38**, 2646 (2009).
- [25] S. P. Adiga and D. W. Brenner, *J. Funct. Biomater* **3**, 239 (2012).
- [26] G. Chen and S. Das, *J. Appl. Phys.* **117**, 185304 (2012).
- [27] G. W. de Groot, M. G. Santonicola, K. Sugihara, T. Zambelli, E. Reimhult, J. Vörös, and G. J. Vancso, *ACS Appl. Mater. Interface.* **5**, 1400 (2013).
- [28] B. Yameen, M. Ali, R. Neumann, W. Ensinger, W. Knoll, and O. Azzaroni, *J. Am. Chem. Soc.* **131**, 2070 (2009).
- [29] M. Ali, B. Yameen, R. Neumann, W. Ensinger, W. Knoll, and O. Azzaroni, *J. Am. Chem. Soc.* **130**, 16351 (2008).

- [30] M. Ali, B. Yameen, J. Cervera, P. Ramirez, R. Neumann, W. Ensinger, W. Knoll, and O. Azzaroni, *J. Am. Chem. Soc.* **132**, 8338 (2010).
- [31] B. Vilozny, A. L. Wollenberg, P. Actis, D. Hwang, B. Singaram, and N. Pourmand, *Nanoscale* **5**, 9214 (2013).
- [32] M. Ali, P. Ramirez, S. Mafe, R. Neumann, and W. Ensinger, *ACS Nano* **3**, 603 (2009).
- [33] M. Ali, B. Schiedt, R. Neumann, and W. Ensinger, *Macromol. Biosci.* **10**, 28 (2010).
- [34] S. Umehara, M. Karhanek, R. W. Davis, and Nader Pourmand, *Proc. Natl. Acad. Sci.* **106**, 4611 (2009).
- [35] S. Chanda, S. Sinha, and S. Das, *Soft Matt.* **10**, 7558 (2014).
- [36] M. Daoud and J. P. Cotton, *J. Phys.* **43**, 531 (1982).
- [37] A. Halperin, *J. Phys.*, **49**, 547 (1988).
- [38] E. B. Zhulina, O. Borisov, V. A. Pryamitsyn and T. M. Birshtein, *Macromolecules* **24**, 140 (1991).
- [39] C. M. Wijmans, J. M. H. M. Scheutjens, and E. B. Zhulina, *Macromolecules* **25**, 2657 (1992).
- [40] R. R. Netz and M. Schick, *Macromolecules* **31**, 5105 (1998).
- [41] S. T. Milner, T. A. Witten and M. E. Cates, *Europhys. Lett.* **5**, 413 (1988).
- [42] S. T. Milner, T. A. Witten and M. E. Cates, *Macromolecules* **21**, 610 (1988).
- [43] A. M. Skvortsov, I. V. Pavlushkov, A. A. Gorbunov, Y. B. Zhulina, O. V. Borisov and V. A. Pryamitsyn, *J. Polym. Sci., Part B: Polym. Phys.* **30**, 1706 (1988).
- [44] Y. B. Zhulina, V. A. Pryamitsyn and O. V. Borisov, *Pol. Sci. U.S.S.R.* **31**, 205 (1989).
- [45] Y. B. Zhulina and O. V. Borisov, *J. Chem. Phys.* **107**, 5952 (1997).
- [46] Y. B. Zhulina and O. V. Borisov, *Langmuir* **27**, 10615 (2011).

- [47] D. J. Sandberg, J-M. Y. Carrillo, and A. V. Dobrynin, *Langmuir* **23**, 12716 (2007).
- [48] J-M. Y. Carrillo and A. V. Dobrynin, *Langmuir* **25**, 13158 (2009).
- [49] D. Russano, J-M. Y. Carrillo, and A. V. Dobrynin, *Langmuir* **27**, 11044 (2011).
- [50] J-M. Y. Carrillo, D. Russano, and A. V. Dobrynin, *Langmuir* **27**, 14599 (2011).
- [51] F. L. Verso, S. A. Egorov, A. Milchev, and K. Binder, *J. Chem. Phys.* **133**, 184901 (2010).
- [52] Z. Zeng, L. H. Yeh, M. Zhang, and S. Qian, *Nanoscale* **7**, 17020 (2015).
- [53] Z. Milne, L. H. Yeh, T. H. Chou, and S. Qian, *J. Phys. Chem. C* **118**, 19806 (2014).
- [54] I. Luzinov, S. Mino, and V. V. Tsukruk, *Soft Matt.* **4**, 714 (2008).
- [55] A. J. Ryan et al., *Farad. Discuss.* **128**, 55 (2005).
- [56] G. Chen and S. Das, *RSC Adv.* **5**, 4493 (2015).
- [57] G. Chen and S. Das, *Phys. Chem. Chem. Phys.* (Submitted).
- [58] H. Ohshima, *Adv. Colloid Interface Sci.* **62**, 189 (1995).
- [59] H. Ohshima, *Soft Matt.* **8**, 3511 (2012).
- [60] A. C. Barbati and B. J. Kirby, *Soft Matt.* **8**, 10598 (2012).
- [61] H. Ohshima, *Sci. Technol. Adv. Mater.* **10**, 063001 (2009).
- [62] K. Makino and H. Ohshima, *Sci. Technol. Adv. Mater.* **12**, 023001 (2011).
- [63] J. F. L. Duval and F. Gaboriaud, *Curr. Opin. Colloid Interface Sci.* **15**, 184 (2010).
- [64] J. F. L. Duval, J. Merlin and P. Anantha, *Phys. Chem. Chem. Phys.* **13**, 1037 (2011).
- [65] B. Yameen, M. Ali, R. Neumann, W. Ensinger, W. Knoll and O. Azzaroni, *Nano Lett.* **9**, 2788 (2009).

- [66] X. Hou, Y. J. Liu, H. Dong, F. Yang, L. Li and L. Jiang, *Adv. Mater.* **22**, 2440 (2010).
- [67] D. Hlushkou, J. M. Perry, S. C. Jacobson, and U. Tallarek, *Anal. Chem.* **84**, 267 (2012).
- [68] Z. Guo, J. Wang, J. Ren, and E. Wang, *Nanoscale* **3**, 3767 (2011).
- [69] G. Xie, W. Tian, L. Wen, K. Xiao, Z. Zhang, Q. Liu, G. Hou, P. Li, Y. Tian, and L. Jiang, *Chem. Comm.* **51**, 3135 (2015).
- [70] Z. Siwy, L. Trofin, P. Kohli, L. A. Baker, C. Trautmann, and C. R. Martin, *J. Am. Chem. Soc.* **127**, 5000 (2009).
- [71] M. Ali, R. Neumann, and W. Ensinger, *ACS Nano* **4**, 7267 (2010).
- [72] M. Ali, S. Mafe, P. Ramirez, R. Neumann, and W. Ensinger, *W. Langmuir* **25**, 11993 (2009).
- [73] M. Ali, M. N. Tahir, Z. Siwy, R. Neumann, W. Tremel, and W. Ensinger, *Anal. Chem.* **83** 1673 (2011).
- [74] B. Yameen, M. Ali, R. Neumann, W. Ensinger, W. Knoll, and O. Azzaroni, *Chem. Commun.* **46**, 1908 (2010).
- [75] F. Xia et al., *J. Am. Chem. Soc.* **130**, 8345 (2008).
- [76] Q. Cao, C. Zuo, L. Li, Y. Zhang, G. Yan, *J. Polym. Sci., Part B: Polym. Phys.* **50**, 805 (2012).
- [77] F. Tessier and G. W. Slater, *Macromolecules* **39**, 1250 (2006).
- [78] Z. Zhang, C. Zuo, Q. Cao, Y. Ma, and S. Chen, *Macromol. Theory Simul.* **21**, 145 (2012).
- [79] G. Chen and S. Das, *J. Colloid Interface Sci.* **445**, 357 (2015).
- [80] Q. Gao and E. S. Yeung, *Anal. Chem.* **70**, 1382 (1998).
- [81] S. Qi, X. Liu, S. Ford, J. Barrows, G. Thomas, K. Kelly, A. McCandless, K. Lian, J. Goettert, and S. A. Soper, *Lab Chip* **2**, 88 (2002).
- [82] L. Bendahl, S. H. Hansen, and B. Gammelgaard, *Electrophoresis* **22**, 2565 (2001).

- [83] B. Pranaityte and A. Padarauskas, *Electrophoresis* **27**, 1915 (2006).
- [84] Y. Zuo, G. Wang, Y. Yu, C. Zuo, Z. Liu, D. Hu, and Y. Wang, *Microfluid. Nanofluid.* **17**, 923 (2014).
- [85] D. Kaniansky, M. Masar, and J. Bielicikova, *J. Chromotogr. A* **792**, 483 (1997).
- [86] T. Kaneta, T. Ueda, K. Hata, and T. Imasaka, *J. Chromotogr. A* **1106**, 52 (2006).
- [87] F. I. Uba, S. R. Pullagurla, N. Sirasunthorn, J. Wu, S. Park, R. Chantiwas, Y.-K. Cho, H. Shin, and S. A. Soper, *Analyst* **140**, 113 (2015).
- [88] S. Das, P. Dubsy, A. van den Berg, and J. C. T. Eijkel, *Phys. Rev. Lett.* **108**, 138101 (2012).
- [89] S. Das, S. Chanda, J. C. T. Eijkel, N. R. Tas, S. Chakraborty, and S. K. Mitra, *Phys. Rev. E* **90**, 043011 (2014).
- [90] P. G. de Gennes, *Macromolecules* **9**, 594 (1976).
- [91] J. Klein, *Colloid. Surf. A* **86**, 63 (1994).
- [92] G. H. Fredrickson and P. Pincus, *Langmuir* **7**, 786 (1991).
- [93] J. L. Harden and M. E. Cates, *Phys Rev E* **53**, 3782 (1996).
- [94] Y. W. Kim, V. Lobaskin, C. Gutsche, F. Kremer, P. Pincus, and R. R. Netz, *Macromolecules* **42**, 3650 (2009).
- [95] S. Pennathur and J. G. Santiago, *Anal. Chem.* **77**, 6782 (2005).
- [96] Y. Tsori, D. Andelman, and J.-F. Joanny, *Euro. Phys. Lett.* **82**, 46001 (2008).
- [97] D. Heine and D. T. Wu, *J. Chem. Phys.* **114**, 5313 (2001).
- [98] V. A. Pryamitsyn, F. A. M. Leermakers, and E. B. Zhulina, *Macromolecules* **30**, 584 (1997).
- [99] X. Chu, J. Yang, G. Liu, and J. Zhao, *Soft Matt.* **10**, 5568 (2014).
- [100] E. B. Zhulina, T. M. Birshstein, and O. V. Borisov, *Macromolecules* **28**, 1491 (1995).

- [101] P. Pincus, *Macromolecules* **24**, 2912 (1991).
- [102] O. V. Borisov, T. M. Birshtein, and E. B. Zhulina, *J. Phys. II* **1**, 521 (1991).
- [103] E. B. Zhulina and M. Rubinstein, *Soft Matt.* **8**, 9376 (2012).
- [104] M. W. Matsen, *Eur. Phys. J. E* **34**, 45 (2011).
- [105] M. W. Matsen, *Eur. Phys. J. E* **35**, 12 (2012).
- [106] N. A. Kumar and C. Seidel, *Macromolecules* **38**, 9341 (2005).
- [107] H. Chen, R. Zajac, and A. Chakrabati, *J. Chem. Phys.* **104**, 1579 (1996).
- [108] C. Ibergay, P. Malfreyt, and D. J. Tildesley, *J. Phys. Chem. B* **114**, 7274 (2012).
- [109] R. Toomey and M. Tirrell, *Annu. Rev. Phys. Chem.* **59**, 493 (2008).
- [110] M. N. Tamashiro, E. Hernandez-Zapata, P. A. Schorr, M. Balastre, M. Tirrell, and P. Pincus, *J. Chem. Phys.* **115**, 1960 (2001).
- [111] H. Ahrens, S. Förster, and C. Helm, *Phys. Rev. Lett.* **81**, 4172 (1998).
- [112] S. Sanjuan, P. Perrin, and N. Pantoustier, *Langmuir* **23**, 5769 (2007).
- [113] M. Biesalski, D. Johannsmann, and R. Rühle, *J. Chem. Phys.* **120**, 8807 (2004).
- [114] S. Baldessari and J. G. Santiago, *J. Colloid Interface Sci.* **325**, 526 (2008).
- [115] S. Das, A. Guha, and S. K. Mitra, *Anal. Chim. Acta* **804**, 159 (2013).
- [116] H. Ohshima, *Colloid Polym. Sci.* **277**, 535 (1999).
- [117] H. Ohshima, *Colloid Polym. Sci.* **292**, 431 (2014).
- [118] C. Han, X. Hou, H. Zhang, W. Guo, H. Li, and L. Jiang, *J. Am. Chem. Soc.* **133**, 7644 (2011).
- [119] Z. Sun, C. Han, M. Song, L. Wen, D. Tian, H. Li, and L. Jiang, *Adv. Mater.* **26**, 455 (2014).
- [120] H. Wang, S. Hou, Q. Wang, Z. Wang, X. Fan, and J. Zhai, *J. Mater. Chem. B* **3**, 1699 (2015).

- [121] S. Mura, J. Nicolas, and P. Couvreur, *Nat. Mater.* **12**, 991 (2013).
- [122] J. Patwary, G. Chen, and S. Das, *Microfluid. Nanofluid.* **20**, 37 (2016).
- [123] A. Poddar, D. Maity, A. Bandopadhyay, and S. Chakraborty, *Soft Matt.* **12**, 5968 (2016).
- [124] G. Chen and S. Das, *J. Phys. Chem. B* **120**, 6848 (2016).
- [125] G. Chen and S. Das, *Electrophoresis* DOI : 10.1002/*elps*.201600415 (2016).
- [126] S. Mishra, S. Varanasi, and P. P. Varanasi, *Macromolecules* **22**, 4173 (1989).